

INTEGRATED HYDROGEOLOGICAL AND GEOCHEMICAL  
PROCESSES IN SWELLING CLAY-SULFATE ROCKS

zum Erlangen des akademischen Grades eines

DOKTORS DER NATURWISSENSCHAFTEN  
(Dr.rer.nat.)

von der KIT-Fakultät für  
Bauingenieur-, Geo- und Umweltwissenschaften

des Karlsruher Instituts für Technologie (KIT)  
genehmigte

DISSERTATION

von  
M.Sc. Daniel Michael Schweizer  
aus Freiburg

Tag der mündlichen Prüfung:  
21. Oktober 2019

REFERENT: Prof. Dr. Christoph Butscher  
KORREFERENT: Prof. Dr. Nico Goldscheider

Karlsruhe Oktober 2019



*Ohana* means family.  
Family means nobody gets left behind, or forgotten.  
— Lilo & Stitch

Dedicated to my wonderful parents  
Karl and Brigitte Schweizer  
and  
my beloved partner  
Sonja Becker.



# CONTENTS

---

LIST OF FIGURES	viii
LIST OF TABLES	ix
ABSTRACT	xi
KURZFASSUNG	xiii
<b>I INTRODUCTION</b>	<b>1</b>
1 INTRODUCTION	3
1.1 The swelling mechanism: underlying processes and controls . . . . .	4
1.2 Objectives . . . . .	7
1.3 Study site . . . . .	8
1.4 Structure of the thesis . . . . .	9
<b>II UNCERTAINTY ASSESSMENT IN 3D GEOLOGICAL MODELS OF INCREASING COMPLEXITY</b>	<b>13</b>
2 PART 2: UNCERTAINTY ASSESSMENT IN 3D GEOLOGICAL MODELS	15
2.1 Introduction . . . . .	15
2.2 Study site . . . . .	17
2.3 Methods . . . . .	18
2.3.1 Input data . . . . .	18
2.3.2 3D geological modeling . . . . .	20
2.3.3 Uncertainty assessment . . . . .	21
2.3.4 Model dissimilarity . . . . .	25
2.4 Results and discussion . . . . .	26
2.4.1 Initial 3D models . . . . .	26
2.4.2 Multiple model realizations . . . . .	27
2.4.3 Uncertainty assessment . . . . .	30
2.4.4 Models dissimilarity . . . . .	34
2.5 Summary and conclusions . . . . .	35
2.6 Acknowledgments . . . . .	37
<b>III REACTIVE TRANSPORT MODELING OF SWELLING PROCESSES IN CLAY-SULFATE ROCKS</b>	<b>39</b>
3 PART 3: A CONCEPTUAL REACTIVE TRANSPORT MODEL	41
3.1 Introduction . . . . .	41
3.2 Study site . . . . .	45
3.2.1 Overview . . . . .	45
3.2.2 Geology and hydrogeology . . . . .	46
3.3 Conceptual and numerical model development . . . . .	48
3.3.1 Conceptual approach: overview . . . . .	48
3.3.2 Numerical model setup . . . . .	50

3.3.3	Modeling tools . . . . .	50
3.3.4	Groundwater flow . . . . .	50
3.3.5	Solute transport . . . . .	52
3.3.6	Geochemical reactions . . . . .	53
3.3.7	Swelling model . . . . .	56
3.3.8	Model calibration . . . . .	57
3.4	Field observation data . . . . .	59
3.4.1	Groundwater chemistry . . . . .	59
3.4.2	Geodetic monitoring network . . . . .	60
3.5	Results and Discussion . . . . .	62
3.5.1	Simulated flow and reactive transport . . . . .	62
3.5.2	Simulated ground heave . . . . .	64
3.5.3	Estimated parameters . . . . .	68
3.5.4	Parameter uncertainty analysis . . . . .	72
3.6	Conclusions . . . . .	73
3.7	Acknowledgments . . . . .	74
<b>IV</b>	<b>ANALYZING THE HEAVE OF AN ENTIRE CITY: MODEL- ING OF SWELLING PROCESSES IN CLAY-SULFATE ROCKS</b>	<b>77</b>
<b>4</b>	<b>ANALYZING THE HEAVE OF AN ENTIRE CITY: A CASE STUDY</b>	<b>79</b>
4.1	Introduction . . . . .	79
4.2	Study site . . . . .	82
4.3	Modeling approach . . . . .	86
4.3.1	Modeling tools . . . . .	86
4.3.2	Numerical modeling framework . . . . .	86
4.3.3	Setup of the flow model . . . . .	87
4.3.4	Setup of the reactive transport model . . . . .	88
4.3.5	Calculation of heave . . . . .	90
4.3.6	Model calibration . . . . .	92
4.3.7	Mitigation scenarios . . . . .	93
4.4	Results and Discussion . . . . .	93
4.4.1	Calibrated model . . . . .	93
4.4.2	Assessment of mitigation measures . . . . .	99
4.5	Conclusion . . . . .	105
4.6	Acknowledgments . . . . .	105
<b>V</b>	<b>SYNTHESIS AND DISCUSSION</b>	<b>107</b>
<b>5</b>	<b>SYNTHESIS AND DISCUSSION</b>	<b>109</b>
5.1	Summary . . . . .	109
5.2	Discussion and Outlook . . . . .	112
<b>VI</b>	<b>APPENDIX</b>	<b>117</b>
<b>A</b>	<b>APPENDIX</b>	<b>119</b>
A.1	Appendix of Part II . . . . .	119
A.1.1	Structural uncertainty workflow parameters . . . . .	119
A.2	Appendix of Part III . . . . .	122

A.2.1 Uplift rates . . . . .	122
A.2.2 Bulking coefficient . . . . .	122
<b>back matter</b>	<b>125</b>
<b>BIBLIOGRAPHY</b>	<b>127</b>
<b>OWN PUBLICATIONS</b>	<b>143</b>
<b>ACKNOWLEDGEMENTS</b>	<b>145</b>
<b>DECLARATION</b>	<b>147</b>

## LIST OF FIGURES

---

Figure 1.1	The sulfate swelling volume increase . . . . .	5
Figure 1.2	The precipitation of gypsum crystals . . . . .	6
Figure 2.1	The study site Staufen in southern Germany .	18
Figure 2.2	Data categories and geological input data . . .	19
Figure 2.3	Stratigraphy and geological units . . . . .	20
Figure 2.4	The workflow of uncertainty assessment . . . .	23
Figure 2.5	The distance measures scheme . . . . .	26
Figure 2.6	Cross-sections of geological models . . . . .	28
Figure 2.7	Cross-sections of multiple model realizations .	29
Figure 2.8	Information entropy in 3D model . . . . .	31
Figure 2.9	Comparison of average model entropy . . . .	33
Figure 2.10	Comparison of fuzzy set entropy . . . . .	33
Figure 2.11	Dissimilarities between models . . . . .	35
Figure 3.1	Location of the study site, the interpolated up- lift and relevant boreholes . . . . .	47
Figure 3.2	The stratigraphy, lithology and hydraulic prop- erties at the study site . . . . .	49
Figure 3.3	The conceptual model . . . . .	51
Figure 3.4	The sulfate swelling model . . . . .	58
Figure 3.5	The mineral saturation indices . . . . .	60
Figure 3.6	Normalized uplift measurements . . . . .	62
Figure 3.7	The temporal evolution of the simulated water composition . . . . .	65
Figure 3.8	Comparison of heave development . . . . .	66
Figure 3.9	Comparison of volume development . . . . .	66
Figure 3.10	Parameter uncertainty analysis results . . . . .	72
Figure 4.1	Overview of the study site . . . . .	83
Figure 4.2	2D cross section . . . . .	85
Figure 4.3	Mogi approach . . . . .	91
Figure 4.4	Comparison of piezometric heads . . . . .	95
Figure 4.5	Pre-countermeasure head distribution . . . . .	96
Figure 4.6	Post-countermeasure head distribution . . . .	97
Figure 4.7	Ingressed water content and gypsum growth rate	98
Figure 4.8	Comparison of simulated and measured heave	99
Figure 4.9	3D heave body . . . . .	100
Figure 4.10	Water budgets: calibrated model . . . . .	101
Figure 4.11	Water budgets: scenarios . . . . .	102
Figure 4.12	Comparison of simulated scenarios . . . . .	103
Figure 4.13	Transferability and application . . . . .	104
Figure A.1	Comparison of uplift rates . . . . .	123
Figure A.2	Comparison of bulking coefficients . . . . .	123

## LIST OF TABLES

---

Table 3.1	The water compositions . . . . .	61
Table 3.2	Hydraulic model parameters . . . . .	69
Table 3.3	Reactive transport and mechanical model parameters . . . . .	71
Table 4.1	Stratigraphy and formations . . . . .	84
Table 4.2	Stress periods of the numerical model . . . . .	87
Table 4.3	Hydraulic and transport model properties . . . . .	89
Table 4.4	Overview of simulated scenarios . . . . .	94
Table A.1	Fault parameter settings . . . . .	119
Table A.2	Variogram parameter settings . . . . .	120
Table A.3	Horizon parameter settings . . . . .	121



## ABSTRACT

---

Swelling clay-sulfate rocks repeatedly lead to unforeseen problems in tunneling or shallow geothermal drilling and make lengthy and costly remediation measures necessary. The processes underlying the swelling are complex and not yet sufficiently understood. In general, an increase in rock volume caused by the transformation of the mineral anhydrite into gypsum is considered the main mechanism of swelling. Trigger of the transformation is assumed to be a change in hydraulic conditions, followed by a water access in the expansive rock layers, which in turn changes the prevailing geochemical conditions. In the city of Staufen, Germany, the study site of the thesis, this resulted in large-scale heave at the ground surface, and enormous damage to houses and infrastructure. However, the hydrogeological and geochemical processes in the swelling zone, which may be induced by human activities such as geothermal drilling, remain difficult to assess or even predict.

This thesis investigates the significance of 1) the local geological setting, 2) hydrology and geochemistry of the swelling zone and 3) their modification upon human activities (geothermal drilling), as well as 4) the reaction kinetics of the anhydrite-gypsum-water system at the field scale, to the swelling process. For this purpose, a 3D geological model of the study site is developed in the first part of this thesis. It provides the geometric basis for the subsequent numerical investigations of the hydrogeological and geochemical processes of the swelling phenomenon. Furthermore, an uncertainty analysis based on the theory of information entropy is performed which allows for a detailed, voxel-based visualization and quantification of the differences and changes in uncertainty between multiple model interpretations. The approach is complemented by the Jaccard and City-block distance measures to identify dissimilarities between the model realizations and changes in model geometry. The results show that with higher data density the number of identified geological structures as well as the occurrence of locally high structural uncertainty can increase. In addition, the methodology enables more efficient geological exploration campaigns and also provides a sound basis for cost-benefit analysis.

In the second part of the thesis, a novel modeling approach for the swelling phenomenon is developed and numerically implemented as a radially symmetric, reactive transport model. The approach accounts for changing hydraulic and geochemical conditions due to human activities, as well as water availability in the swelling zone. For this purpose, swelling-induced heave at the ground surface is simu-

lated and quantified as a function of the geochemical transformation of anhydrite into gypsum in the subsurface and the local stress conditions exerted by the overburden. The modeling approach differentiates between advective transport along preferential flow paths in the rock and the transformation of anhydrite into gypsum in the rock matrix. A dual-domain approach is used in order to assign specific porosities to both domains and couple them via a transfer rate for diffusive transport. Process-specific hydraulic, geochemical, and mechanical model parameters are estimated through an inversion process, constrained by geodetic uplift data. The results show that reaction rate constants for anhydrite dissolution ( $2.4 \times 10^{-5} \text{ mol m}^{-2} \text{ s}^{-1}$ ) and gypsum precipitation ( $3.2 \times 10^{-6} \text{ mol m}^{-2} \text{ s}^{-1}$ ) are comparable with literature values from laboratory experiments. It also becomes apparent that the rate of the chemical transformation is significantly influenced by diffusive mass transport into the rock matrix, which may be a limiting factor to the swelling process, especially at low rock porosities (e.g. compact anhydrite layers). Overall, the proposed reactive transport modeling approach reproduces the observed swelling-induced heave at the study site with a plausible parameterization.

In the third part, the previously developed reactive transport modeling approach is applied to the complex geological setting at the study site in order to explicitly account for the impact of geothermal drilling and subsequent mitigation measures on local groundwater flow and thus, the swelling phenomenon. The focus is on predicting the further development of swelling-induced heave as a function of possible countermeasures, in order to provide a scientific basis for evaluating strategies to stop the swelling process. For this purpose, the swelling process is simulated for three different mitigation scenarios and water inflows into the swelling zone is located and quantified. The results show that even with an incomplete, subsequent sealing of the geothermal drillings, the flow of water into the swelling zone and thus the swelling process can be stopped by appropriate hydraulic countermeasures. They also highlight that comprehensive geological, hydraulic and geochemical information is needed for a substantive simulation of the swelling processes and to assess suitable site-specific remediation measures.

## KURZFASSUNG

---

Quellende Ton-Sulfatgesteine führen immer wieder zu unvorhergesehenen Problemen im Tunnelbau oder bei oberflächennahen Geothermiebohrungen und machen dort langwierige Sanierungsmaßnahmen erforderlich. Die Prozesse, die dem Quellen zugrunde liegen, sind komplex. Im Allgemeinen wird davon ausgegangen, dass der Quellvorgang hauptsächlich auf die Umwandlung von Anhydrit zu Gips zurückzuführen ist. Auslöser ist in der Regel eine Änderung der hydraulischen Bedingungen, gefolgt von einem Wasserzutritt in die quellfähigen Gesteinsschichten, was wiederum die vorherrschenden geochemischen Bedingungen verändert. In der Folge kommt es zu einer Zunahme des Gesteinsvolumens im Untergrund. Dies führte in der süddeutschen Stadt Staufeu, dem Untersuchungsstandort dieser Arbeit, zu großräumigen Hebungen an der Geländeoberfläche und, damit verbunden, zu großen Schäden an Häusern und Infrastruktur. Gerade diese hydrogeologischen und geochemischen Prozesse, sowie der Einfluss menschlicher Aktivitäten (z.B. Geothermiebohrungen), lassen sich jedoch nur sehr schwer nachvollziehen oder gar vorhersagen, da die genauen Zusammenhänge bisher unzureichend erforscht sind.

Im ersten Teil dieser Arbeit wird zunächst ein 3D geologisches Modell entwickelt, um die komplexen geologischen Verhältnisse im Untersuchungsgebiet zu rekonstruieren. Dieses Modell stellt die geometrische Grundlage für die im weiteren Verlauf durchgeführten numerischen Untersuchungen der hydrogeologischen und geochemischen Prozesse des Quellphänomens dar. In diesem Zusammenhang wird außerdem eine Unsicherheitenanalyse der 3D geologischen Modellierung basierend auf der Theorie der Informationsentropie durchgeführt. Die Analyse veranschaulicht wie sich verschiedene geologische Erkundungsdaten unterschiedlich auf die vorhandenen Modellunsicherheiten und die Modellgeometrie auswirken. Der erstmals auf ein komplexes Standortmodell angewendete Ansatz ermöglicht dabei eine detaillierte, Voxel-basierte Visualisierung und Quantifizierung der Unterschiede und Änderungen der Unsicherheit zwischen mehreren Modellinterpretationen. Zusätzlich können mit Hilfe der verwendeten Jaccard- und der City-block-Distanzen Unähnlichkeiten zwischen den Modellen direkt identifiziert werden. Damit ermöglicht die Methodik unter anderem eine effizientere Durchführung von geologischen Erkundungskampagnen und bietet außerdem eine fundierte Grundlage für Kosten-Nutzen-Analysen. Für die komplexen geologischen Verhältnisse des Untersuchungsstandorts Staufeu zeigt sich, dass mit zunehmender Datendichte mehr geologische Struktu-

ren identifiziert werden, gleichzeitig aber auch vermehrt lokal hohe strukturelle Unsicherheiten auftreten.

Im zweiten Teil der Arbeit wird ein neuartiger Modellansatz entwickelt und numerisch als radialsymmetrisches, reaktives Transportmodell umgesetzt. Das Modell kann genutzt werden, um den Quellprozess abzubilden und berücksichtigt folgende Einflüsse: 1) die veränderten hydraulischen Randbedingungen auf Grund menschlicher Aktivitäten (Geothermiebohrungen), 2) die Wasserverfügbarkeit in der Quellzone, und 3) die Geochemie. Dazu wird die Quellhebung an der Geländeoberfläche in Abhängigkeit der geochemischen Umwandlung von Anhydrit in Gips und einer daraus abgeleiteten Volumenzunahme im Untergrund simuliert und quantifiziert. Der Modellansatz trennt dabei zwischen advektivem Stofftransport entlang von Klüften im Gestein und der Umwandlung von Anhydrit zu Gips in der Gesteinsmatrix. Um den beiden Wirkungsbereichen (Domänen) spezifische Porositäten zuordnen zu können, wird ein Zwei-Domänen Modellierungsansatz ("dual domain approach") verwendet, der diese gleichzeitig über eine Transferrate für den diffusiven Wassertransport koppelt. Mit diesem Modellansatz können prozessspezifische hydraulische, geochemische und mechanische Modellparameter basierend auf geodätischen Hebungsdaten in einer inversen Modellierung abgeschätzt werden. Die hierbei ermittelten Reaktionskonstanten für Anhydritlösung ( $2.4 \times 10^{-5} \text{ mol m}^{-2} \text{ s}^{-1}$ ) und Gipsfällung ( $3.2 \times 10^{-6} \text{ mol m}^{-2} \text{ s}^{-1}$ ) sind vergleichbar mit Literaturwerten aus Laborversuchen. Es zeigt sich jedoch, dass der diffuse Stofftransport in die Gesteinsmatrix wesentlich die Geschwindigkeit des Quellprozesses beeinflusst, was insbesondere bei niedrigen Gesteinsporositäten (z. B. kompakte Anhydritlagen) ein limitierender Faktor sein kann. Insgesamt ist das Modell in der Lage, den am Untersuchungsstandort beobachteten Hebungsverlauf abzubilden.

Im dritten Teil der Arbeit wird das zuvor entwickelte Quellhebungsmodell auf die komplexe geologische Situation am Untersuchungsstandort Staufen angewendet. Dadurch können, im Vergleich zum radialsymmetrischen Ansatz, sowohl lokale Grundwasserströmungen, als auch die örtlichen geologischen Gegebenheiten explizit und umfassend bei der Simulation des Quellprozesses berücksichtigt werden. Das Modell kann genutzt werden, um eine Prognose über die weitere Entwicklung der Hebungsprozesse in Abhängigkeit der Sanierungsmaßnahmen vorzunehmen und bietet damit die wissenschaftliche Grundlage für eine Bewertung verschiedener Strategien, um den Quellprozess zu stoppen. Die Methode ermöglicht eine Bilanzierung der Wasserzuflüsse in die Quellzone, sowie eine Abschätzung des zukünftigen Quellpotentials für individuelle Sanierungsszenarien. Für den Untersuchungsstandort Staufen zeigen die Ergebnisse, dass auch bei einer unvollständigen, nachträglichen Abdichtung der Erdwärmesonden der Wasserfluss in die Quellzone und damit

der Quellprozess durch entsprechende hydraulische Gegenmaßnahmen gestoppt werden kann. Außerdem wird ersichtlich, dass umfassende geologische, hydraulische und geochemische Informationen für eine stichhaltige Simulation der Quellprozesse und eine Beurteilung geeigneter standortspezifischer Sanierungsmaßnahmen erforderlich sind.



Part I

INTRODUCTION



## INTRODUCTION

---

In April 2017 the *Stuttgarter Zeitung* wrote:

*“Die Geothermie-Katastrophe in Staufeu - Eine Stadt in Bewegung: Eine Geothermiebohrung unterm Rathaus ließ Staufeu aus den Fugen geraten. Zehn Jahre später bewegt sich der historische Stadtkern noch immer. Wann der Aufruhr unter der Erde ein Ende findet, kann keiner sagen.” Keck, 2017*

What happened in the city of Staufeu im Breisgau, Germany, is a direct consequence of swelling clay-sulfate rocks. The spectacular incident described here not only lead to severe damage to buildings exceeding 50 Mio. € (Fleuchaus and Blum, 2017) and uncertainty in the population regarding the ground source heat pump (GSHP) technology, it also illustrates the key issue associated with the swelling process: its unpredictability.

*Once the swelling starts there is no telling when it stops*

In general, the cause of swelling in clay-sulfate rocks and the principal mechanisms of swelling are known. The swelling is triggered by water ingress into rocks containing expansive clay and sulfate minerals which increase their volume by absorbing water. This phenomenon is particularly pronounced in the geological formations of the Triassic Gipskeuper (“Gypsum Keuper” or Grabfeld-Fm.), commonly found in north-western Switzerland (Jura Mountains) and in south-western Germany.

Besides recent incidents in connection with GSHP installations in the Gipskeuper (Fleuchaus and Blum, 2017), the swelling phenomenon is also of major concern in tunnel engineering where it causes severe damage, lengthy disruption of operation and costly repairs (e.g., Alonso, I. Berdugo, et al., 2013; Amstad and Kovári, 2001; I. R. Berdugo et al., 2009a,b; Einstein, 1996; Steiner, 1993). In this context, several theoretical and constitutive models have been proposed which describe the relationship between pressure (stress) and heave (strain) as well as the time dependency of the swelling process to facilitate predictions about the swelling behavior of the rock (e.g., Grob, 1972; Gysel, 1977; Kirschke, 1995; E. Pimentel, 2007, reviewed in Butscher et al., 2018) and to provide a rational basis for engineering measures that counteract the swelling (Kovári and Chiaverio, 2007; Pierau and Kiehl, 1996). However, reliable experimental results supporting these models are scarce, since the swelling process takes an extremely long time to reach a steady state (equilibrium), even under optimal laboratory conditions. Thus, tests are lengthy and usually terminated prematurely. Furthermore, existing data are not necessarily comparable as

*A swelling law for the stress-strain relationship may not exist*

experimental setups differ, making the search for a constitutive model of the swelling behavior even more difficult. Ultimately it remains questionable, whether the spatial-temporal evolution of the swelling process in clay-sulfate rocks can be adequately described without fully considering the underlying processes and controls (Butscher, Breuer, et al., 2018; Butscher, Mutschler, et al., 2016). These include but are not limited to interactions between mechanical behavior, material properties, hydrogeological and geochemical processes as well as the prevailing geological conditions. In describing these relationships, purely analytical approaches are limited.

*Processes and controls are manifold and complex*

Process-based numerical models coupling thermal, hydraulic, mechanical and chemical processes are therefore the most promising approach for describing the swelling behavior of clay-sulfate rocks. In recent years a number of coupled numerical models were developed to investigate the swelling process and its controls in more detail. For example, Anagnostou (1993, 1995) treated the swelling phenomenon as a hydraulic-mechanical coupled process in order to study the effect of seepage flow on the development of heave and pressure in tunnels over the course of time. And coupling with geochemical processes, in particular with regard to the role of sulfate minerals, was advanced by Alonso and Olivella (2008), Oldecop and Alonso (2012), Ramon and Alonso (2013, 2018), and Ramon, Alonso, and Olivella (2017). However, although these models have been successfully used to simulate swelling deformation observed in tunnels, bridges, and buildings, their general applicability and predictive capabilities remain limited by still existing gaps in the overall understanding of the swelling process. Addressing these gaps and ultimately improving our ability to predict swelling behavior in clay-sulfate rocks is the main topic I address in my thesis.

*Improved process understanding through numerical modeling*

### 1.1 THE SWELLING MECHANISM: UNDERLYING PROCESSES AND CONTROLS

The swelling mechanism in clay-sulfate rocks involves both “sulfate swelling” and “clay swelling”, which superimpose each other (Madsen and Nuesch, 1991). Clay swelling is either the result of an osmotic water uptake driven by a concentration gradient between the clay matrix and the free pore water (Gonçalvès et al., 2010), or it is due to the hydration of clay minerals such as smectites (crystalline swelling), i.e. the intercalation of discrete layers of water molecules (Laird, 2006; Madsen and Müller-Vonmoos, 1989). Similarly, sulfate swelling is a hydration reaction in which water is incorporated into the crystal lattice of the mineral anhydrite ( $\text{CaSO}_4$ ) to form gypsum ( $\text{CaSO}_4 \cdot \text{H}_2\text{O}$ ):

*Sulfate swelling is main mechanism of swelling in clay-sulfate rocks*



As a result of this chemical transformation the specific volume of the sulfate increases by 60.8% if swelling is unconfined (Figure 1.1).

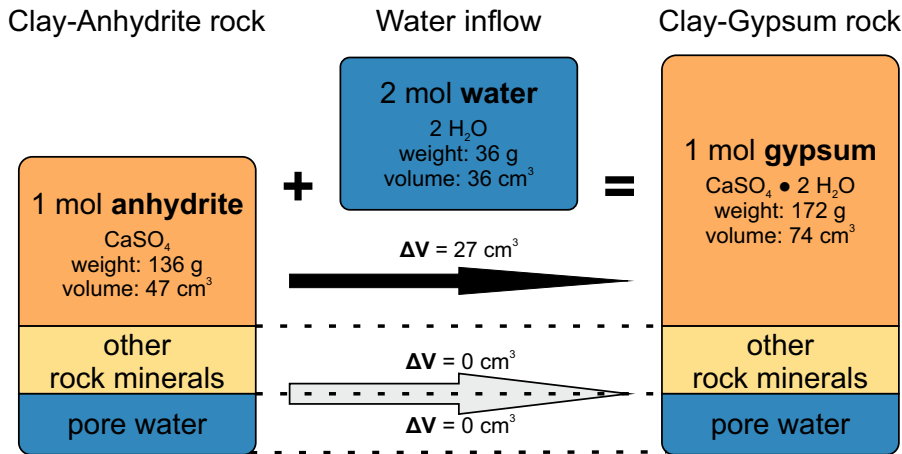


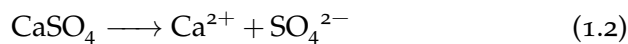
Figure 1.1: Volume and mass balance of the chemical transformation of anhydrite into gypsum caused by the uptake of water. The volume increase of the sulfate is approximately 61%.

However, if volumetric strain is prevented, high swelling pressures may occur in clay-sulfate rocks. In-situ and laboratory measurements of maximum swelling pressures in the Gipskeuper formation reach 5 MPa and 16 MPa, respectively (Hauber et al., 2005; Henke et al., 1975; Steiner, 1993). Although the observed swelling pressures widely differ, they exceed those encountered in pure clay swelling (Gonçalvès et al., 2010; Madsen and Müller-Vonmoos, 1989). Hence, sulfate swelling is considered to be the predominant mechanism of swelling in clay-sulfate rocks (e.g., Wittke, 2014).

Nevertheless, the swelling potential decisively depends on the type of clay minerals present alongside the amount of clay fraction. While massive pure anhydrite layers do not develop extensive swelling (Einstein, 1996; Steiner, 1993), swelling in clay-sulfate rocks is maximal at 15% clay (Madsen and Nuesch, 1991), as well as where the clay mineral corrensitite (i.e. a mixed layer clay chlorite-smectite variation) is abundant (Lippmann, 1976). A possible explanation is that in the presence of clay minerals the otherwise almost impermeable anhydrite layers are disintegrated by clay swelling, as clay minerals favor osmotic flow of water into the rock. However, the exact role of clay in the swelling of clay-sulfate rocks remains inconclusive. There are several other hypothesis on the role of clay, some of which are summarized by Butscher, Mutschler, et al. (2016).

*Clay minerals play a crucial but ambiguous role in clay-sulfate swelling*

In an open system, such as a natural rock formation, the transformation of anhydrite into gypsum is decoupled through the circulation of water (i.e. through groundwater flow and diffusion, Figure 1.2). Anhydrite dissolves in the pore water:



and gypsum subsequently precipitates out of the solution:



Consequently, the saturation states and stability fields of both sulfate minerals strongly depend on the prevailing pore water chemistry, but also temperature and pressure (e.g., Blount and Dickson, 1973; Dai et al., 2017; Freyer and Voigt, 2003; Hardie, 1967; Hill, 1937; MacDonald, 1953; Marsal, 1952; Partridge and A. H. White, 1929; Serafeimidis and Anagnostou, 2014a,b). In general, low-pressure and low-temperature conditions prevail in clay-sulfate rocks problematic to engineering activities (e.g., tunneling and geothermal drilling). Under these conditions, the solubility of anhydrite is typically higher than that of gypsum. Thus, gypsum being the mineral with the lower solubility (equilibrium concentration) is the stable mineral phase and the precipitate (Figure 1.2). The resulting decrease in calcium and sulfate ion concentration in solution maintains a continuous state of under-saturation with respect to the mineral anhydrite. In clay-sulfate rocks the kinetically controlled process continues to occur until all the anhydrite has been consumed, and it is typically even further propelled by the ingress of water already under-saturated in respect to anhydrite.

*Gypsum is the stable mineral phase and precipitates*

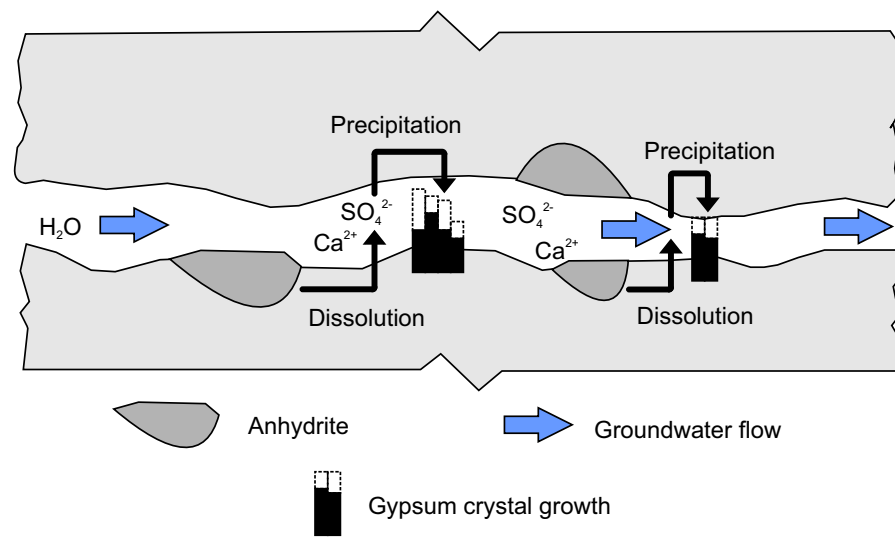


Figure 1.2: Conceptual model for swelling by crystal growth (gypsum precipitation) in a system open to water flow. From Alonso (2012) and Ramon (2014), modified.

Various authors have investigated the reaction kinetics and evolution of such systems under controlled laboratory conditions to provide, for example, an estimate of the reaction rate constants (e.g., J. Christoffersen and M. R. Christoffersen, 1976; Jeschke and Dreybrodt, 2002; Kontrec et al., 2002; Zorn et al., 2009). Actual reaction kinetics at the field scale, however, are difficult to predict as they depend on many different factors, most of which may vary widely in space

*Reaction kinetics of the anhydrite-gypsum-water system*

and time. They include rock characteristics (composition, texture, orientation), the distribution of anhydrite (shape, size) and the specific reactive surface area (e.g., Rauh and Thuro, 2007; Serafeimidis and Anagnostou, 2012a,b).

Furthermore, the reaction kinetics depend on the hydrodynamic conditions of the system, because they determine solute transport and water accessibility within the clay-sulfate rocks (Jeschke, Vosbeck, et al., 2001). During the swelling processes, the hydrodynamic conditions may change on the micro-scale due to, for example, rock disintegration form clay swelling or gypsum crystal growth in discontinuities (Alonso, 2012; Wittke, 2014). However, they are also altered at the macro-scale by engineering activities (Butscher, Einstein, et al., 2011; Scheidler et al., 2017). Hence, in order to develop predictive models of the swelling behavior of clay-sulfate rocks, a comprehensive understanding of the controlling hydrogeological and geochemical conditions and processes as well as the influence of engineering activities is essential.

*Hydrodynamic conditions influence the swelling process*

## 1.2 OBJECTIVES

This thesis is part of the DFG research project “Integrated hydrogeological and geochemical processes in swelling clay-sulfate rock”, with the overall objective to better understand the hydrogeological and geochemical processes involved in the swelling of clay-sulfate rocks, ultimately improving predictions of the swelling behavior. More specifically, a reactive transport model will be developed which can be used to investigate the hydrodynamic conditions and how these, together with the geochemistry of the swelling zone, change on the field scale through engineering activities (e.g., geothermal drilling). In addition, a particular focus is on evaluating the prevailing geological conditions, as these determine the maximum extent of the swelling zone and the hydro-geochemical conditions therein and therefore must be reliable in order to be used as the geometric basis of a complex numerical model. To address these objectives, a specific study site in Staufen im Br., Germany is investigated in this thesis, with Chapter 2, 3, and 4 each focusing on a particular set of research goals:

- Chapter 2 aims to provide a adequate representation of the sub-surface structure (i.e. a geological model) in the light of existing uncertainty in the geological information in order to locate the expansive anhydrite-bearing rock strata that constitute the swelling zone. Knowledge of the exact location and extent of the swelling zone is essential to be able to associate the observed heave at the ground surface with the swelling process itself. For this purpose, a focus was placed on assessing the uncertainty in 3D geological models, and how these uncertainties, as well as model geometry, and general structural understanding are

affected by different types of geological data. Thus, a methodology is provided to systematically assess interpretations of geological structures, taking into account the available geological information at a particular location.

- Chapter 3 aims to develop a novel conceptual and numerical modeling approach that can be used to study the effect of groundwater flow, the associated availability of water and changing geochemical conditions, on the swelling process. Another goal is to propose reaction rate constants for anhydrite and gypsum, which describe the observed swelling on the field scale.
- And Chapter 4 aims to improve the scientific basis for assessing the effectiveness of various mitigation measures in counteracting the swelling process by simulating their impact on hydraulic and geochemical conditions on a field scale. At the same time an attempt is made to predict the development of the swelling process.

Through accomplishing the above goals, this thesis aims to serve as a bridge between application-oriented problems and a basic understanding of the underlying processes.

### 1.3 STUDY SITE

The study site of this thesis is situated in Staufen im Br., southwest Germany. The town lies at the eastern border of the Upper Rhine Graben within the “Sulzburg-Staufener Vorbergzone” (Genser, 1958). The geological strata present in this zone range from Tertiary sediments at the top to crystalline bedrock at the bottom. The bedrock of the study site itself is mainly steeply inclined Mesozoic strata covered by quaternary sediments (Sawatzki and Eichhorn, 1999). They are strongly fragmented by a fault system with a releasing bend geometry, kinematically linked to the Eastern Main Border Fault (EMBF) (Behrmann et al., 2003). Faults are typically west-dipping with a large normal displacement, while faults oriented perpendicular to the EMBF cause further segmentation. This results in a geological setting that is complex and not fully mapped (LGRB, 2010).

Overall, the formations most relevant to the thesis are (from top to bottom) the Schilfsandstein (Stuttgart-Fm.), Gipskeuper (Grabfeld-Fm.), Lettenkeuper (Erfurt-Fm.) and Upper Muschelkalk (Rottweil-Fm.). The marlstone and claystone of the Gipskeuper contain the swelling-prone sulfates, whereas the dolomitic limestone of the Lettenkeuper and the karstified limestone of the Upper Muschelkalk represent the most important aquifers at the study site.

In 2007, a geothermal drill campaign for the installation of seven borehole heat exchangers (BHE) was carried out in these strata as an

energy-related refurbishment measure of the historic town hall. Almost immediately thereafter, first cracks were found on buildings as a result of ground displacement. Measured uplift rates reached  $11 \text{ mm month}^{-1}$  (LGRB, 2010), with a total uplift of nearly 60 cm by 2018. In total, more than 250 houses were damaged and the costs attributable to the swelling process amount to more than 50 Mio. € (Fleuchaus and Blum, 2017). The observed ground heave was caused by a change in hydro-geochemical conditions in the clay-sulfate rocks of the Gipskeuper, which triggered the chemical transformation of anhydrite to gypsum, followed by a net increase in rock volume. Water from the artesian aquifers of the Lettenkeuper and Upper Muschelkalk was likely able to access the swelling zone along at least one of the BHE drillings due to an incomplete annular sealing. Mitigation measures aimed at stopping the swelling process started in 2009 and were able to partially negate the ground heave by preventing further inflow of water into the swelling zone. This was accomplished by grouting the BHE to seal the annular space, and by the installation of pumping wells to cause permanent drawdown of the groundwater level in the underlying aquifers. Nevertheless, the ground surface heave is likely to continue until all water that has already ingressed into the swelling zone is consumed by the swelling process.

In order to assess the cause of the observed ground heave in Staufen and to plan appropriate mitigation measures a comprehensive exploration program was undertaken that collected extensive data on the geological, hydrogeological, geochemical and geomechanical conditions at the study site. They have been published in two reports (LGRB, 2010, 2012) and are freely available under the following URL: <https://lgrb-bw.de/geothermie/staufen>. Furthermore, a geodetic monitoring network was established to collect data on the ground heave. The scope and variety of available data provide the best possible conditions for a detailed investigation of the swelling process, which is why this study site was chosen.

#### 1.4 STRUCTURE OF THE THESIS

This cumulative thesis consists of three self-contained studies, which are enclosed in Chapter 2, 3, and 4. All studies were submitted to peer-reviewed (ISI-listed) international journals, with the first two of them already being published and the study in Chapter 4 being under review. The synthesis in Chapter 5 presents a summary and establishes a connection of the results and findings of the three individual studies, followed by a discussion and outlook.

The chapters are organized as follows:

- Chapter 2: *Uncertainty assessment in 3D geological models of increasing complexity*

An uncertainty analysis based on the theory of information entropy is performed. In this context, several geological 3D models of increasing complexity and with different geological input data categories are created for the study site Staufen. The information entropy is used to evaluate structural uncertainties and capture changes between these models, and to compare multiple model interpretations. Accordingly, differences and changes in uncertainty between the models are visualized, quantified and discussed. In addition, the Jaccard and City-Block distance measures are employed to quantify dissimilarities between the models.

- Chapter 3: *Reactive transport modeling of swelling processes in clay-sulfate rocks*

A numerical modeling approach is proposed that quantifies the swelling-induced heave at the ground surface as a function of the geochemical transformation from anhydrite to gypsum, while emphasizing the role of both groundwater flow and prevailing geochemical conditions. As a central part of the presented study, a conceptual model of the swelling process is introduced, which allows a separate consideration of solute transport along discontinuities and the chemical transformation of anhydrite into gypsum in the rock matrix by means of a dual-domain modeling approach. Furthermore, inverse modeling is used in order to estimate model-specific parameters such as the reaction rate constants of anhydrite and gypsum, and to analyze parameter uncertainties. The inversion process is constrained by geodetic measurement data, thus maximizing the fit between measured and simulated heave at the ground surface, while considering plausible parameter values.

- Chapter 4: *Analyzing the heave of an entire city: modeling of swelling processes in clay-sulfate rocks*

A case study is presented that employs the reactive transport modeling approach and the geological model developed in the previous two chapters to examine different mitigation measures, while assessing their efficiency in counteracting the swelling process. Mitigation scenarios are discussed with regards to their influence on water ingress into the swelling zone and water availability for the transformation of anhydrite into gypsum. In this context, a method is introduced that approximates the swelling-induced heave at the ground surface as a function of the volume increase of a spherical source, which is embedded in an isotropic elastic half-space (Mogi model). Model simulations predict the progress of uplift and the potential for future swelling is evaluated. In addition, the transferability and application of hydraulic countermeasures are assessed on the basis

of a similar incident of swelling-induced heave at the ground surface in Böblingen, Germany.

- Chapter 5: *Synthesis and Discussion*

The major results of the individual studies are summarized and their contribution towards an improved understanding of the swelling phenomenon is discussed. In addition, the coupling of processes and the assessment of uncertainties, which represent key issues of the presented modeling approach, are elaborated upon with a focus on opportunities for future research.

Although the individual chapters focus on different aspects relevant to the swelling process in clay-sulfate rocks, due to this organization of the thesis, there are some repetitions. This applies in particular to the sections describing the study site or previous research on clay-sulfate rocks.



## Part II

### UNCERTAINTY ASSESSMENT IN 3D GEOLOGICAL MODELS OF INCREASING COMPLEXITY

This study is published in the EGU journal *Solid Earth*.  
Part II is a reprint of:

Schweizer, D., Blum, P., & Butscher, C. (2017).  
Uncertainty assessment in 3-D geological models of  
increasing complexity. *Solid Earth*, 8(2), 515–530.  
doi:[10.5194/se-8-515-2017](https://doi.org/10.5194/se-8-515-2017)



## PART 2: UNCERTAINTY ASSESSMENT IN 3D GEOLOGICAL MODELS

---

### ABSTRACT

The quality of a 3D geological model strongly depends on the type of integrated geological data, their interpretation and associated uncertainties. In order to improve an existing geological model and effectively plan further site investigation, it is of paramount importance to identify existing uncertainties within the model space. Information entropy, a voxel based measure, provides a method for assessing structural uncertainties, comparing multiple model interpretations and tracking changes across consecutively built models. The aim of this study is to evaluate the effect of data integration (i.e. update of an existing model through successive addition of different types of geological data) on model uncertainty, model geometry and overall structural understanding. Several geological 3D models of increasing complexity, incorporating different input data categories, were built for the study site Staufen (Germany). We applied the concept of information entropy in order to visualize and quantify changes in uncertainty between these models. Furthermore, we propose two measures, the Jaccard and the City-Block distance, to directly compare dissimilarities between the models. The study shows that different types of geological data have disparate effects on model uncertainty and model geometry. The presented approach using both information entropy and distance measures can be a major help in the optimization of 3D geological models.

### 2.1 INTRODUCTION

Three dimensional (3D) geological models have gained importance in structural understanding of the subsurface and are increasingly used as a basis for scientific investigation (e.g., Bistacchi et al., 2013; Butscher and Huggenberger, 2007; Caumon, Collon-Drouaillet, et al., 2009; J. Liu et al., 2014), natural resource exploration (e.g., Collon et al., 2015; Hassen et al., 2016; Jeannin et al., 2013), decision-making (e.g., Campbell et al., 2010; Hou et al., 2016; Panteleit et al., 2013) and engineering applications (Hack et al., 2006; Kessler et al., 2008). 3D geological models are usually preferable over 2D solutions, because our object of study is intrinsically three dimensional in space and, therefore, they offer a higher degree of data consistency and superior data visualization. Moreover, they enable the integration of many different

types of geological data such as geological maps, cross-sections, outcrops, boreholes as well as data from geophysical (e.g., Boncio et al., 2004) and remote sensing methods (e.g., Schamper et al., 2014). Nevertheless, input data are often sparse, heterogeneously distributed or poorly constrained. In addition, uncertainties from many sources such as measurement error, bias and imprecisions, randomness and lack of knowledge are inherent to all types of geological data (Bárdossy and Fodor, 2001; Culshaw, 2005; Mann, 1993). Furthermore, assumptions and simplifications are made during data collection, and subjective interpretation is part of the modeling process (Bond, 2015). Hence, model quality strongly depends on the type of integrated geological data and its associated uncertainties.

In order to assess the quality and reliability of a 3D geological model as objectively as possible, it is essential to address underlying uncertainties. Numerous methods have recently been proposed that enable estimates, quantification and visualization of uncertainty (Kinkeldey et al., 2015; Lark et al., 2013; Lindsay, Aillères, et al., 2012; Lindsay, Jessell, et al., 2013; Lindsay, Perrouty, et al., 2014; Park et al., 2013; Tacher et al., 2006; Wellmann, Horowitz, et al., 2010). A promising approach is based on the concept of information entropy (Shannon, 1948). Wellmann and Regenauer-Lieb (2012) applied this concept to 3D geological models. In their study, they evaluated uncertainty as a property of each discrete point of the model domain by quantifying the amount of missing information with regard to the position of a geological unit (Wellmann and Regenauer-Lieb, 2012). They consecutively added new information to a 3D model and compared uncertainties between the resulting models at discrete locations and as an average value for the total model domain using information entropy as a quantitative indicator. Through their approach, they addressed two important questions: 1) How is model quality related to the available geological information and its associated uncertainties; and 2) how is model quality improved through incorporation of new information?

Wellmann and Regenauer-Lieb (2012) illustrated their approach using synthetic 3D geological models, showing how additional geological information affects model uncertainty. The present study goes a step further. It applies the concept of information entropy as well as model dissimilarity to a real case, namely the city of Staufen, Germany at the eastern margin of the Upper Rhine Graben. In contrast to the previous study, the present study evaluates the effects of consecutive addition of data from different data categories to an existing model on model uncertainty and overall model geometry. We hypothesize that disparate effects of different data types on model uncertainty exist, and that quantification of these effects provides a trade-off between costs (i.e. data acquisition) and benefits (i.e. reduced uncertainty and therefore higher model quality). Thus, several

3D geological models of the study site were consecutively built with increasing complexity; each of them based on an increasing amount of (real) categorized data. An approach was developed that uses information entropy and model dissimilarity for quantitative assessment of uncertainty in the consecutive models. Results indicate that the approach is applicable for complex and real geological settings. The approach has large potential as a tool to support both model improvement through successive data integration and cost-benefit analyses of geological site investigations.

## 2.2 STUDY SITE

The city of Staufen suffers from dramatic ground heave that resulted in serious damage to many houses (South-West Germany, Figure 2.1). Ground heave with uplift rates exceeding  $10 \text{ mm month}^{-1}$  started in 2007 after seven wells were drilled to install borehole heat exchangers for heating the local city hall (LGRB, 2010). After more and more houses in the historic city center showed large cracks, an exploration program was initiated by the State Geological Survey (LGRB) in order to investigate the case. Results showed that the geothermal wells hydraulically connected anhydrite-bearing clay rocks with a deeper aquifer, and resulting water inflow into the anhydritic clay rock triggered the transformation of the mineral anhydrite into gypsum (Ruch and Wirsing, 2013). This chemical reaction is accompanied by a volume increase that leads to rock swelling, a phenomenon typically encountered in tunneling in such rock (e.g., Alonso, 2012; Anagnostou, Pimentel, et al., 2010; Butscher, Huggenberger, and Zechner, 2011; Butscher, Mutschler, et al., 2016; Einstein, 1996), but recently also observed after geothermal drilling (Butscher, Huggenberger, Zechner, and Einstein, 2011; Grimm et al., 2014). The above mentioned exploration program aimed not only at finding the cause of the ground heave, but also at better constraining the complex local geological setting. The hitherto existing geological data were not sufficient to explain the observed ground heave, locate the geological units that are relevant for rock swelling, and plan counter measures.

Staufen is located west of the Black Forest at the eastern margin of the Upper Rhine Graben (URG). It is part of the "Vorbergzone" (Genser, 1958), a transition zone between the Eastern Main Border Fault (EMBF) of the graben and the graben itself. This zone is characterized by staggered fault blocks that got trapped at the graben margin during opening and subsidence of the graben. The strata of this transition zone are often steeply inclined or even vertical (Schöttle, 2005), and are typically displaced by west-dipping faults with a large normal displacement. The fault system, kinematically linked to the EMBF, has a releasing bend geometry and today experiences sinistral oblique movement (Behrmann et al., 2003). The major geological units at the site

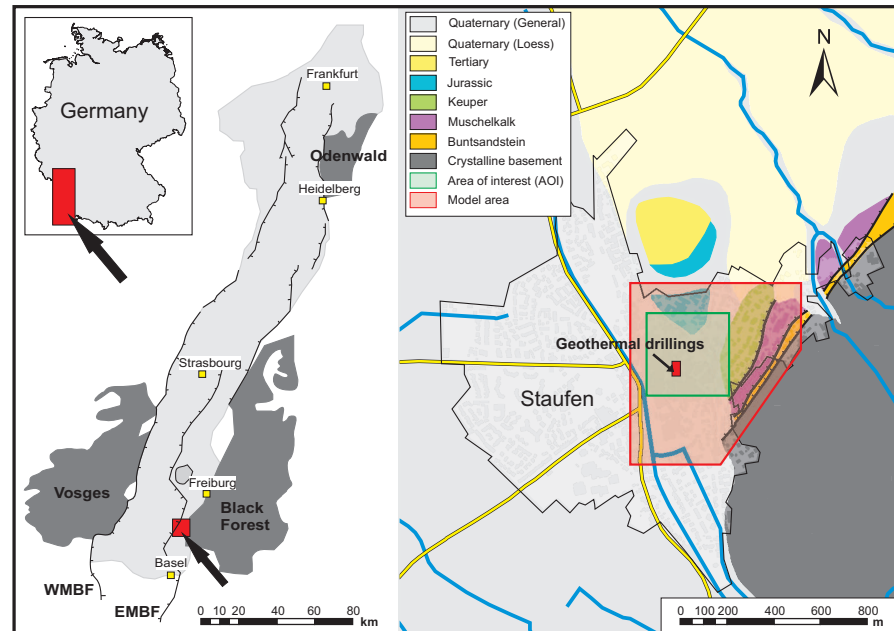


Figure 2.1: Study site and location of the model area and area of interest (AOI).

comprise Triassic and Jurassic sedimentary rocks, which are covered by Quaternary sediments of an alluvial plain in the south (Sawatzki and Eichhorn, 1999) (Figure 2.1).

Three geological units play an important role for the swelling problem at the site: the Triassic Gipskeuper “Gypsum Keuper”) formation, which contains the swelling zone; and the underlying Lettenkeuper formation and Upper Muschelkalk formation, which are aquifers providing groundwater that accesses the swelling zone via pathways along the BHE. The Gipskeuper formation consists of marlstone and mudstone, and contains the calcium-sulfate minerals anhydrite ( $\text{CaSO}_4$ ) and gypsum ( $\text{CaSO}_4 + \text{H}_2\text{O}$ ). The thickness of this formation varies between 50 to 165 m, with an average thickness of 100 to 110 m (LGRB, 2010), depending on the degree of leaching of the sulfate minerals close to the ground surface. It is underlain by the Lettenkeuper formation (5 to 10 m thickness), consisting of dolomitic limestone, sandstone and mudstone, and the Upper Muschelkalk formation ( $\approx 60$  m thickness) dominantly consisting of limestone and dolomitic limestone.

## 2.3 METHODS

### 2.3.1 Input data

Input data for the 3D geological modeling include all available geological data that indicate: 1) boundaries between geological units, 2) presence of geological units and faults at a certain positions and 3)

orientation (dip and azimuth) of the strata. These data were classified into four categories (Figure 2.2): 1) non-site specific, 2) site specific, 3) problem direct specific data and 4) indirect problem specific data.

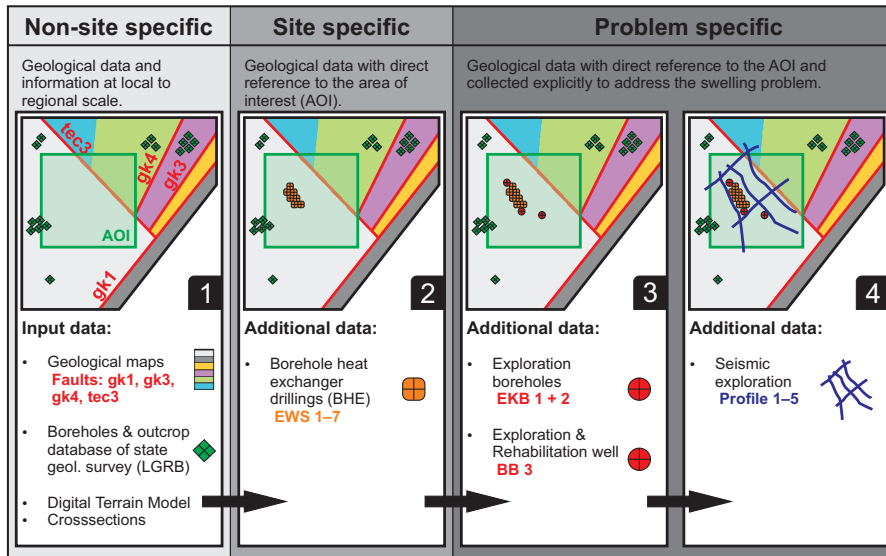


Figure 2.2: Data categories and geological input data used to build four initial 3D geological models. The green square indicates the area of interest (AOI), where data was extracted for further analysis. For geological formation color code see Figure 2.1.

The non-site specific data category comprise geological data that are generally available from published maps (Sawatzki and Eichhorn, 1999), literature (Genser, 1958; Groschopf et al., 1981; Schreiner, 1991) and the database of state geological survey (LGRB). Furthermore, a Digital Terrain Model (DTM) of 1.0 m grid size is included in the non-site specific data. Outcrop and borehole data are mostly scarce and irregularly distributed in space. The site specific data comprise drill logs of the geothermal drillings, which provided a pathway for up-rising groundwater that finally triggered the swelling. Problem specific data comprise all data collected during the exploration program that was conducted after heave at the ground surface caused damage to the local infrastructure (LGRB, 2010, 2012). This exploration program was initiated because geological knowledge of the site was insufficient for an adequate understanding of the swelling process in the subsurface; and for planning and implementing suitable counter measures. The problem specific data were further divided into direct data from drill cores of the three exploration boreholes (Figure 2.2; EKB 1 + 2 and BB 3), which add very accurate point information; and indirect data from a seismic campaign (Figure 2.2; Profile 1-5), which add rather “fuzzy” 2D information that have to be interpreted.

### 2.3.2 3D geological modeling

The 3D geological models were constructed using the geomodeling software SKUA/GoCAD<sup>®</sup> 15.5 by Paradigm. They cover an area of about 0.44 km<sup>2</sup> and have a vertical extent of 665 m. A smaller area of interest (AOI, 300 m × 300 m, 250 m vertical extent) was defined within the model domain, including the drilled wells and the area, where heave at the ground surface was observed and the problem specific data were collected.

The strata of the models cover 10 distinct geological units including Quaternary sediments, Triassic and Jurassic bedrock and crystalline basement at the lower model boundary (Figure 2.3). The Triassic strata is further divided (from top to bottom) into four formations of the Keuper (Steinmergelkeuper, Schilfsandstein, Gipskeuper and Lettenkeuper), two formations of the Muschelkalk (Upper Muschelkalk, Middle to Lower Muschelkalk) and the Bundsandstein formation. Figure 2.3 provides an overview over the modeled geological units and average thicknesses used in the initial models.

Stratigraphy (LGRB, 2010; Groschopf et al., 1981)				Thickness (m)	Abbr.	Model	
						Abbr.	Average thickness (m)
Quaternary					q		
Jurassic	Middle Jura	Hauptrogenstein	60–70	jm	j	240	
		Opalinuston	80–100				
	Lower Jura		70–80	ju			
Triassic	Upper	Rhät	2	ko	km3	60	
	Keuper Middle	Steinmergelkeuper	20–80	km3	km2	10	
		Schilfsandsteinkeuper	5–40	km2	km1	100	
		Gipskeuper	50–165	km1	ku	10	
	Lower	Lettenkeuper	5–10	ku	mo	60	
	Upper Muschelkalk		60–80	mo	mm–mu	70	
	Middle Muschelkalk		25–100	mm	so	45	
	Lower Muschelkalk		35–40	mu			
Upper Bundsandstein		10–70	so				
Crystalline basement						base	

Figure 2.3: Stratigraphic overview of the study area and modeled geological units with average thicknesses.

Four initial models were consecutively build, according to the four previously described data categories. Model 1 was constructed based only on non-site specific data (maps, literature, etc.); Model 2 addi-

tionally considered site specific data (drill logs of the seven geothermal drillings); Model 3 also included “direct” problem specific data (exploration boreholes); and finally, Model 4 included “indirect” problem specific data (seismic campaign). Through this approach, data density and structural model complexity increase from Model 1 to 4; and the models required successively higher efforts in data acquisition in the field.

First, an explicit modeling approach (Caumon, Collon-Drouaillet, et al., 2009) was used to create representative boundary surfaces for the geological units and faults of the initial models, because the available input data was, in terms of spatial coverage, not sufficient to directly use an implicit approach. Discrete Smooth Interpolation (DSI) provided by GoCAD<sup>®</sup> was used as the interpolation method (J. L. Mallet, 1992), which resulted in Delaunay-triangulated surfaces for both horizons and faults. Subsequently, based on the explicitly constructed surfaces, a volumetric 3D model was built by implicit geological modeling, implemented in the software SKUA<sup>®</sup>. The implicit modeling approach uses a potential field interpolation considering the orientation of strata (Frank et al., 2007), and is based on the U-V-t concept (J.-L. Mallet, 2004), where horizons represent geochronological surfaces.

### 2.3.3 *Uncertainty assessment*

#### 2.3.3.1 *General approach*

Our approach for assessing uncertainties of the 3D geological models consists of four distinct steps (Figure 2.4):

- (I) Building the initial 3D geological models of increasing data density and structural complexity (see above).
- (II) Definition of fault and horizon uncertainties. Horizon uncertainties were specified in SKUA<sup>®</sup> by a maximum displacement parameter or by alternative surface interpretations, resulting in a symmetric envelope of possible surface locations around the initial surface. To constrain the shape of generated horizons, SKUA<sup>®</sup> uses a variogram that spatially correlates perturbations applied to the initial surfaces (Paradigm, 2015). Fault uncertainties were defined by a maximum displacement parameter and a Gaussian probability distribution around the initial fault surface (Caumon, Tertois, et al., 2007; Tertois and J.-L. Mallet, 2007).
- (III) Creation of 30 model realizations for each initial model based on the above defined surface variations, applying the Structure Uncertainty workflow of SKUA<sup>®</sup>.
- (IV) Extraction of the geological information from all model realizations for analysis, comparison and visualization. For this pur-

pose, the AOI was divided into a regular 3D grid of 5 m cell size, resulting in 180 000 grid cells. The membership of a grid cell to a geological unit was defined as a discrete property of each grid cell and extracted for all 30 model realizations. Based on these data, we calculated the probability of each geological unit being present in a grid cell in order to derive the information entropy at the level of: 1) a single grid cell, 2) a subset representing the area of extent of a geological unit and 3) the overall AOI. Furthermore, the fuzzy set entropy was calculated to determine the ambiguousness of the targeted geological units Gipskeuper (km<sub>1</sub>), Lettenkeuper (ku) and Upper Muschelkalk (mo) within the AOI. Calculations were conducted using the statistics package R (R Core Team, 2016). The underlying concepts and equations used to calculate probabilities and entropies are described in the following section.

### 2.3.3.2 Information entropy

The concept of information entropy (or Shannon entropy) was first introduced by Shannon (1948) and is well known in probability theory (Klir, 2005). It quantifies the amount of missing information and hence, the uncertainty at a discrete location  $x$ , based on a probability function  $P$  of a finite data set. When applied to geological modeling, information entropy expresses the "degree of membership" of a grid cell to a specific geological unit. In other words, information entropy quantitatively describes how unambiguously the available information predicts that unit  $U$  is present at location  $x$ . Information entropy was recently applied to 3D geological modeling by Wellmann, Horowitz, et al. (2010) and Wellmann and Regenauer-Lieb (2012) in order to quantify and visualize uncertainties introduced by imprecision and inaccuracy of geological input data. A detailed description of the method can be found in the cited references, and is briefly summarized here.

By subdividing the model domain  $M$  into a regular grid, a discrete property can be assigned to any cell at location  $x$  in the model domain. In a geological context, the membership of a grid cell to a geological unit  $U$  can be defined as such a property by an indicator function:

$$I_U(x) = \begin{cases} 1 & \text{if } x \in U \\ 0 & \text{otherwise} \end{cases} \quad (2.1)$$

Applied to all  $n$  realizations  $k$  of the model space  $M$ , the indicator function yields a set of  $n$  indicator fields  $I$  with each of them defining the membership of a geological unit as a property of a grid cell. Considering the combined information of all indicator fields, it follows that membership is no longer unequivocally defined at a location  $x$  and hence has to be expressed by a probability function  $P_U$ :

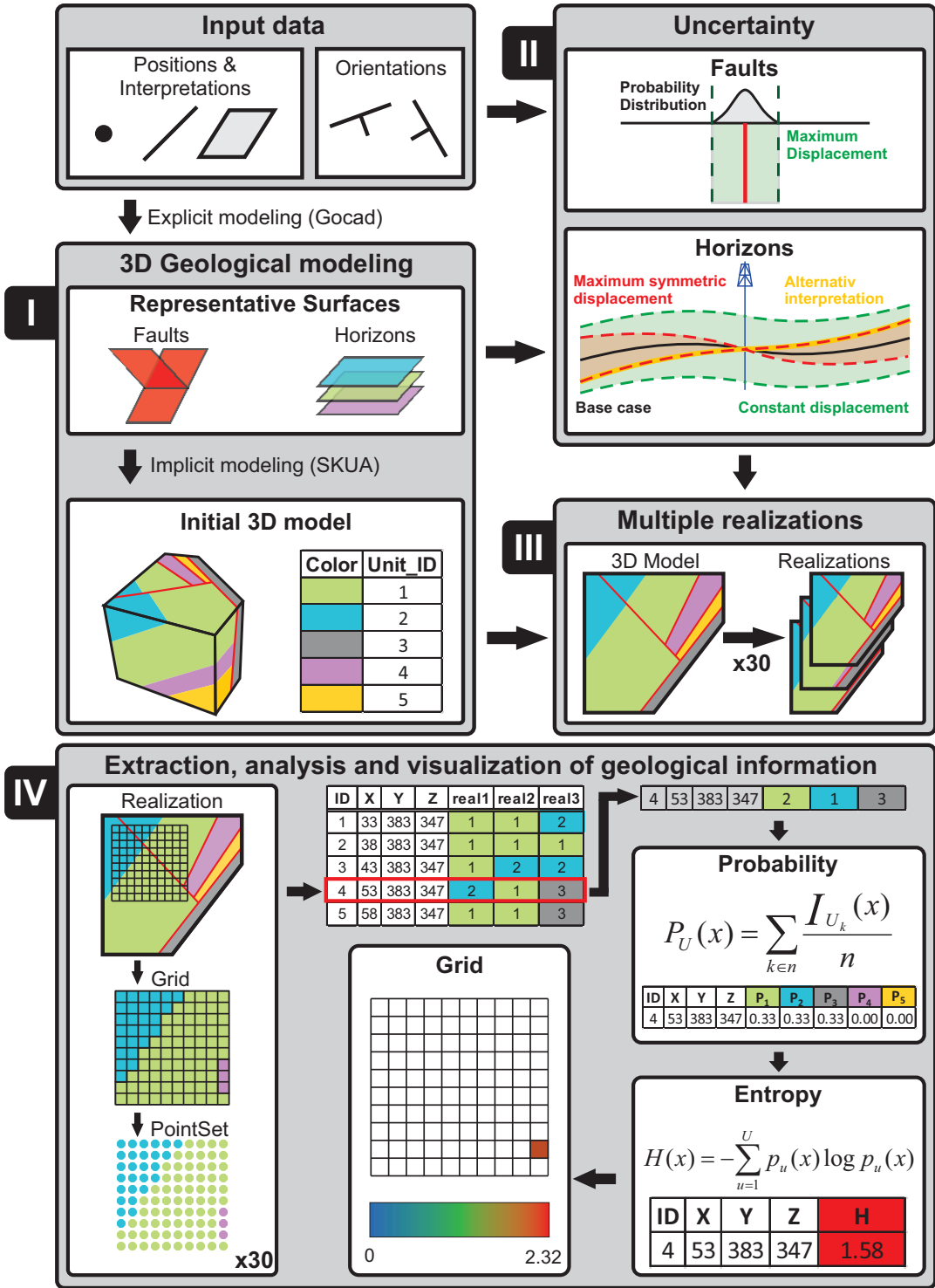


Figure 2.4: Uncertainty assessment workflow with four distinct steps. This workflow is applied to four initial models that are based on the different data sets illustrated in Figure 2.2.

$$P_x(\mathbf{U}) = \sum_{k \in n} \frac{I_{U_k}(x)}{n} \quad (2.2)$$

From the probabilities of occurrence  $P_x(\mathbf{U})$  the uncertainty (or amount of missing information) associated with a discrete point (grid cell) can be obtained by calculating the information entropy  $H_x$  (Shannon, 1948) for a set of all possible geological units  $\mathcal{U}$ :

$$H_x = - \sum_{\mathbf{U} \in \mathcal{U}} P_x(\mathbf{U}) \times \log P_x(\mathbf{U}) \quad (2.3)$$

In a next step, information entropy  $H_M$  can be calculated as an average value of  $H_x$  over the entire model space:

$$H_M = \frac{1}{|M|} \times \sum_{x \in M} H_x \quad (2.4)$$

where  $|M|$  is the number of elements within  $M$ ,  $H_M = 0$  denotes that the location of all geological units is precisely known (no uncertainty), and  $H_M$  is maximum for equally distributed probabilities of the geological units ( $P_{U1} = P_{U2} = P_{U3} = \dots$ ), which means that a clear distinction between geological units within the model space is not possible. Similarly, average information entropy can also be applied to only a subset of the model space ( $S \subseteq M$ ):

$$H_S = \frac{1}{|S|} \times \sum_{x \in S} H_x \quad (2.5)$$

$H_S$  can be used to evaluate the contribution of a specific sub-domain to overall uncertainty. In case of a drilling campaign, for example, the sub-domain can comprise a targeted depth or a geological formation of specific interest. In this study, we used the probability function  $P_x(\mathbf{U})$  with  $H_S$  conditioned by  $P_x(\mathbf{U}) > 0$  to define subsets within the model space. Thus, each subset represents the probability space of a geological formation of interest, namely the Lettenkeuper ( $S_{ku}$ ), Gipskeuper ( $S_{km1}$ ) and Upper Muschelkalk ( $S_{mo}$ ) formation.

Wellmann and Regenauer-Lieb (2012) also adapted fuzzy set theory (Zadeh, 1965) in order to assess how well-defined a single geological unit is within a model domain. A fuzzy set of  $n$  model realization introduces a certain degree of indefiniteness to a discrete property (e.g. membership of a geological unit), resulting in imprecise boundaries which can be referred to as fuzziness. The fuzziness of a fuzzy set (De Luca and Termini, 1972) in the context of a geological 3D model can be quantified by the fuzzy set entropy  $H_U$  (Leung et al., 1992; Yager, 1995):

$$H_U = -\frac{1}{N} \times \sum_{x=1}^N [P_x(\mathbf{U}) \log P_x(\mathbf{U}) + (1 - P_x(\mathbf{U})) \log(1 - P_x(\mathbf{U}))] \quad (2.6)$$

where the probability function  $P_x(U)$  with an interval  $[0,1]$  represents the degree of membership of a grid cell to a fuzzy set.  $H_U$  equals 0 when  $P_x(U)$  is either 0 or 1 everywhere within the set; and  $H_U$  equals 1 when all cells of the set have an equal probability of  $P_x(U) = 0.5$ .

#### 2.3.4 Model dissimilarity

The step-wise addition of input data to the models (see section 2.3.1) not only affects uncertainties associated with a geological unit, but also the geometry of the units, and therefore their position, size and orientation in space. New data may significantly change the geometry of a geological unit but only marginally change the overall uncertainty. Thus, both model uncertainty and dissimilarity should be evaluated. In order to quantify the dissimilarity  $d$  between consecutive models in terms of the probability of a specific geological unit occurring in a given voxel, two measures, the Jaccard and the City-block distance (Figure 2.5), are proposed to complement information entropy. However, dissimilarities between models and therefore, uncertainties, have recently also been addressed very effectively using geodiversity metrics such as formation depth and volume, curvature and neighborhood relationships together with principal component analysis (Lindsay, Jessell, et al., 2013) and through topological analysis, which quantifies geological relationships in a model Thiele, Jessell, Lindsay, Ogarko, et al., 2016; Thiele, Jessell, Lindsay, Wellmann, et al., 2016.

The set of locations for which the probability  $P_x(U)$  of belonging to a particular geological unit  $U$  is greater than a threshold value  $t$  can be defined by:

$$Q_M^t = \{x\}_{P_x(U) > t} \quad (2.7)$$

A threshold value of  $t = 0$  was applied in order to capture and consider the same sample space as in  $H_U$ . This definition is highly sensitive to outcomes of small probability and might, in some cases, be more robust using a threshold value greater than zero (e.g.  $t > 0.05$ ). The Jaccard similarity measure (Webb and Copsey, 2003) is then defined as the size of the intersection divided by the size of the union (overlap) of two sample sets ( $M_1, M_2$ ), which in our case represent the similarity in position of a geological unit  $U$  between two models:

$$s_{JAC} = \frac{|Q_{M_1}^t \cap Q_{M_2}^t|}{|Q_{M_1}^t \cup Q_{M_2}^t|} \quad (2.8)$$

Accordingly, the dissimilarity between models can be expressed by the Jaccard distance:

$$d_{JAC} = 1 - s_{JAC} \quad (2.9)$$

where  $d_{JAC} = 1$  indicates maximum dissimilarity (no match in position of a geological unit  $U$  between two models); and  $d_{JAC} = 0$  indicates complete overlap.

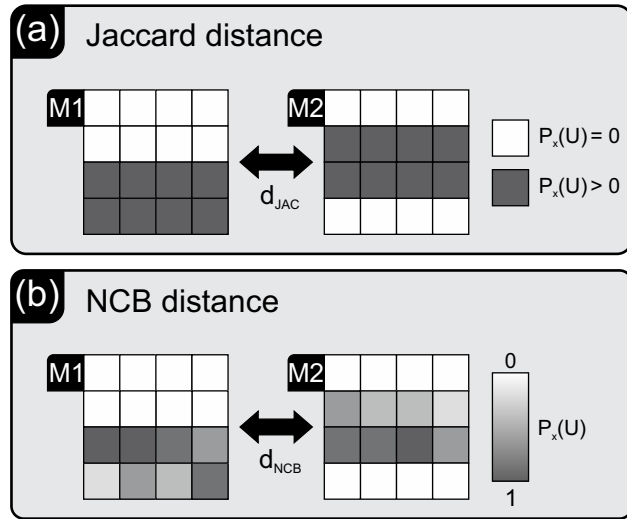


Figure 2.5: Distance measures used to calculate dissimilarities between models (M1, M2). (a) Jaccard distance ( $d_{JAC}$ ) using a TRUE/FALSE binary function and (b) Normalized City-Block distance based on a probability function.

Even though the use of binary dissimilarities is straight forward and suitable to quantify absolute changes in position of a geological unit between models, it does not account for fuzziness (c.f., section 2.3.3.2). Hence, the dissimilarity may be overestimated by the Jaccard distance. In order to include fuzziness, the normalized City-Block distance was employed, adopting the probability function  $P_x(U)$  as a dimension to compare dissimilarities between the two sample sets (M1, M2) (Paul and Maji, 2014; Webb and Copsey, 2003):

$$d_{NCB} = \frac{1}{N} \times \sum_{x=1}^N | P_x^{M1}(U) - P_x^{M2}(U) | \quad (2.10)$$

where  $N$  is the size of  $M1 \cup M2$  (i.e, number of grid cells present within the union). The distance is greatest for  $d_{NCB} = 1$ .

## 2.4 RESULTS AND DISCUSSION

### 2.4.1 Initial 3D models

The four consecutively constructed initial models show a step-wise increase in structural complexity (Figure 2.6). Model 1 was based on non-site specific geological data, and horizon orientations were only constrained by regionally available, isolated outcrop data, which made a general extrapolation of structures difficult, especially into

depth (Jessell, Ailleres, et al., 2010). Dip and strike were assumed uniform ( $40^\circ$  and  $35^\circ$ ) for all horizons across the model domain (cf., Figure 2.6). Information from geological maps and outcrop data revealed a normal fault within the AOI, which was assumed to be ENE-WSW striking with a moderate displacement of about 50 m.

In Model 2, horizon positions of the Schilfsandsteinkeuper (km2), Gipskeuper (km1) and Lettenkeuper (ku) were locally constrained by site-specific information provided by drill logs of the geothermal wells, slightly impacting fault displacement and thickness of the formations. However, changes in model geometry were minor, as no further information on horizon orientations was available and no additional faults could be located. By adding the direct problem specific data from the exploration wells to Model 3, a Horst-Graben structure was identified that entailed a considerable displacement at two normal faults between and to the north-west of the wells with a displacement of 120 m and 70 m, respectively. Furthermore, the drill logs included orientation measurements of the strata, resulting in a shift in position and inclination of layers, compared to the previous models. Thus, large parts of the model domain within the AOI changed from Model 2 to Model 3 and, as a consequence, dissimilarities between these models are particularly high (cf., section. 2.4.4). Finally, Model 4, which included data from a seismic campaign, has the highest degree of structural complexity. The information provided by seismic sections revealed uncertainties, which were present previously but not captured by the more simple models 1 to 3. Ultimately, seismic data forces the interpreter to add complexity down to a certain scale. However, seismic surveys are inherently ambiguous and allow alternative interpretations, especially concerning the orientation and number of faults as well as the type of fault contact to a fault network (e.g., branching) (Cherpeau and Caumon, 2015; Julio et al., 2015; Røe et al., 2014). In our case, seismic sections and interpretations were adopted from LGRB (2010). The indirect problem specific data from the seismic 2D survey located several additional faults within the AOI, and in some cases caused a shift in position of faults compared to Model 3. The AOI was strongly fragmented by the added faults, and the orientation of layers is no longer uniform but varies strongly between fault blocks. In summary, the step-wise integration of data according to the four data categories improved our general knowledge of subsurface structures at the study site (Figure 2.2). In addition, the effect of data integration from different exploration stages on modeled subsurface geometry could be evaluated and visualized.

#### 2.4.2 Multiple model realizations

The multiple (30) model realizations created by the Structural Uncertainty workflow of SKUA are illustrated in Figure 2.7 using 2D

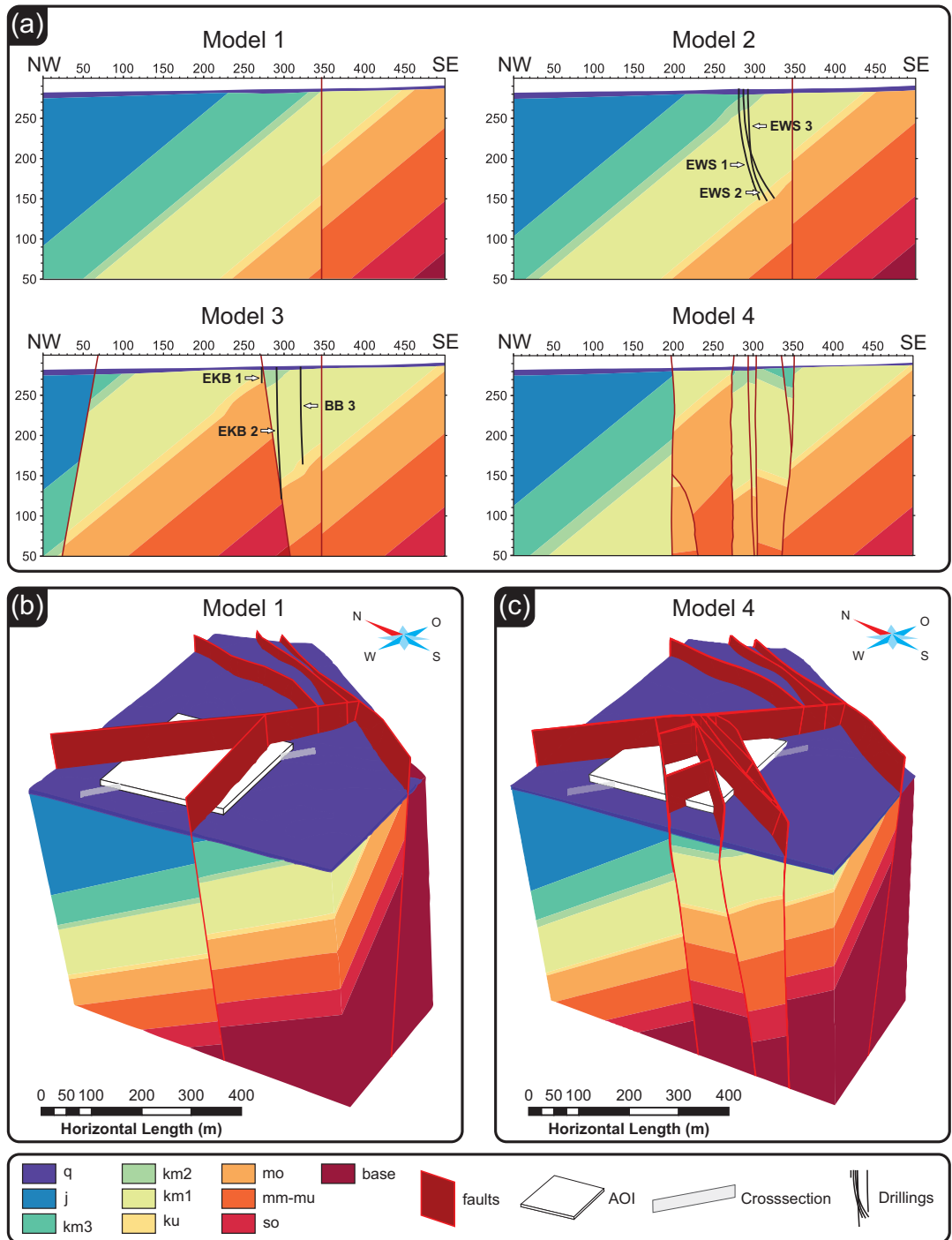


Figure 2.6: (a) Cross-section through the AOI of all four initial geological models with projected borehole tracks (black lines) and 3D representations of (b) Model 1 and (c) Model 4.

cross-sections of Model 1 and 4 as examples. A total number of 30 realizations and a cell size of 5 m was chosen as a compromise between model detail, lowest practical limit for statistical viability and data handling. For the same reason we did not base our number of realizations on an estimate of convergence. Instead we used the estimate of 30 realizations for a stable fluctuation in fuzzy entropy in a model developed by Wellmann, Horowitz, et al. (2010) as a guideline value to our model. Perturbations in horizon location are based on: 1) alternative surface interpretations, which reflect a maximum deviation in dip and azimuth ( $\pm 5^\circ$ ) from the initial surface and 2) constant displacement values, which were assigned in order to account for uncertainties in formation thickness and boundary location. For a more detailed explanation of our choice of parameters, assigned probability distributions and specific input modes of the Structural Uncertainty workflow, please refer to the supplementary material (Table S1 and S2). In Model 1, the non-site specific data set includes minimal constraints, resulting in faults and horizons of the realizations that are widely dispersed but parallel. In contrast, the faults and horizons of the Model 4 realizations are more narrowly dispersed where problem-specific data was available within the AOI. The workflow handles equal uncertainties consistently across models by producing a similar pattern of horizontal displacement in Model 1 and Model 4. This can be seen in particular for structures located close to the NW boundary, which were not further constrained by consecutively added geological data. However, it is also apparent from the mostly uniform orientation of the surfaces in the 30 realizations of each model that perturbation measures implemented in the Structural Uncertainty workflow did not allow for large variations in dip and azimuth of horizons or faults. Therefore, uncertainty may be systematically underestimated especially at greater depths.

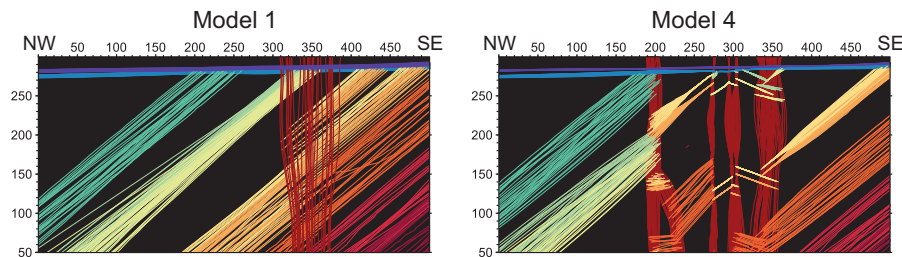


Figure 2.7: Cross-section through Model 1 and Model 4. The multiple lines show 30 model realizations with shifted faults and horizons (for the location of the cross-sections see Figure 2.6). The horizontal lines indicate the land surface (purple) and the base of the Quaternary (blue).

### 2.4.3 *Uncertainty assessment*

#### 2.4.3.1 *Distribution of information entropy*

Information entropy, quantified at the level of individual grid cells, can be visualized in 3D to identify areas of uncertainty and evaluate changes in geometry resulting from successive data integration. Figure 2.8a shows the distribution of information entropy for Models 1 and 4. It can also be seen that the approach is suitable for locating areas with high degrees of uncertainty, indicated by dark red colors (hot-spots) in this figure. Furthermore, Figure 2.8b highlights where additional constraints from the data helped to optimize the model by reducing uncertainties ( $\Delta H_x < 0$ ) and whether further constraints are needed in locations of specific interest.

The overall distribution of uncertainty was clearly affected by additional geological information from site and problem specific input data (Model 4). This effect is highlighted by the changes in entropy between the models (Figure 2.8b). Additional constraints on horizon and fault boundaries caused a shift in position and orientation of geological units, followed by a large redistribution of uncertainties, indicated by the changes in entropy. It can be seen that new hot-spots of uncertainty were introduced in proximity to the faults identified by the exploration boreholes and the seismic data incorporated into Model 4 (c.f., Figure 2.6). However, these new areas of uncertainty can be considered an optimization of the model, because large parts of the preceding Model 1 did not reflect the complex local geology. Model 1 (wrongly) predicted low uncertainties for areas where information on unidentified but existing structures (i.e. faults) was missing. This illustrates that epistemic uncertainties at the study site are likely substantial. Even Model 4 will inevitably still under-represent the true structural complexity at this site, especially in areas of low data density. In a risk-assessment and decision-making process, this can be problematic, because low uncertainty areas might be in fact no-information areas. In such a case, the respective model area would actually be highly uncertain. However, ambiguities in data interpretation (e.g. seismic sections) can lead to incorrectly identified structures and uncertainty in any case, even in areas of high data density. Nevertheless, the approach allows one to assess and visualize uncertainties related to structures that have been identified during site investigation. To lessen the limitations posed by non-sampled locations, Yamamoto et al. (2014) proposed a post-processing method for uncertainty reduction, using multiple indicator functions and interpolation variance in addition to information entropy. Based on information theory, Wellmann (2013) further proposed joint entropy, conditional entropy and mutual information as measures to evaluate correlations and reductions of uncertainty in a spatial context. However, uncertainty from lack of evidence for a geological structure (e.g. fault),

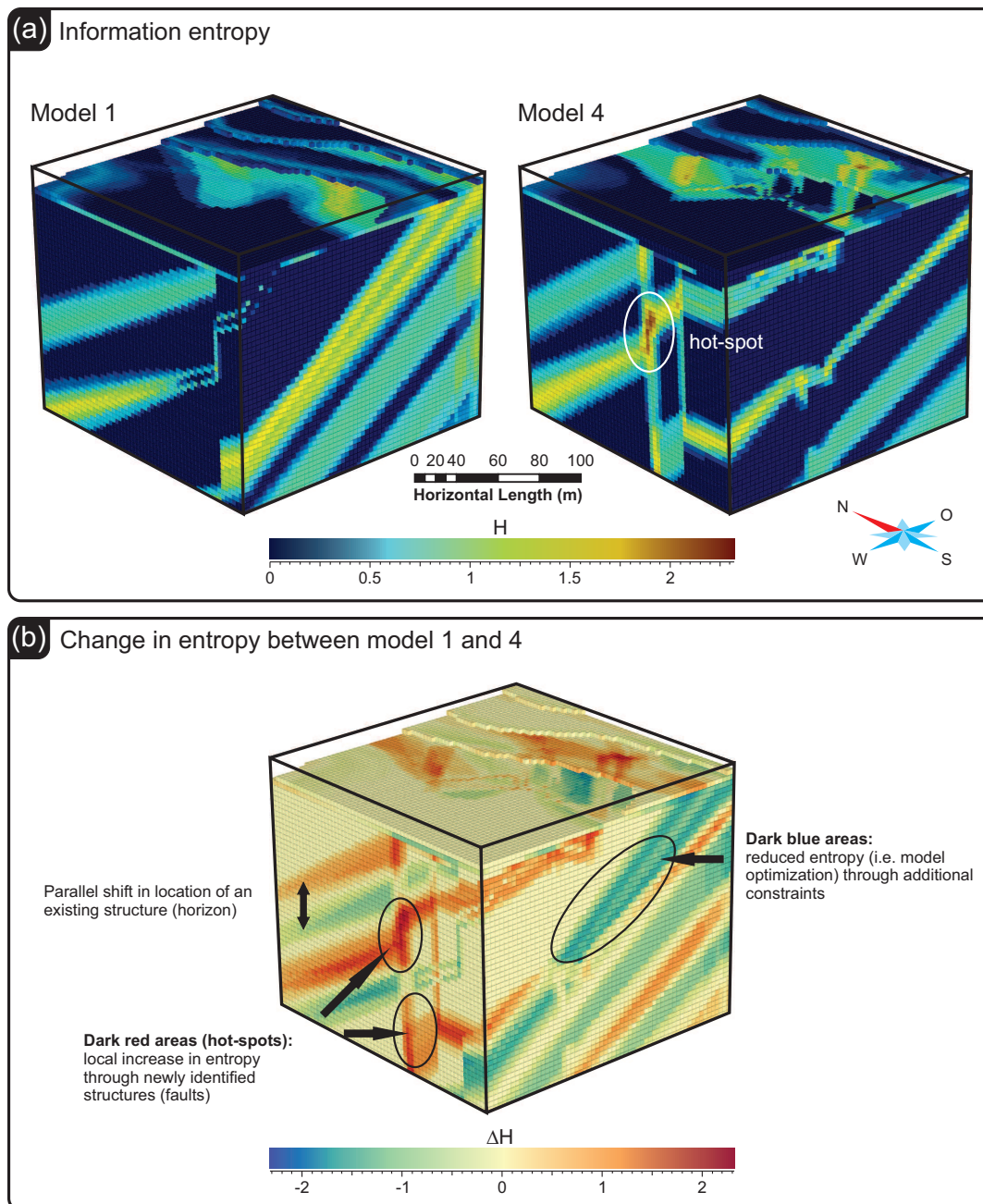


Figure 2.8: 3D view of the AOI with a discretization of 5 m for (a) average information entropy  $H_M$  of Model 1 and Model 4 and (b) change in entropy  $\Delta H_x$  between both models.

known as imprecise knowledge (Mann, 1993), still depends on the density and completeness of available input data.

#### 2.4.3.2 *Average information entropy*

The calculated average information entropy  $H_T$  of the consecutive models steadily decreases with higher data specificity (i.e. non-site to problem specific, see Figure 2.2) from Model 1–4 (Figure 2.9). Mean values of  $H_M$  ranged from 0.56 (Model 1) to 0.39 (Model 4), where  $H_M = 0$  would denote no structural uncertainty. The decrease from Model 1 to 4 is approximately linear, indicating that all four categories of geological data had a similar impact on overall model uncertainty, even though the added information resulted in quite different model geometries and, as discussed above, in some cases in a local increase in entropy (cf., Figure 2.8b). A similar but more pronounced trend was observed for the average entropy  $H_S$  of the subsets  $S_{km1}$ ,  $S_{ku}$  and  $S_{mo}$ , which represent the domain of the three geological units that are of particular importance to the swelling problem. However, entropy, i.e. the amount of uncertainty, is considerably higher within the domain of these geological units than for the overall model space, especially for the subsets  $S_{ku}$  and  $S_{mo}$ , identifying them as areas of a particularly high degree of uncertainty. Note that these units are the aquifers that have been hydraulically connected to the swellable rocks via the geothermal drillings. Nevertheless, all entropy values are comparably moderate, considering that a maximum of (only) five different geological units was found in any one grid cell across all four models, yielding a possible maximum entropy of  $H_M = 2.32$  for an equal probability distribution ( $P_1 = P_2 = P_3 = P_4 = P_5$ ). For comparison: if all ten geological units would be equally probable, the maximum entropy would be 3.32. Furthermore, median values and interquartile range dropped from 0.51 (0 to 0.99) in Model 1 to 0.0 (0 to 0.84) in Model 4. This helps to illustrate that the amount of grid cells with  $H_x = 0$  (indicating no inherent uncertainty), increased notably by 34.8% from 40.6% (Model 1) to 54.8% (Model 4); and that the remaining entropies in Model 4 are limited to a considerably smaller number of cells within the model domain.

Overall, comparing the pre- to post-site-investigation situations (Model 1 to 4), site and problem specific investigations were all equally successful in adding information to the model and reducing uncertainties in the area of the targeted horizons. While the benefits from the different data are equal, the costs in data acquisition (i.e. work, money and time required) may vary considerably, depending on the exploration method (e.g., drillings, seismic survey, etc.). An economic evaluation was not within the scope of this study. Nevertheless, the approach presented could improve cost and benefit analyses by quantifying the gain in information through different exploration stages.

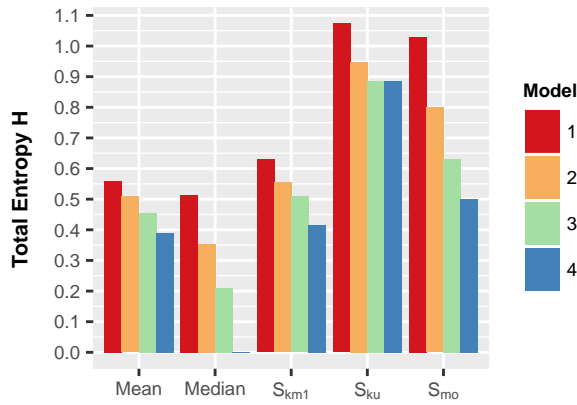


Figure 2.9: Average entropy  $H_M$  calculated for the different models (mean and median) and for subsets of the model space of each model ( $S_{km1}$ ,  $S_{ku}$ ,  $S_{mo}$ ).

### 2.4.3.3 Fuzzy set entropy

The fuzzy set entropy was calculated to indicate how well-defined a geological unit is within the model space. Applied to the swelling problem of our case study, a high degree of uncertainty remains with regard to the position of the relevant geological units ( $km1$ ,  $ku$ ,  $mo$ ) after full data integration. We obtained fuzzy set entropy values ( $H_U$ ) ranging between 0.329 to 0.504 (Figure 2.10). The fuzziness of these geological units only slightly changed from Model 1 to Model 4, indicating that higher data specificity did not translate into more clearly defined geological units within the model domain. This can be partially attributed to the complex geological setting of the study site. In the process of data integration, additional boundaries between geological units are created at newly introduced faults, increasing the overall fuzziness of a unit.

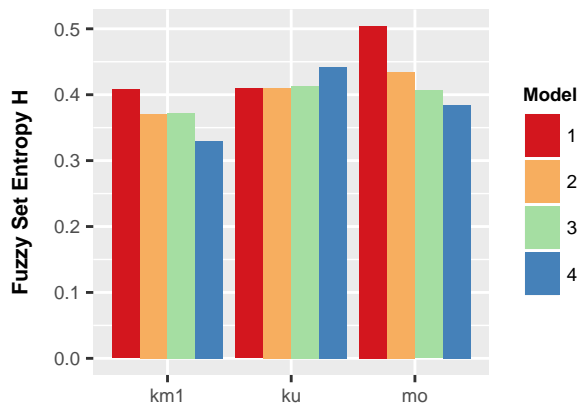


Figure 2.10: Fuzzy set entropy  $H_U$  of the targeted geological units  $km1$ ,  $ku$  and  $mo$  of the different models.

In case of the Lettenkeuper formation (unit ku), boundaries are even slightly less well-defined in Model 4 compared to Model 1. This is likely related to the low thickness of the formation (5 to 10 m, Figure 2.3) relative to the mesh size (5 m). A finer grid could reduce this effect; however computation time would increase significantly. Wellmann and Regenauer-Lieb (2012) propose using unit fuzziness to determine an optimal representative cell size and reduce the impact of spatial discretization on information entropy. As previously discussed in section 2.4.2, our workflow does not explicitly consider uncertainties through dip and strike variations by a value indicated for this purpose, but through perturbations based on alternative surface interpretations, which in our case likely underestimates the fuzziness of the targeted geological units at greater depths. Thus, overall fuzziness, particularly in Model 1, may be significantly higher than calculated.

#### 2.4.4 Models dissimilarity

A gain in structural information through newly acquired data usually not only impacts model uncertainty but is also associated with a change in model geometry. The calculated distances between models can identify the data category with the strongest impact on model geometry and make it possible to determine whether model geometry and uncertainty are related. Figure 2.11 shows the calculated Jaccard and City-Block distances between the models with respect to the targeted geological units km1, ku and mo.

Calculated distances between models are rather high, with values of up to 0.78; indicating a pronounced shift in position of the geological units after data was added. The addition of both direct and indirect problem specific data to Model 3 had a strong impact on model geometry, which can be seen by comparing the calculated distances between Model 2, 3 and 4 for both, Jaccard and City-Block (Figure 2.11). In contrast, site specific data had a much lower effect, with less than 20% (0.2) change in unit position, except for ku of the Jaccard distance (see distance between Model 1 and 2).

Overall, the City-Block distance, which considers the fuzziness of geological boundaries, shows a similar trend as the Jaccard distance; however changes are much less pronounced, especially for unit ku. According to the low City-Block distance, absolute changes in probability  $P_x(U)$  for each grid cell are small, whereas high Jaccard distances indicate a large number of grid cells being affected through newly added data. Thus, the Jaccard distance likely overestimated the actual dissimilarity between models. Comparing unit ku of both distances; the disparity between values hints at a large number of low degree changes in membership of the grid cells ( $\Delta P_x(U) \ll 1$ ). These predominately low degree changes are likely related to the above

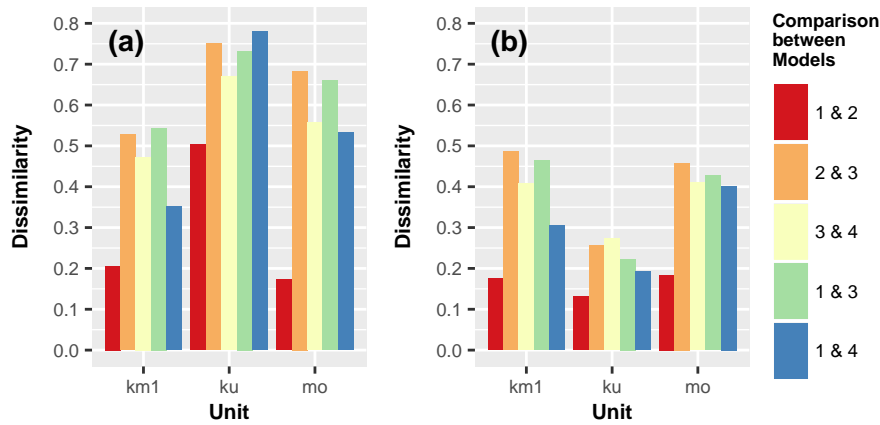


Figure 2.11: Dissimilarities between the different models expressed by (a) Jaccard distance, and (b) City-Block distance.

mentioned high degree of unit boundary fuzziness; and the resulting, ill defined, geological unit ku being shifted within the model domain. However, a direct comparison of fuzzy set entropy to the corresponding City-Block distance yields no quantifiable relationship between model geometry and structural uncertainty.

Nonetheless, both distance measures allow quantification and assessment of different aspects of dissimilarities and therefore, changes in geometry across models. Yet, the City-Block distance is preferable when sets of multiple realizations are compared, because it factors in the probability of occurrence of a geological unit at a discrete location. In recent years, various distance measures have already been applied in other contexts to create dissimilarity distance matrices and compare model realizations in history matching and uncertainty analysis, particularly in reservoir modeling (Park et al., 2013; Scheidt and Caers, 2009a,b; Suzuki et al., 2008). These include the Hausdorff distance which, similar to our approach, directly compares the geometry of different structural model realizations, but also more sophisticated measures that calculate distances in realizations based on flow model responses from a transfer function.

## 2.5 SUMMARY AND CONCLUSIONS

Prior work has demonstrated the effectiveness of information entropy in assessing model uncertainties and providing valuable insight into the geological information used to constrain a 3D model. Wellmann and Regenauer-Lieb (2012), for example, evaluated how additional information reduces uncertainty and helps to constrain and optimize a geological model using the measure of information entropy. Their approach focused on a hypothetical scenario of newly added borehole data and cross-section information to a synthetic model. In the

present study, information entropy and, in addition, model dissimilarity was used to assess the impact of newly acquired data on model uncertainties using actual site investigation data in the complex geological setting of a real case.

We presented a new workflow and methods to describe the effect of data integration on model quality, overall structural understanding of the subsurface and model geometry. Our results provide a better understanding of how model quality can be assessed in terms of uncertainties in a data acquisition process of an exploration campaign, showing that information entropy and model dissimilarity are powerful tools to visualize and quantify uncertainties, even in complex geological settings. The main conclusions of this study are:

- (1) Average and fuzzy set entropy can be used to evaluate uncertainties in 3D geological modeling and, therefore, support model improvement during a consecutive data integration process. We suggest that the approach could be used to also perform a cost-benefit analysis of exploration campaigns.
- (2) The study confirms that 3D visualization of information entropy can reveal hot-spots and changes in distribution of uncertainty through newly added data in real cases. The method provides insight into how additional data reduce uncertainties in some areas, and how newly identified geological structures may create hot-spots of uncertainty in others. Furthermore, the method stresses that parsimonious models can locally under-estimate uncertainty, which is only revealed after new data is available and being considered.
- (3) Dissimilarities in model geometry across different sets of model realizations can effectively be quantified and evaluated by a single value using the City-Block distance. A combination of the concepts of information entropy and model dissimilarity improves uncertainty assessment in 3D geological modeling.

However, some limitations of the presented approach are noteworthy. Although it was designed to assess uncertainties in the position and thickness of horizons, uncertainty in orientation could only be included indirectly through perturbations based on alternative surface interpretations, but not by explicit dip and azimuth parameter values indicated for this purpose. This may result in a systematic underestimation of uncertainties at greater depths of the model domain. Furthermore, our study site (Vorbergzone) is a highly fragmented geological entity, and epistemic uncertainties due to missing information about unidentified but existing geological structures are likely substantial.

Future work should therefore aim to include “fault block uncertainties” more effectively into the workflow, for example by including multiple fault network interpretations (Cherpeau and Caumon,

2015; Cherpeau, Caumon, and Lévy, 2010; Holden et al., 2003) or by considering fault zones that produce a given displacement by a variable number of faults. Finally, all data of the investigated site was collected prior to our analysis; therefore additional data was not explicitly collected in order to reduce detected uncertainties within the consecutive models. Applying this approach during an ongoing site investigation could improve the targeted exploration and allow a well-founded cost-benefit analysis through uncertainty hot-spot detection.

## 2.6 ACKNOWLEDGMENTS

The financial support for D. Schweizer from the German Research Foundation (DFG) under grant number BU 2993/2-1 is gratefully acknowledged. We acknowledge support by Deutsche Forschungsgemeinschaft and Open Access Publishing Fund of Karlsruhe Institute of Technology. Furthermore, we thank the Geological Survey of Baden-Wuerttemberg (LGRB), especially Gunther Wirsing and Clemens Ruch (LGRB) for data provision; and the Paradigm support team for their technical support. Finally, we would like to thank Jan Behrmann (GEOMAR) and Thomas Bohlen (KIT) for discussions of the tectonic setting and seismic interpretations, respectively.



### Part III

## REACTIVE TRANSPORT MODELING OF SWELLING PROCESSES IN CLAY-SULFATE ROCKS

This study is published in the AGU journal *Water Resources Research*. Part III is a reprint of:

Schweizer, D., Prommer, H., Blum, P., Siade, A. J., & Butscher, C. (2018). Reactive Transport Modeling of Swelling Processes in Clay-sulfate Rocks. *Water Resour. Res.* 54(9), 6543–6565. doi:[10.1029/2018WR023579](https://doi.org/10.1029/2018WR023579)



## PART 3: A CONCEPTUAL REACTIVE TRANSPORT MODEL

---

### ABSTRACT

Swelling of clay-sulfate rocks often causes large problems in geotechnical applications such as tunneling. The primary mechanism inducing the increase in rock volume is the chemical transformation of anhydrite to gypsum, which is triggered by the ingress of groundwater. In the present study, a novel conceptual and numerical modeling approach is developed that emphasizes the effect of groundwater flow in conjunction with the associated availability of water and changing geochemical conditions on the chemical transformation of anhydrite to gypsum. A reactive transport model was developed and hydraulic, reactive and solute transport as well as mechanical model parameters were estimated through an inversion process, constrained by geodetic ground heave measurements from a study site in Staufen, Germany. The conceptual model of the swelling process was implemented numerically through a dual-domain modeling approach, whereby the mobile domain accounts for solute transport along discontinuities, and the immobile “reactive domain” represents the matrix. A mass transfer process accounts for diffusive and/or capillary water transport into the matrix, where the rate-limited transformation of anhydrite to gypsum takes place. The model calculates heave at the land surface depending on water inflow, the transformation of anhydrite into gypsum and the local stress conditions exerted by overburden pressure. The results show that the proposed reactive transport modeling approach is suitable to quantify the observed swelling-induced heave at the study site with a plausible parameterization. The study also highlights that diffusion is a decisive factor for the effective rate of anhydrite dissolution and, therefore, the overall chemical transformation process.

### 3.1 INTRODUCTION

Understanding the hydro-mechanical-chemical processes associated with rock swelling plays an important role for mitigating and preventing the failure of many geotechnical applications. For example, the swelling of argillaceous rock through hydration and osmosis is a decisive factor in selecting geologic formations suitable for hosting rock nuclear waste storage facilities (e.g., NDA, 2010) and in determining the stability of well drillings in shales (Fjar et al., 1993).

Rock swelling is particularly pronounced in clay-sulfate rocks, such as those found in the Triassic Gypsum Keuper formation in southern Germany. The most severe problems with swelling clay-sulfate rocks are typically encountered during the construction of tunnels, and more recently also in conjunction with vertical ground source heat pump (GSHP) systems (Fleuchaus and Blum, 2017; Grimm et al., 2014). Clay-sulfate rocks may swell substantially upon contact with water, thus creating pressures that can severely damage infrastructure through the heaving of tunnel sections and the ground surface (Anagnostou, Pimentel, et al., 2010; Ruch and Wirsing, 2013). Although it is generally accepted that rock swelling is triggered by inflow of water stemming from engineering activities, the processes underlying the actual swelling of clay-sulfate rocks are not yet sufficiently well understood (Butscher, Breuer, et al., 2018; Butscher, Mutschler, et al., 2016). In particular, the link between hydrogeological and geochemical processes and their resulting response on geomechanical swelling requires further investigation in order to develop effective countermeasures to mitigate or even prevent swelling. This is especially true in settings where the swelling cannot be contained via engineering solutions (Kovári and Chiaverio, 2007; Pierau and Kiehl, 1996).

Clay-sulfate rocks consist of a clay matrix that contains finely dispersed anhydrite crystals or anhydrite layers and nodules of varying dimensions, with the actual texture of the rock depending on its pressure and temperature history (e.g., Rauh and Thuro, 2007). In general, clay-sulfate swelling involves two partially superimposed processes: (1) The swelling of clay minerals through osmotic water uptake and hydration (Madsen and Müller-Vonmoos, 1989), and (2) the swelling of sulfates caused by the chemical transformation of anhydrite ( $\text{CaSO}_4$ ) into gypsum ( $\text{CaSO}_4 \cdot \text{H}_2\text{O}$ ) upon contact with water ( $\text{CaSO}_4 + 2\text{H}_2\text{O} \longleftrightarrow \text{CaSO}_4 \cdot \text{H}_2\text{O}$ ). The latter process results in a volume increase of up to 61 % and is considered to be the main mechanism of swelling in clay-sulfate rocks. The swelling potential, however, is strongly dependent on the specific surface area of the anhydrite crystals and thus on the grain morphology. Finely dispersed anhydrite crystals are particularly prone to swelling due to their relatively large surface area in potential contact with water. Beds of massive anhydrite, in contrast, show relatively little swelling (Rauh and Thuro, 2007). Furthermore, Madsen and Nuesch (1991) showed that the swelling potential of clay-sulfate rocks also depends on the clay content and reaches its maximum at about 15 % clay. There are numerous conflicting hypotheses for this causal link and the role of clay in clay-sulfate swelling (See Butscher, Mutschler, et al. (2016), for an overview). They range from an increase in water availability for anhydrite through flow paths created by rock disintegration or locally increased permeability, to an influence on the sulfate concentration and thus the anhydrite saturation state, all triggered by the swelling

of clay. Expansive clay minerals such as corrensite also appear to play an important, yet not clearly defined, role in the swelling. Possibly they facilitate the transformation of anhydrite into gypsum (Anagnostou, Pimentel, et al., 2010; Lippmann, 1976; Wittke, 2014).

The mineralogical transformation of anhydrite into gypsum takes place indirectly via the solution phase, with anhydrite dissolving into the pore water and gypsum subsequently precipitating from the solution. Dissolution and precipitation equilibria are controlled by the pore water composition, temperature, and pressure (Serafeimidis and Anagnostou, 2014a,b). Reaction kinetics additionally depend on the available reactive mineral surfaces (Hardie, 1967; Hill, 1937; Serafeimidis and Anagnostou, 2012b). Furthermore, the reaction kinetics depend on the hydrodynamic conditions of the system (Jeschke, Vosbeck, et al., 2001), which may drastically change during swelling, for example, because the hydraulic properties of discontinuities are altered by gypsum crystallization (Alonso, 2012; Wittke, 2014). Hydrodynamic conditions are also altered by engineering activities, on both the regional and local scale (e.g., Butscher, Einstein, et al., 2011; Scheidler et al., 2017), therefore affecting solute transport and water accessibility within the clay-sulfate rocks. Thus, in order to gain a comprehensive understanding of the swelling phenomena, knowledge of the controlling hydrogeological and geochemical conditions and processes, and how these are affected by engineering activities (e.g., geothermal drillings), is of paramount importance.

Previous studies have provided important insights into the geochemical processes affecting the  $\text{CaSO}_4 - \text{H}_2\text{O}$  system, for example by determining stability fields of anhydrite and gypsum under various pressure, temperature and concentration conditions (e.g., Blount and Dickson, 1973; Dai et al., 2017; Freyer and Voigt, 2003; MacDonald, 1953; Marsal, 1952; Partridge and A. H. White, 1929), which can be used to characterize the critical conditions that may lead to sulfate dissolution or precipitation. Under low pressure and temperature conditions, which normally prevail in Gypsum Keuper formations relevant to geothermal applications and tunneling, the solubility of anhydrite is higher than that of gypsum. Under these conditions, the inflow of water (e.g., triggered by geothermal drilling) induces the chemical transformation of anhydrite to the stable mineral phase gypsum, which continues until all anhydrite has been consumed. This kinetically controlled process continues to occur as a result of the system being in a continuous state of under-saturation with respect to anhydrite, which is maintained by a decrease in calcium and sulfate ion concentration in solution through gypsum precipitation. J. Christoffersen and M. R. Christoffersen (1976), Jeschke and Dreybrodt (2002), Jeschke, Vosbeck, et al. (2001), Kontrec et al. (2002), Serafeimidis and Anagnostou (2012a), and Zorn et al. (2009) and others have investigated the kinetics of anhydrite dissolution and gypsum precipitation

of such systems. Their studies were able to provide estimates of reaction rate constants and insights into the evolution of the transformation process under the respective governing laboratory conditions.

Earlier studies focused mainly on the formation of natural mineral deposits and applications in the building industry, i.e., for gypsum targeting and mining. More recent work, however, has investigated the reaction kinetics as well as the critical geochemical conditions (Anagnostou, Serafeimidis, et al., 2014; Serafeimidis and Anagnostou, 2013), including the effect of regional groundwater flow and hydrological boundary conditions, that impact the swelling of clay-sulfate rocks (Butscher, Huggenberger, and Zechner, 2011; Butscher, Huggenberger, Zechner, and Einstein, 2011). Furthermore, several numerical models have been proposed, including models that couple hydrological, chemical and mechanical processes, to simulate the swelling of such rocks. Anagnostou (1992, 1993), for example, developed the first hydro-mechanical model that considers the effect of seepage flow on deformation patterns around tunnels in swelling rocks. Alonso and Olivella (2008) and Ramon and Alonso (2013) implemented gypsum crystal growth as the driving swelling mechanism in a chemo-mechanical model, which was further refined and implemented as a cross-sectional hydro-chemo-mechanical model by Ramon, Alonso, and Olivella (2017), describing the deformation processes occurring in the Lilla tunnel, located in the province of Tarragona, Spain. Oldecop and Alonso (2012) also developed a one-dimensional hydro-chemo-mechanical model for the same incident, confirming anhydrite dissolution and gypsum precipitation as the most likely mechanism of swelling. Although these studies and models consider hydro-mechanical and chemical processes as well as their coupling, the consideration of actual hydrogeological and geochemical conditions at the field scale as well as the impact of groundwater influx on changes in geochemical conditions need further and more detailed investigations.

In the present study, a novel conceptual and numerical modeling approach is developed that emphasizes the effect of groundwater flow, in conjunction with the associated availability of water and changing geochemical conditions, on the chemical transformation of anhydrite to gypsum. A reactive transport modeling approach is employed to simulate the coupled flow, transport and reaction processes and to underpin the quantification of the swelling process. It is hypothesized that the interplay between the various simulated physical and chemical processes has a significant influence on the extent and progression of swelling in clay-sulfate rocks and for the ensuing deformation. Actual groundwater compositions, saturation states and speciation of all major water constituents, and the effect of foreign ions in solution on the solubility of anhydrite and gypsum, are considered. Moreover, in order to adequately account for the flow

and transport characteristics of fractured argillaceous rocks, a dual-domain mass transfer approach (DDMT) was employed. The mobile domain accounts for solute transport within fractures and discontinuities, while the majority of the aquifer, i.e., the matrix, is considered immobile. The two domains are connected through a concentration - dependent mass transfer process to represent the diffusive and/or capillary water transport into the matrix, where the potentially rate-limited transformation of anhydrite to gypsum takes place. Finally, the modeling approach decouples the transformation of anhydrite to gypsum from the water present in the rock prior to swelling. Instead, water intruding from outside the system is effectively used as a catalyst of the reaction. Hence, water inflow and resulting geochemical reactions can be simulated in anhydrite bearing clay-rocks assuming saturated conditions. While this conceptual approach does not necessarily reflect the actual processes taking place at the pore scale, it is well suited to describe the swelling of clay-sulfate rocks triggered and controlled by water inflow at the field scale.

Heave at the ground surface is calculated from volume changes due to anhydrite-gypsum transformation in the swelling zone, considering the geomechanical dependency of swelling on the prevailing stress conditions (overburden). Data collected at a geothermal drilling site in Germany is used to guide the development and parameterization of a modeling framework that quantifies the spatio-temporal heave patterns. The model determines and illustrates the influence of hydro(geo)logical, geochemical and geomechanical processes on the change in rock volume, associated deformation and subsequent heave at the ground surface at the field scale.

## 3.2 STUDY SITE

### 3.2.1 Overview

In 2007, a drilling campaign with boreholes of a depth of up to 140 m was undertaken in the city of Staufen (South-West Germany) to install seven borehole heat exchangers (BHE) (Figure 3.1). Shortly after completion, a dramatic heave of the ground occurred with uplift rates reaching up to  $11 \text{ mm month}^{-1}$  (LGRB, 2010) and a total uplift of up to 60 cm between 2007 and 2018. More than 250 houses were seriously damaged with costs exceeding 50 Mio. € (Fleuchaus and Blum, 2017). Extensive investigations of the cause of the heave showed that an incomplete annular sealing in one or more of the BHE drillings created a hydraulic short-circuit between the anhydrite-bearing clay rocks of the Gypsum Keuper formation and deeper artesian aquifers (Fleuchaus and Blum, 2017; Grimm et al., 2014; LGRB, 2010; Ruch and Wirsing, 2013; Sass and Burbaum, 2010). It was hypothesized that fractures, or high conductivity preferential flow paths

(PFPs) within the expansive layers facilitated the lateral transport of inflowing water, which triggered the chemical transformation of anhydrite to gypsum, followed by a net increase in rock volume that ultimately caused the observed ground heave.

In 2009, mitigation measures were initiated. They included grouting of the BHE and the installation of pumping wells in the deeper aquifers (i.e. in the Lettenkeuper and Upper Muschelkalk formation) to suppress water inflow into the anhydrite bearing rocks by lowering the hydraulic potential below the level of the swelling zone (Ruch and Wirsing, 2013). The mitigation measures were successful in decreasing the heave rates at the surface. However, until today it has been impossible to completely prevent further swelling. A potential explanation for this is that even if the remediation measures were successful in preventing further water inflow into the swelling zone, the heave at the ground surface will continue until all water in the swelling zone is consumed by anhydrite to gypsum transformation. Currently, there is no technical solution to extract water that has already intruded into the swelling layers.

### 3.2.2 *Geology and hydrogeology*

Staufen is located at the eastern margin of the Upper Rhine Graben within the so called “Vorbergzone” of the southern Black Forest, which is characterized by high structural complexity and strong fragmentation of the geological strata (Genser, 1959; LUBW, 2005). Three geological formations relevant to the swelling problem can be distinguished: (1) The Triassic Gypsum Keuper formation (km1) containing the swelling zone, followed below by (2) the Lettenkeuper (ku) and (3) the Upper Muschelkalk (mo) formations, with (2) and (3) representing the two main aquifers in the studied system (Figure 3.2).

The Gypsum Keuper is composed of calcium-sulfate rocks, marls and mudstone with an average thickness of 100 to 110 m. This formation can be divided into three zones of different geotechnical and hydrological properties according to the degree of leaching and the prevailing type of sulfate (LGRB, 2010; Wittke, 2014) (also see Figure 3.3). In the leached Gypsum Keuper above the upper gypsum level (UGL, 28.6 m below ground level (bgl)), all sulfate has been dissolved and transported away with groundwater flow in geological times, creating a water-bearing first zone characterized by high permeability (gypsum karst). It is followed by a second zone of unleached Gypsum Keuper between the UGL and the upper anhydrite level (UAL, 61.5 m bgl) and characterized by low permeability and sulfate being present as gypsum. Below the UAL, a third zone, comprising unleached Gypsum Keuper that, with depth, increasingly consists of anhydrite-bearing claystone of generally very low permeability is located. Based on exploration borehole data (drilling EBH2 in

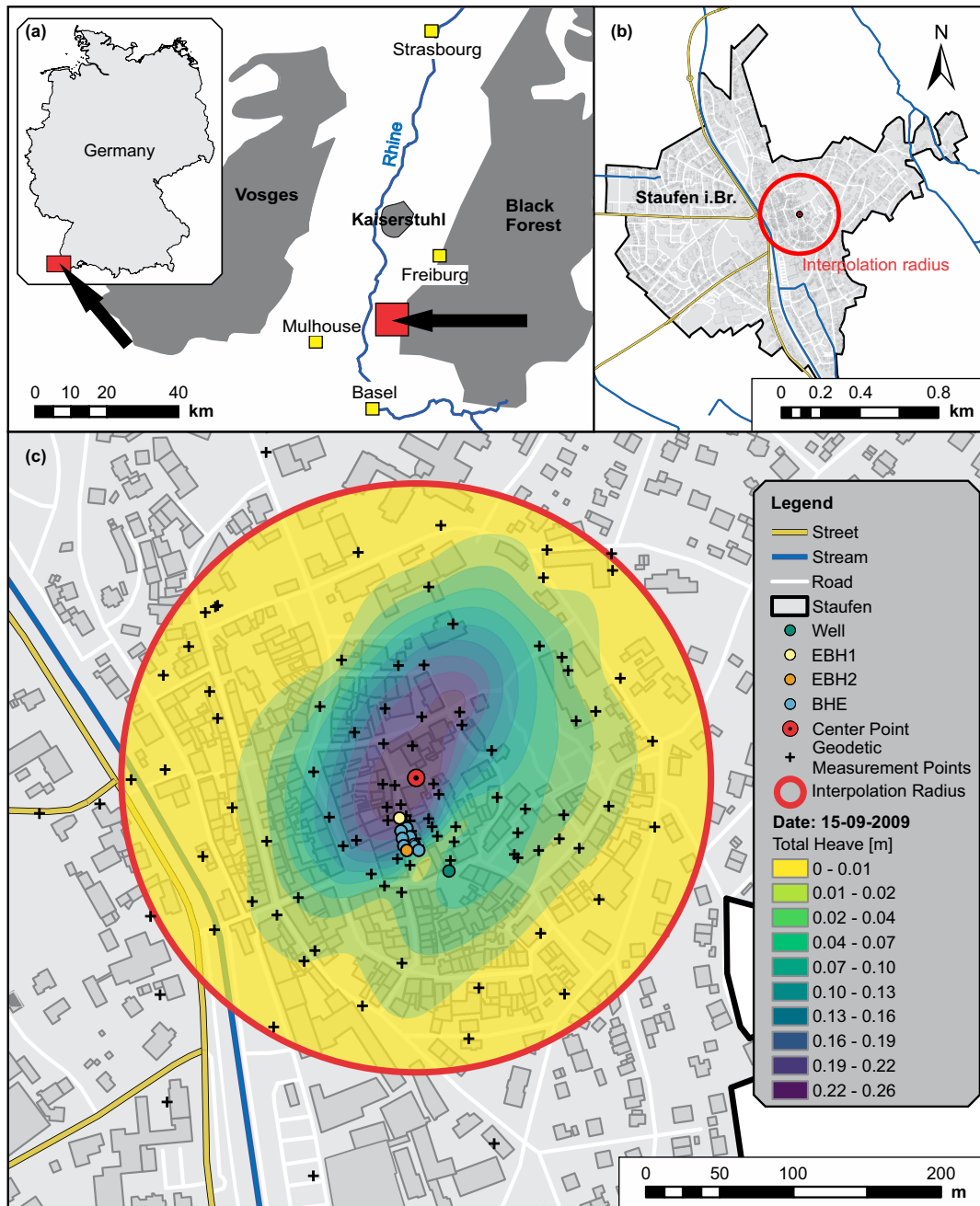


Figure 3.1: Study site with location of the interpolated uplift area in the city of Staufen, locations of borehole heat exchangers (BHE), exploration boreholes (EBH<sub>1</sub> and EBH<sub>2</sub>) and a well installed for counter measures. Total heave since installation of the BHE is depicted at the time of mitigation measure initiation.

Figure 3.1), the swelling zone is located in this section of the unleached Gypsum Keuper. Increased permeability was documented by drilling fluid losses at 76.4 m bgl pointing towards fractures or PFPs. The potential swelling zone has a thickness of approximately 42 m and is characterized by a mineralogical composition particularly susceptible to swelling, containing up to 40% (average of 13.7%) of the expansive clay mineral corrensite, present in thin alternating layers of clay, anhydrite and gypsum, and millimeter-sized anhydrite nodules dispersed within the clay matrix (LGRB, 2010). An “anhydrite core” (AC) demarks the lower boundary of the swelling zone with anhydrite and expansive clay contents being too high and too low for significant swelling to occur, respectively. Below the AC, the three identifiable zones appear in an inverted order with the lower anhydrite level (LAL) at 126 m bgl and the lower gypsum level (LGL) at 141.7 m bgl.

The Gypsum Keuper formation is underlain by the Lettenkeuper formation (143 to 155 m bgl), a fractured rock aquifer of 5 to 10 m thickness composed of alternating dolomitic limestone, mudstone and sandstone, followed by the Upper Muschelkalk formation (~60 m thickness). This formation mainly consists of karstified limestone and dolomitic limestone, constituting a regional aquifer. The groundwater of both aquifers is artesian with heads measured at 1.8 and 2.1 m above ground level (agl), respectively (Figure 3.3). All formations and groundwater systems were hydrogeologically disconnected prior to drilling, with no apparent vertical flow that would allow the rise of artesian groundwater from the deeper aquifers into the anhydrite-bearing Gypsum Keuper. The originally disconnected nature of the groundwater systems was confirmed by hydrochemical analysis (Table 3.1). A more exhaustive description of the hydrogeology, lithology and formation properties can be found in the survey report by LGRB (2010).

### 3.3 CONCEPTUAL AND NUMERICAL MODEL DEVELOPMENT

#### 3.3.1 *Conceptual approach: overview*

A reactive transport model approach was developed to simulate coupled flow, transport and chemical reactions. The model was used to quantify and analyze the underlying hydraulic and geochemical processes in the swelling zone of the study site. In a subsequent post-processing step, the mass of precipitated gypsum crystals calculated by the model was related to rock deformation as a function of the effective stress, using a bulking (swelling) coefficient proposed by Oldecop and Alonso (2012) and Ramon and Alonso (2013). This coefficient considers that gypsum crystals might either precipitate and occupy existing open spaces (no deformation), or cause a volume increase

Stratigraphy		Lithology	Thickness [m]	Lithological description	<input type="checkbox"/> Aquifer <input checked="" type="checkbox"/> Aquitard	k-values [m/s]	
Quaternary		q		Fluvial-glacial gravels and sands			
Triassic	Keuper	Upper	km2	5–40	Alternation of sandstone and siltstone	$8 \times 10^{-6}$	
			GES	10	Clay, dolomite and marls Leached gypsum residuuls	Gypsum karst	
		UBE	15				
	Middle	km1	MGH	40	Unleached Alternation of clay, nodular and bedded gypsum/anhydrite		
			WEH	10			
			DRM	15			
			BH	10			
			GI	25		Alternation of dolomite and gypsum Leached gypsum residuuls	
	Lower	ku	LK	5–10	Dolomite and shales	Lettenkeuper aquifer	$5 \times 10^{-6}$
	Muschelkalk	Upper	moR	20–55	Dolomite		$4 \times 10^{-7}$
		mo	25–40	Limestone, bedded	Upper Muschelkalk aquifer		

Figure 3.2: Overview of the stratigraphy, lithology and hydraulic properties at the study site based on LGRB (2010) and the German stratigraphic nomenclature of the Triassic by Nitsch et al. (2005). GES = Graue Estherien-Schichten, UBE = Untere Bunte Estherien-Schichten, MGH = Mittlerer Gipshorizont, WEH = Weinsberg-Horizont, DRM = Dunkelrote Mergel, BH = Bochingen-Horizont, GI = Grundgipsschichten, LK = Lettenkeuper, moR = Rottweil-Formation, UGL = Upper Gypsum Level, UAL = Upper Anhydrite Level, AC = Anhydrite Core, LAL = Lower Anhydrite Level, LGL = Lower Gypsum Level.

by enlarging or opening up new voids. In a final step, the calculated volume change in the swelling zone was projected to the ground surface as heave. For simplicity, neither the orientation of the geological layers nor elastic deformation of the overburden were considered. To constrain the model, calculated ground heave was compared to field data from a geodetic monitoring network at the study site (LGRB, 2010). A similar approach using monitoring data for model calibration was described by Ramon and Alonso (2013) and Ramon, Alonso, and Olivella (2017) using vertical displacement data of a bridge pillar and tunnel in Spain, respectively. The location of maximum uplift at the ground surface (i.e., center of heave cone) and of the water intrusion in the subsurface (at the BHE drillings) are assumed to coincide in the model and were projected directly onto each other (c.f., Figure 3.1 and 3.4). A measured hydraulic head in the Lettenkeuper formation (i.e. in EKB2) was used as an additional constraint to the geodetic monitoring data for model calibration.

### 3.3.2 Numerical model setup

The model domain was set up as a radial-symmetric model, implementing a 2D cross-section around a line source that coincides with the center of the full 3D domain (Figure 3.3). The domain has a vertical extent of 42 m ( $\delta_z = 6$  m), representing the thickness of the swelling zone. The top of the domain coincides with the upper anhydrite level at 62 m bgl, above which no anhydrite is present, while the base of the model coincides with the anhydrite core at 104 m bgl. The model extent in the radial direction was set to 240 m ( $\delta_x = 6$  m), capturing the spatial extent of the observed heave cone at the ground surface (max. radius  $\sim 170$  m) while avoiding boundary effects (c.f., Figure 3.1). Appropriate scaling of the model input parameters for the radial-symmetric approach was considered (Langevin, 2008; Wallis et al., 2013).

The total simulation period was set to 1500 days, discretized into daily time steps. The first phase (P1) of the simulation period (790 days) started on the 3<sup>rd</sup> September 2007, coinciding with the start of the geothermal drilling. At this point in time, water started to migrate from deeper aquifers along defective BHE drillings into the anhydrite bearing claystone of the swelling zone. The second phase (P2) of the simulation period coincides with the initiation of the mitigation measures on 4<sup>th</sup> November 2009 (i.e., after  $\sim 790$  days), after which water ingress into the swelling zone was stopped.

### 3.3.3 Modeling tools

All flow simulations were carried out with the USGS finite-difference groundwater flow model MODFLOW-2005 (Version 1.12.00) (Harbaugh, 2005; Harbaugh et al., 2017). Reactive transport processes were defined and simulated with the reactive multicomponent transport model PHT3D (Prommer et al., 2003), which combines the solute transport model MT3DMS and the geochemical model PHREEQC-2 (Parkhurst and Appelo, 1999). Model calibration was conducted with the nonlinear parameter estimator PEST++ (Doherty, 2015; Welter et al., 2015). All pre- and post-processing scripts were written and executed in Python (Version 2.7.14).

### 3.3.4 Groundwater flow

The model simulates saturated flow in a porous media. Hydraulic conductivity, porosity and specific storage were assumed homogeneous over the entire model domain, and estimated via nonlinear regression (i.e., via PEST++). The vertical conductivity was defined as an anisotropy ratio between horizontal and vertical conductivity (Table 3.2). The model top and bottom were defined as no-flow bound-

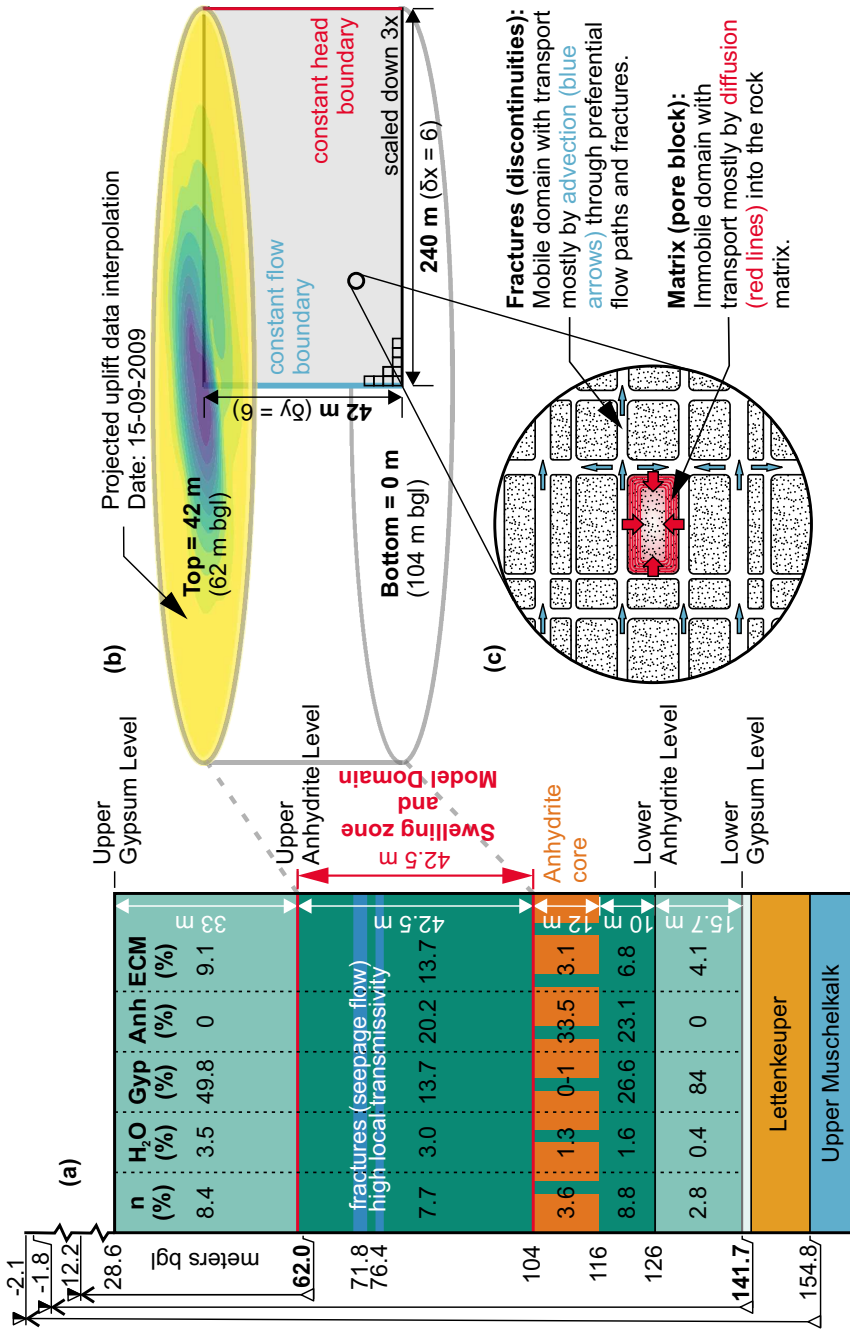


Figure 3.3: (a) Conceptual model set up with homogeneous areas using average values for total porosity (n), water (H<sub>2</sub>O), gypsum (Gyp), anhydrite (Anh) and expansive clay minerals (ECM) based on LGRB (2010). Head values measured at various depths in exploration borehole EKB2 are indicated to the left. (b) A conceptual model depicting the radial symmetric setup with a projected uplift interpolation and the actual modelled domain indicated by the grey area, and (c) a schematic of the dual domain approach.

aries and correspond to the low permeability zones without significant swelling potential above the UAL and below the AC (Figure 3.3). The right-hand model boundary was defined as a constant head boundary, representing a groundwater level of 12.2 m bgl measured in an exploration borehole (EBH2, Figure 3.3) in the Gypsum Keuper at 62 m bgl. Initial heads were defined uniformly across the model domain at 12.2 m bgl on the basis of these measurements. The left-hand boundary of the 2D cross-section (located at the center of the radial symmetric domain) was set as a constant, specified flow boundary, representing the defective BHE drilling as a line source through which water inflow occurs. Water intrusion into the swelling zone most likely occurred along multiple defective BHE drillings. However, given the close proximity of the BHEs (<20 m) it was assumed that they can be represented as a single source. The associated flow rate was estimated as part of the inversion process for both simulation phases ( $Q_{P1}$  and  $Q_{P2}$ ). However, it was assumed that inflow during the second phase ( $t > 790$  days) approached zero due to the implementation of the mitigation measures.

### 3.3.5 Solute transport

While the clay-rich matrix of the unleached Gypsum Keuper formation has a very low permeability with supposedly no free water available for the chemical transformation process, fractures and discontinuities can facilitate flow and the availability of water within the formation, and thus trigger the reaction over a large area (Wittke, 2014). However, these PFPs (i.e., fractures) are presumably limited to a relatively small portion of the total rock volume, with negligible mineral-fluid interaction and residence times too short to allow critical saturation conditions for gypsum precipitation (Hauber et al., 2005). Consequently, the simplifying assumption was made that the mineral-fluid interaction critical for the chemical reaction of sulfates is limited to the rock matrix, which consists of pore spaces containing immobile water with minor or no groundwater seepage velocity (Kresic, 2007). Transport within, into and out of this domain is generally dominated by diffusion.

Thus, two domains are distinguished for swelling clay-sulfate rocks in the model i.e., (i) a mobile domain, which allows for water access to the formation via advection, and (ii) an immobile domain, which considers the low permeability rock matrix, where the potentially rate-limited transformation of anhydrite to gypsum takes place. Accordingly, in the numerical implementation the classical advection-dispersion model was replaced by a dual-domain mass transfer (DDMT) approach, where total porosity is divided into domains of mobile ( $\theta_m$ ) and immobile porosity ( $\theta_{im}$ ). The fluid interaction between both domains is characterized by a mass transfer rate, which is proportional

to the concentration difference between the two domains (Feehley et al., 2000; G. Liu et al., 2007):

$$\theta_{im} \frac{\partial C_{im}}{\partial t} = \zeta (C_m - C_{im}), \quad (3.1)$$

where  $t$  is time,  $\zeta$  is the first-order mass transfer rate coefficient ( $T^{-1}$ ), and  $C_m$  ( $\text{mol L}^{-1}$ ) and  $C_{im}$  ( $\text{mol L}^{-1}$ ) are the solute concentrations in the mobile and immobile domain, respectively.

The longitudinal and transverse dispersivity were set to local-scale values of 1.0 m and 0.05 m, respectively.

### 3.3.6 Geochemical reactions

The transformation of anhydrite into gypsum can be considered as the sequence of two separate processes, anhydrite dissolution ( $\text{CaSO}_4 \longrightarrow \text{Ca}^{2+} + \text{SO}_4^{2-}$ ) and gypsum crystal growth ( $\text{Ca}^{2+} + \text{SO}_4^{2-} + \text{H}_2\text{O} \longrightarrow \text{CaSO}_4 \cdot 2\text{H}_2\text{O}$ ). The kinetics of water-rock interaction are described in the literature by a number of generic rate formulations (Appelo and Postma, 2005; Lasaga, 1984; Lasaga et al., 1994; Mullin, 2001; Nancollas and Purdie, 1964; Rimstidt and Barnes, 1980). Typically the reaction rates depend on the thermodynamics of the system and the mineral reactive surface area (Serafeimidis and Anagnostou, 2013) in a form similar to (Appelo and Postma, 2005):

$$R_i = k_i \phi_i \left( \frac{A_i^0}{V} \right) \left( \frac{m_i}{m_i^0} \right)^n \left( 1 - \frac{IAP}{K_i} \right), \quad (3.2)$$

where  $R_i$  is the reaction rate for mineral  $i$  ( $\text{mol L}^{-1} \text{s}^{-1}$ ),  $k_i$  is the corresponding rate constant ( $\text{mol m}^{-2} \text{s}^{-1}$ ),  $\phi_i$  is the volume fraction,  $A_i^0$  the initial reactive surface area ( $\text{m}^2$ ) of the mineral in contact with a volume  $V$  of solution ( $\text{m}^3$ ),  $m_i^0$  and  $m_i$  are the initial moles of the solid and the moles of solid at a given time,  $IAP$  is the ion activity product and  $K_i$  the equilibrium constant. Both the rate constants and the volume fractions for anhydrite dissolution and gypsum precipitation were estimated via nonlinear regression (Table 3.3). The dependency of the reaction rate on the degree of saturation is expressed by the ratio of  $IAP$  and  $K$ , while variations in the specific surface area ( $A/V$ ) over time are accounted for by the term  $(m_i/m_i^0)^n$ .

The value of parameter  $n$  in Eq. 3.2 is a function of the initial grain size distribution and shape, with  $n = 0.67$  for a monodisperse population of uniformly dissolving spheres as in case of the anhydrite nodules, and approximately  $n = 0.5$  for the elongated, plate-like gypsum crystals (He et al., 1994; Serafeimidis and Anagnostou, 2013; Witkamp et al., 1990).

The initiation of new fractures and changes in porosity are not explicitly considered in our modeling approach as residence times were considered too short for gypsum precipitation to occur in the mobile

domain. Hence, the initial mineral mass ultimately determining the available mineral-fluid interaction area was completely attributed to the immobile domain. Consequently, the solution volume  $V$  in contact with the mineral equals the immobile porosity ( $\theta_{i,m}$ ) instead of the total porosity (Table 3.3). It should be noted that this assumption is different from the model of Ramon, Alonso, and Olivella (2017), who assumed that gypsum crystal growth occurs solely in fractures. The focus of their study, however, was on mechanical considerations such as fracture opening. By assuming an initial fracture aperture of zero, their modeling framework generally agrees with the assumptions of the present study in that the minerals-fluid interaction area is initially represented by the pore space of the rock matrix, until new fractures open and increase the overall permeability, facilitating transport by advection.

The surface area  $A_i^0$  of the minerals was calculated using geometric measures of single grains (Rimstidt and Barnes, 1980). Based on drill cuttings analysis, anhydrite nodules present in the clay matrix were assumed to be spherical with a diameter of  $d = 1.0$  mm (LGRB, 2010), in agreement with previous estimates by Oldecop and Alonso (2012):

$$A_A^0 = \frac{3}{r_A \rho_A}, \quad (3.3)$$

where  $r_A$  is the particle radius and  $\rho_A$  the density of anhydrite. For the gypsum crystals growing during the precipitation process, on the other hand, the shape of elongated platelets with a side ratio of 21 : 8 : 2 and the smallest dimension, ( $S_0$ ) = 0.1 mm, was assumed (Kontrec et al., 2002):

$$A_G^0 = \frac{2(ab + a + b)}{S_0 a b \rho_G}, \quad (3.4)$$

where  $\rho_G$  is the density of gypsum.

Water inflow from outside the system is a basic requirement for clay-sulfate rock swelling to occur and can be regarded as the trigger of the swelling process. Although, measured hydraulic potentials in aquifers above and below the swelling zone suggest that the unleached Gypsum Keuper formation (swelling zone) is located below the groundwater surface, i.e. saturated zone, this formation is typically encountered "dry" in boreholes (e.g., Wittke, 2014). Nevertheless, determination of the water content from drill cores revealed water contents in the swelling zone between 0.1 and 5.6% (3.0% on average; (LGRB, 2010)). These water contents were determined via oven drying at only 40 °C in order to prevent evaporation of water bound by gypsum or clay minerals. Thus, the determined water content corresponds to the content of capillary bound and free (mobile) water, which in turn corresponds to the effective porosity. As the effective porosity of clay rocks is usually in the same order of magnitude as

the measured water content, this suggests that assuming saturated conditions is likely valid.

The phenomenon of swelling that requires water as a reactant was conceptually addressed by assuming the swelling zone to be saturated with water, and by using a reactive water tracer (W) as the anhydrite dissolution catalyst. In this way, a reaction with water within the swelling zone prior to the ingress of water is prevented. At the same time, the reaction front linked to the inflowing groundwater (from underlying aquifers via geothermal drillings) can be traced. In the model, W was added as a constituent of the inflowing “reactive” water with its concentration estimated via nonlinear regression. While this conceptual approach does not provide a detailed process-based description that reflects the multiphase nature of the problem (i.e., “dry” or not fully saturated conditions) and the actual processes taking place at the pore scale, it is well suited as a surrogate model to describe the swelling of clay-sulfate rocks triggered and controlled by water inflow at the field scale. Note that the computational complexity associated with the explicit simulation of the simultaneous saturation and chemical processes is substantial, and rather infeasible for numerical calibration and uncertainty quantification. Therefore, the proposed methodology provides a novel and efficient approach for handling these complex processes in a tractable way.

As the reaction rate of anhydrite dissolution is a function of the mineral-fluid interaction area (specific surface area,  $A/V$ ), and therefore the amount of water (i.e., tracer concentration within the matrix) in contact with the mineral surface, the rate expression in Eq. 3.2 was extended by a concentration dependent term that links the reaction rate of anhydrite dissolution to the tracer concentration:

$$R_A = k_A \phi_A \left( \frac{A_A^0}{V} \right) \left( \frac{m_A}{m_A^0} \right)^{0.67} \left( 1 - \frac{IAP}{K_A} \right) \left( \frac{C_W}{k_{1/2} + C_W} \right), \quad (3.5)$$

where  $k_{1/2}$  is the half-saturation constant and  $C_w$  is the water tracer concentration. Values of the added concentration-dependent term range between 0 and 1, equaling 0.5 for  $k_{1/2} = C_w$  and approaching 1.0 for higher concentrations. Since  $k_{1/2}$  is dependent on the maximum tracer concentration, it was estimated via nonlinear regression.

While the term  $(m_i/m_i^0)^n$  in Eq. 3.2 and 3.5 accounts for changes in surface area ( $A$ ) over time, the solution volume ( $V$ ), which equals the immobile porosity ( $\theta_{im}$ ), is constant throughout the simulation. This assumes that the tracer concentration, rather than the solution volume, exerts a direct control on the rate of the reaction. Conceptually, the concentration-dependent term in Eq. 3.5 represents the amount and availability of “reactive water” present within the rock matrix, i.e., water that can be consumed during the transformation reaction. Unlike the “dimensionless water content” parameter described by Witke (2014), which corresponds to the absolute degree of swelling and

represents a gradient for diffusive transport into the matrix (i.e., high water content equals an advanced stage of swelling), the concentration-dependent term of the present study directly controls the reaction rate of anhydrite as a factor (i.e., high water content enables high reaction rate). Without this term, transformation of anhydrite to gypsum would also occur in the absence of inflowing water, as gypsum is the more stable mineral phase under the geochemical conditions prevailing in the swelling zone.

The following reaction equation links the precipitation of gypsum to the water tracer:



The molar concentration of the water tracer ( $M_W$ ) and that of the inflowing water ( $M_{\text{H}_2\text{O}}$ ) are proportional. Thus, while gypsum precipitates, the water tracer  $W$  is consumed relative to the rate at which water molecules are incorporated into the mineral. Related to the rate of gypsum crystal growth ( $R_G$ ), the following reaction rate ( $R_W$ ) for  $W$  can be deduced:

$$R_W = - \left( \frac{M_W}{M_{\text{H}_2\text{O}}} \right) R_G * 2.0 \quad (3.7)$$

### 3.3.7 Swelling model

The vertical effective stress  $\sigma'_z$  on the swelling zone from overburden was calculated for each depth  $z$  and location  $x$  of the model domain and point in time  $t_p$  of the simulation based on mean lithostatic and hydrostatic pressure:

$$\sigma'_{z,x,t_p} = (1 - \theta_{\text{tot}})\gamma_s z + \theta_{\text{tot}} \gamma_w z - u(x, t_p), \quad (3.8)$$

where  $u$  is the pore water pressure,  $\theta_{\text{tot}}$  is the total porosity,  $z$  is the vertical depth (m) of the model cell, and  $\gamma_s$ , and  $\gamma_w$  are the specific weight of the solid (rock) and liquid phase (water) derived from bulk density data by LGRB (2010), respectively.

In order to relate stress to strain and derive the vertical deformation from the mass of precipitated gypsum crystals determined by the coupled flow, transport and reaction simulations in the swelling zone, a bulking (swelling) coefficient was used, following the work by Oldecop and Alonso (2012), Ramon and Alonso (2013), and Ramon, Alonso, and Olivella (2017):

$$\frac{d\varepsilon_i}{dt} = - \frac{\gamma_i}{\rho_G} \frac{dm_G}{dt}, \quad (3.9)$$

where  $\varepsilon_i$  is the deformation (strain) and  $\gamma_i$  the bulking coefficient in the  $i$  direction, respectively,  $\rho_G$  is the gypsum density ( $\text{kg m}^{-3}$ )

and  $m_G$  the mass of precipitated gypsum crystals (kg). The geomechanical stress – strain relationship is calculated posterior to the completed MODFLOW and PHT3D model simulation using a Python script. Thus, the model does not couple geochemical equilibrium and groundwater flow conditions with in situ stresses. However, the approach is able to capture the overall impact of in situ stress on rock deformation.

The effect of stress (expressed by  $\gamma$ ) is approximated by an exponential decay function:

$$\gamma_i = \gamma_{\max} e^{-b\sigma'_i}, \quad (3.10)$$

where  $\gamma_{\max}$  is the bulking coefficient for zero pressure stress which was set to 2 as in Ramon, Alonso, and Olivella (2017),  $b$  is a model fitting parameter estimated during the inversion process and  $\sigma'_i$  is the effective stress.

Assuming unidirectional deformation in  $z$  within the swelling zone, the total deformation  $\varepsilon$  for all  $n$  depths in  $z$  at a particular location  $x$  of the model domain, and for a specific point in time  $t_p$  of the simulation, can simply be expressed as (Figure 3.4):

$$\varepsilon(x, t_p) = \frac{1}{A(x)} \sum_{t=0}^{t_p} \sum_{z \in n} \gamma(z, x, t) * \Delta V_G(z, x, t), \quad (3.11)$$

where  $V_G$  ( $m^3$ ) is the volume of precipitated gypsum crystals and  $A$  ( $m^2$ ) is the surface area of the grid cell. The elastic deformation of the overburden is assumed to be zero, hence  $\varepsilon$  equals the total heave  $h$  at the ground surface.

Similarly, the total uplift volume at the ground surface  $V$  for a specific point in time  $t_p$  can be obtained by calculating the product of the volume increase from precipitated gypsum crystals  $V_G$  and the corresponding  $\gamma$  for all  $n$  depths in  $z$  and  $m$  locations in  $x$  over the entire model domain:

$$V_{t_p} = \sum_{t=0}^{t_p} \sum_{z \in n} \sum_{x \in m} \gamma(z, x, t) * \Delta V_G(z, x, t), \quad (3.12)$$

### 3.3.8 Model calibration

The inversion of the flow and multi-component transport model was constrained by periodic geodetic measurements of ground uplift and interpolated values of the total heave volume over the entire simulation period. Furthermore, a piezometric head of 1.8 m agl measured within the Lettenkeuper (i.e., in EBH2) was used to constrain head values at the left-hand model boundary for  $t = 700$ . Initial parameter values were based on data collected during the site characterization (hydraulic conductivity, porosity, mineral volume fractions, bulk

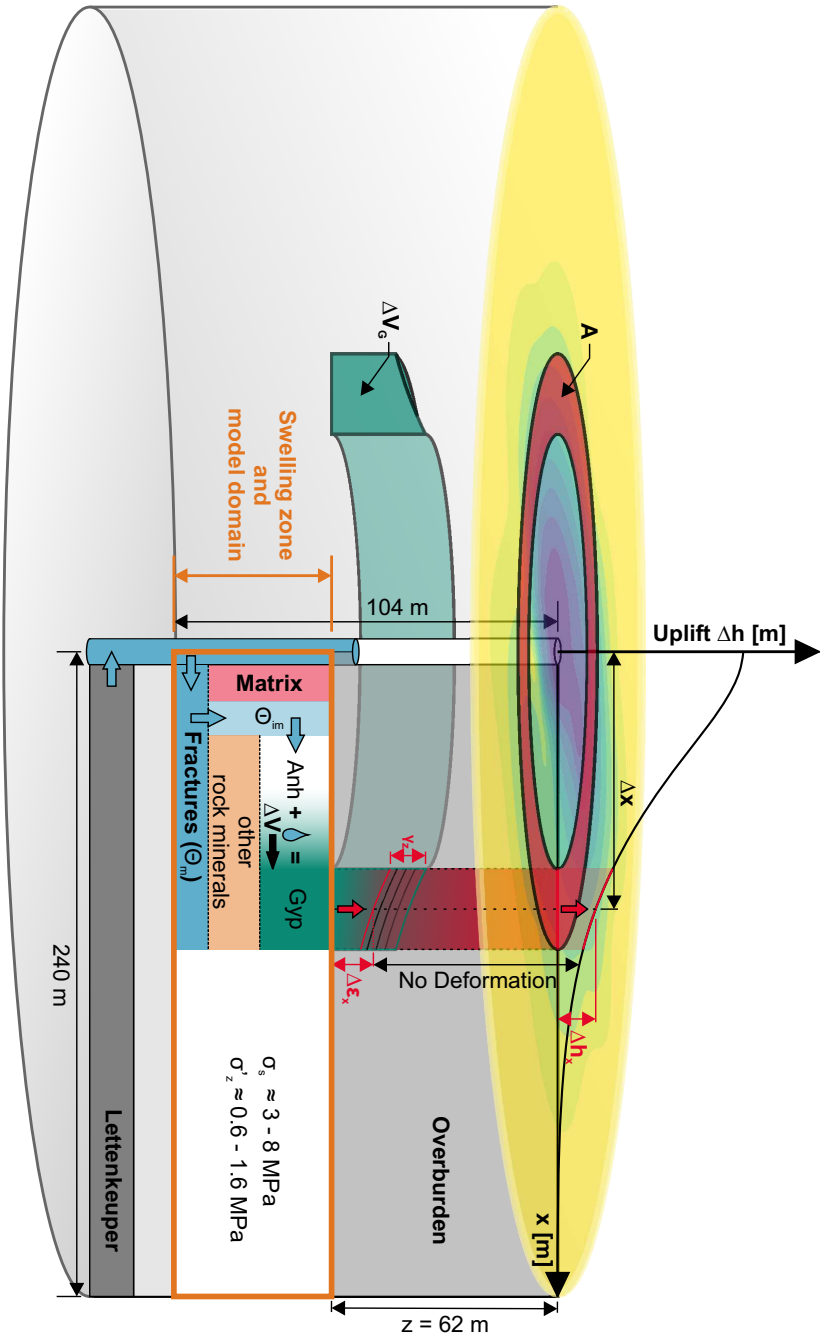


Figure 3-4: Sulfate swelling model that relates the mass of precipitated gypsum crystals to deformation ( $\epsilon$ ) and the heave ( $\Delta h$ ) at the ground surface via a bulking coefficient  $\gamma$ . Average stress conditions are indicated by the swelling stress ( $\sigma'_s$ ) (Steiner, 1993) and the effective vertical stress ( $\sigma'_z$ ).

density) (LGRB, 2010), literature data (reactions constants, storage) (Domenico and Mifflin, 1965; Serafeimidis and Anagnostou, 2013) and on stoichiometric calculations (minimum flow rate).

The parameter values were log-transformed and optimized during the inversion process with PEST++ (Doherty, 2015; Welter et al., 2015). The inversion process minimizes the weighted sum of squared residuals between model output and the corresponding measurements. In order to obtain a stable and unique solution of the inverse problem, Tikhonov regularization was used (Tikhonov and Arsenin, 1977) with the expected values listed in Table 3.2 and 3.3, which were also used as initial values. Mobile and immobile porosity parameters were estimated by relating them to the total porosity ( $\theta_{\text{tot}}$ ) and a ratio parameter ( $\phi_{\text{ratio}}$ ). Furthermore, the total mineral fractions of anhydrite and gypsum was approximated to be 33.8% and constrained by an additional prior information term. The GENLINPRED, IDENTPAR and SUPCALC utilities (Doherty, 2016), and PyEMU (J. T. White et al., 2016) were used to perform a parameter estimability analysis including parameter identifiability and relative parameter error reduction (Doherty and Hunt, 2009).

### 3.4 FIELD OBSERVATION DATA

#### 3.4.1 Groundwater chemistry

The ambient and inflowing water compositions (Figure 3.5) were defined on the base of field observations. However, in the absence of data that would directly characterize the ambient conditions within the unleached Gypsum Keuper below the UAL (Figure 3.3), the groundwater composition was approximated by water samples taken in the overlying gypsum karst (Table 3.1, water sample 71 046). PHREEQC was used to calculate mineral saturation states. The calculations suggest that the ambient groundwater is characterized by high sulfate concentrations of 1482–1533 mg L<sup>-1</sup> and is saturated with respect to gypsum and slightly under-saturated with respect to anhydrite.

Water samples from the Lettenkeuper and Upper Muschelkalk formations, which represent the inflowing groundwater composition, were both highly undersaturated with respect to gypsum and anhydrite (Figure 3.5). However, compared to the Lettenkeuper aquifer, where mineralization is dominated by the dissolution of sulfate minerals, the degree of mineralization in the Upper Muschelkalk is lower and mostly a result of dissolved carbonates (dolomite and calcite). These significant differences in mineral saturation further underpin the hypothesis that there was no vertical exchange between the different groundwater stories prior to the BHE drilling campaign. For the modeling study, the groundwater composition of the inflowing

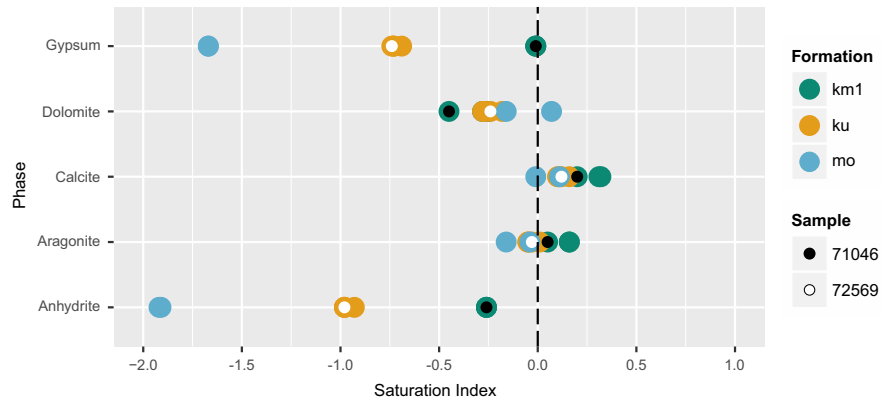


Figure 3.5: Mineral saturation indices in ambient and inflowing groundwater samples (data from LGRB, 2010).

water was taken from the Lettenkeuper formation (Table 3.1, Sample 72 569).

### 3.4.2 Geodetic monitoring network

The geodetic monitoring network (details provided in LGRB (2010)), which recorded the vertical ground heave at the study site, included up to 106 measurement points. All uplift values were referenced to the absolute (and in a few cases projected) elevation at the time before the BHE drilling. Measurements started on 14<sup>th</sup> January 2008 with 14 reference points, after which the network was successively refined until all 106 points were installed (from 18<sup>th</sup> May 2010 onward). In the time period between January 2008 and September 2011, a total of 49 points in time were sampled at irregular intervals of 11 to 63 days.

Two types of observation data were used for model calibration: (1) The point observations of absolute uplift from the geodetic monitoring network (total of 3431 points in space and time), and (2) interpolated volumetric values of total ground heave for selected 23 points in time, which are irregularly distributed over the entire simulated period (i.e selected based on adequate number of measurements from geodetic monitoring network). For type one, observation data from the geodetic network were directly compared to the model output along the x-axis of the cross-section by calculating the distance of all measurement points to the mean center point. However, comparison of normalized mean uplift values shows high data ambiguity for the observation points at a given distance from the center, characterized by a large spread of uplift values (Figure 3.6). This indicates a pronounced anisotropy, especially close to the center, which makes model calibration difficult (see Figure 3.1). Thus, the second type of observation data, the interpolated volumetric values, were calculated by interpolating the point observation data set of each point in time. For this, the radial basic function method employing the multiquadric

Table 3.1: Charge balanced and equilibrated ambient and inflowing water composition (data from LGRB, 2010).

AQUEOUS COMPONENT	UNIT	AMBIENT CHEMISTRY (GIPSKARST)		INFLOW CHEMISTRY (LETTENKEUPER)	
		SAMPLE 71046	RANGE	SAMPLE 72569	RANGE
Temperature	°C	13	13-13.1	15.4	15.4-16.4
pH		6.85	6.85-6.91	7.05	7.03-7.05
pe		4	4	4	4
Alkalinity (HCO <sub>3</sub> )	mol L <sup>-1</sup>	5.9 × 10 <sup>-3</sup>	5.9-7.3 × 10 <sup>-3</sup>	5.5 × 10 <sup>-3</sup>	5.4-5.9 × 10 <sup>-3</sup>
C(4)	mol L <sup>-1</sup>	7.7 × 10 <sup>-3</sup>	7.7-9.3 × 10 <sup>-3</sup>	6.5 × 10 <sup>-3</sup>	6.5-7.0 × 10 <sup>-3</sup>
C(-4)	mol L <sup>-1</sup>	0	0	0	0
Ca	mol L <sup>-1</sup>	1.6 × 10 <sup>-2</sup>	1.6-1.6 × 10 <sup>-2</sup>	5.3 × 10 <sup>-3</sup>	5.3-5.6 × 10 <sup>-3</sup>
Cl	mol L <sup>-1</sup>	2.2 × 10 <sup>-4</sup>	2.2-2.4 × 10 <sup>-4</sup>	1.0 × 10 <sup>-4</sup>	0.9-1.1 × 10 <sup>-4</sup>
Fe(2)	mol L <sup>-1</sup>	3.1 × 10 <sup>-6</sup>	0.3-5.6 × 10 <sup>-5</sup>	1.4 × 10 <sup>-5</sup>	1.3-3.6 × 10 <sup>-5</sup>
Fe(3)	mol L <sup>-1</sup>	2.5 × 10 <sup>-8</sup>	0.2-5.1 × 10 <sup>-7</sup>	6.7 × 10 <sup>-7</sup>	0.6-1.8 × 10 <sup>-6</sup>
K	mol L <sup>-1</sup>	1.1 × 10 <sup>-4</sup>	1.1-2.0 × 10 <sup>-4</sup>	1.7 × 10 <sup>-4</sup>	1.7-9.9 × 10 <sup>-4</sup>
Mg	mol L <sup>-1</sup>	2.4 × 10 <sup>-3</sup>	2.1-2.4 × 10 <sup>-3</sup>	1.8 × 10 <sup>-3</sup>	1.7-1.8 × 10 <sup>-3</sup>
Mn(2)	mol L <sup>-1</sup>	7.7 × 10 <sup>-7</sup>	7.7-8.4 × 10 <sup>-7</sup>	2.9 × 10 <sup>-7</sup>	0.2-4.9 × 10 <sup>-6</sup>
Mn(3)	mol L <sup>-1</sup>	0	0	0	0
N(0)	mol L <sup>-1</sup>	0	0	0	0
N(3)	mol L <sup>-1</sup>	0	0	0	0
N(-3)	mol L <sup>-1</sup>	0	0	0	0
Na	mol L <sup>-1</sup>	9.3 × 10 <sup>-4</sup>	0.9-3.9 × 10 <sup>-3</sup>	2.5 × 10 <sup>-4</sup>	2.5-4.2 × 10 <sup>-4</sup>
S(-2)	mol L <sup>-1</sup>	0	0	0	0
S(6)	mol L <sup>-1</sup>	1.5 × 10 <sup>-2</sup>	1.5-1.6 × 10 <sup>-2</sup>	4.5 × 10 <sup>-3</sup>	4.5-5.0 × 10 <sup>-3</sup>
W (tracer)	mol L <sup>-1</sup>	0	-	1.0 × 10 <sup>-4</sup>	-

kernel function was used. To account for the visible anisotropy of the heave body (c.f., Figure 3.1), the major axis was set to  $30^\circ$ . The extent of all raster outputs was standardized and cropped to a 200 m radius around the center of the heave cone to capture the full extent of the uplifted area in September 2011, while avoiding boundary effects of the interpolation method. Subsequently, volumetric values of total ground heave and the position of the maximum uplift (center point) were calculated for each of the raster datasets (i.e., at different times). Furthermore, it was assumed that the mean location of the center point of all raster datasets coincides with the center of the model domain.

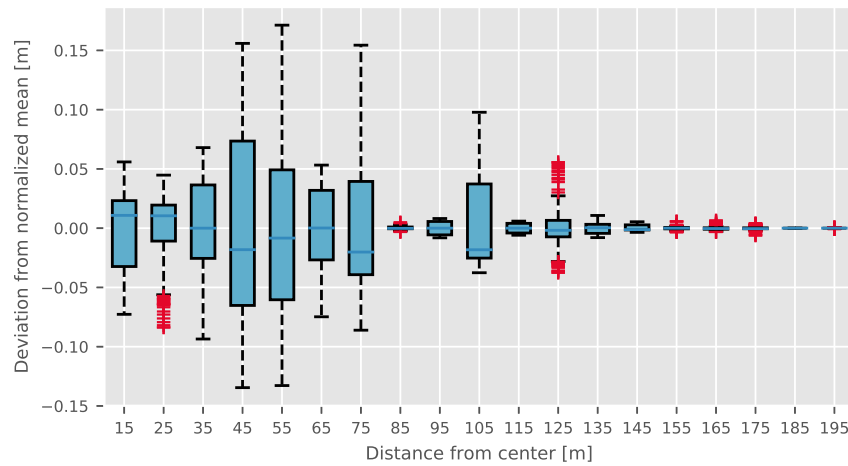


Figure 3.6: Deviation of all uplift observations from a corresponding mean value normalized for each point in time and depending on the distance from the model center (categorized into bins of 10 m). The median is marked by the deep blue bar, while the blue box represents 50% of all values (i.e. the interquartile range (IQR)). Outliers (red) are values  $1.5 \times$  IQR above and below the third and first quartile (i.e. range represented by the whiskers), respectively.

### 3.5 RESULTS AND DISCUSSION

#### 3.5.1 Simulated flow and reactive transport

The model simulation results show that transformation of anhydrite to gypsum was triggered by the intrusion of water into the swelling zone (Figure 3.7). The total simulated anhydrite mineral concentration decreases from an initial value of  $4.15 \text{ mol L}_{\text{bulk}}^{-1}$  (referring to liter of bulk volume) to a minimum of  $3.52 \text{ mol L}_{\text{bulk}}^{-1}$  after 1500 days in the vicinity of the inflow boundary, i.e., the location where the maximum reduction in anhydrite mineral content of 14% occurred. Hence, only a fraction of the total available anhydrite mineral content (1.8%) was

converted within the modeled swelling zone (radius of 240 m) and duration of the simulation (1500 days). This suggests that there is still large potential for future swelling upon further contact with water. Assuming a linear extrapolation of the anhydrite dissolution rate as well as the flow rate towards the end of simulation phase one, a complete transformation of all anhydrite within the swelling zone would take at least another 130 years. Serafeimidis and Anagnostou (2013) demonstrated that hydration times exceeding centuries in duration are indicative for thick anhydrite layers, low porosities and diffusion-limited dissolution rates. The fact that the transfer rate ( $\zeta$ ) and thus diffusion is the limiting factor for anhydrite dissolution can also be deduced from the consistently low tracer concentration (i.e., close to zero) in the immobile domain.

Generally, the two simulation phases are characterized by a change in water inflow conditions, which directly affected the evolution of the chemical transformation of anhydrite to gypsum. The two phases can also be identified by their changing state of chemical equilibrium, because the inflowing water is under-saturated with respect to both gypsum and anhydrite and has a strong effect on the saturation state (Figure 3.7). Both anhydrite dissolution and gypsum precipitation proceed fastest during the first simulation phase (Figure A.1), when rate controlling equilibrium conditions are most favorable for the reaction, and tracer concentrations are high. However, with the change in water inflow conditions, equilibrium conditions are re-established uniformly throughout the model domain and tracer concentrations decrease. As a result, the chemical transformation slows down.

The change in gypsum concentration ( $\Delta\text{Gypsum}$ ) is proportional to the decrease in anhydrite concentration, indicating that the dissolution and precipitation processes are temporally and spatially correlated, and calcium and sulfate ion transport is negligible (Figure 3.7). This is also apparent from the absence of gypsum precipitation within the mobile domain. However, this absence can be attributed to the simplifying model assumption that only homogeneous gypsum crystal growth takes place (Eq. 3.2), and neither inert minerals nor anhydrite were considered as possible heterogeneous nucleation and precipitation sites. With the initial mobile mineral concentration of gypsum and anhydrite assumed to be zero, gypsum growth in the water delivering discontinuities is not accounted for. Therefore, it is plausible to assume that the rate of gypsum precipitation is actually higher due to the additional mineral surface available for crystal growth. Although growth of gypsum crystals in discontinuities has been observed and documented in previous studies as critical to the overall swelling process (e.g., Alonso and Olivella, 2008; Alonso and Ramon, 2013), it is conceptually most relevant when mechanical processes and changes in porosity are considered. In the present study, in contrast, it is assumed that the critical concentration for gypsum

precipitation is not reached within discontinuities of the mobile domain due to a comparatively small specific surface area and high flow velocities (Hauber et al., 2005). The immobile phase thus represents areas of the rock volume in which, due to the substantially longer residence times, the transformation process is favored. The distinction made in the present modeling concept is therefore still compatible with previously presented modeling approaches.

### 3.5.2 Simulated ground heave

Two types of observation data were used to constrain the model calibration: direct point measurements of uplift (Figure 3.8) and interpolated volumes of the heave cone (Figure 3.9). The inversion process resulted in a plausible model (i.e. parameterization in accordance with site measurements and literature values) that generally matches well with observed heave at most locations of the geodetic measurement network (see supporting information for a more detailed description).

The comparison of the simulated heave with point measurements, while generally showing a reasonable match, also shows two distinct characteristic deviations (Figure 3.8b). First, the heave at the observation point locations differ systematically from the corresponding simulated values, resulting in a greater spread around the 1:1 centerline over time, creating a fan-like shape. This can be attributed to the anisotropy of the heave body (ellipsoidal shape), which results in notable differences in the measured uplift at equidistance to the center (c.f., Figure 3.1 and 3.6) that cannot be reproduced by the radial-symmetric model. This causes the model to over- or under-predict the measured uplift depending on the location of the measurement.

Secondly, all values shown in the 1:1 relationship flatten off asymptotically after implementation of the mitigation measures ( $t = 790$  days). The mean measured heave rates only decline to  $3.6 \times 10^{-2} \text{ mm d}^{-1}$  at the end of the simulation period, while mean simulated heave rates decline to  $1.0 \times 10^{-2} \text{ mm d}^{-1}$  and converge towards zero (Figure A.2). The same trend is apparent in Figure 3.8a, where the simulated uplift for  $t = 1110$  days and  $t = 1470$  are almost identical, although geodetic heave measurements show a persistent uplift for most measurement points.

The simulated increase in heave volume is generally in good agreement with the interpolated volumes of the heave cone (Figure 3.9). The calculated root mean square deviation (RMSD) and the Fréchet distance for the volumetric values were  $328.7 \text{ m}^3$  and  $496.4 \text{ m}^3$ , respectively. Total increase in volume at the end of the simulation amounts to  $6385 \text{ m}^3$  (Figure 3.9a), with the heave-time-curve approaching a plateau slightly below the interpolated value of  $6833 \text{ m}^3$  after 1500 days. In general, a systematic underestimation of the volume by the model can be observed. However, this is in line with the compara-

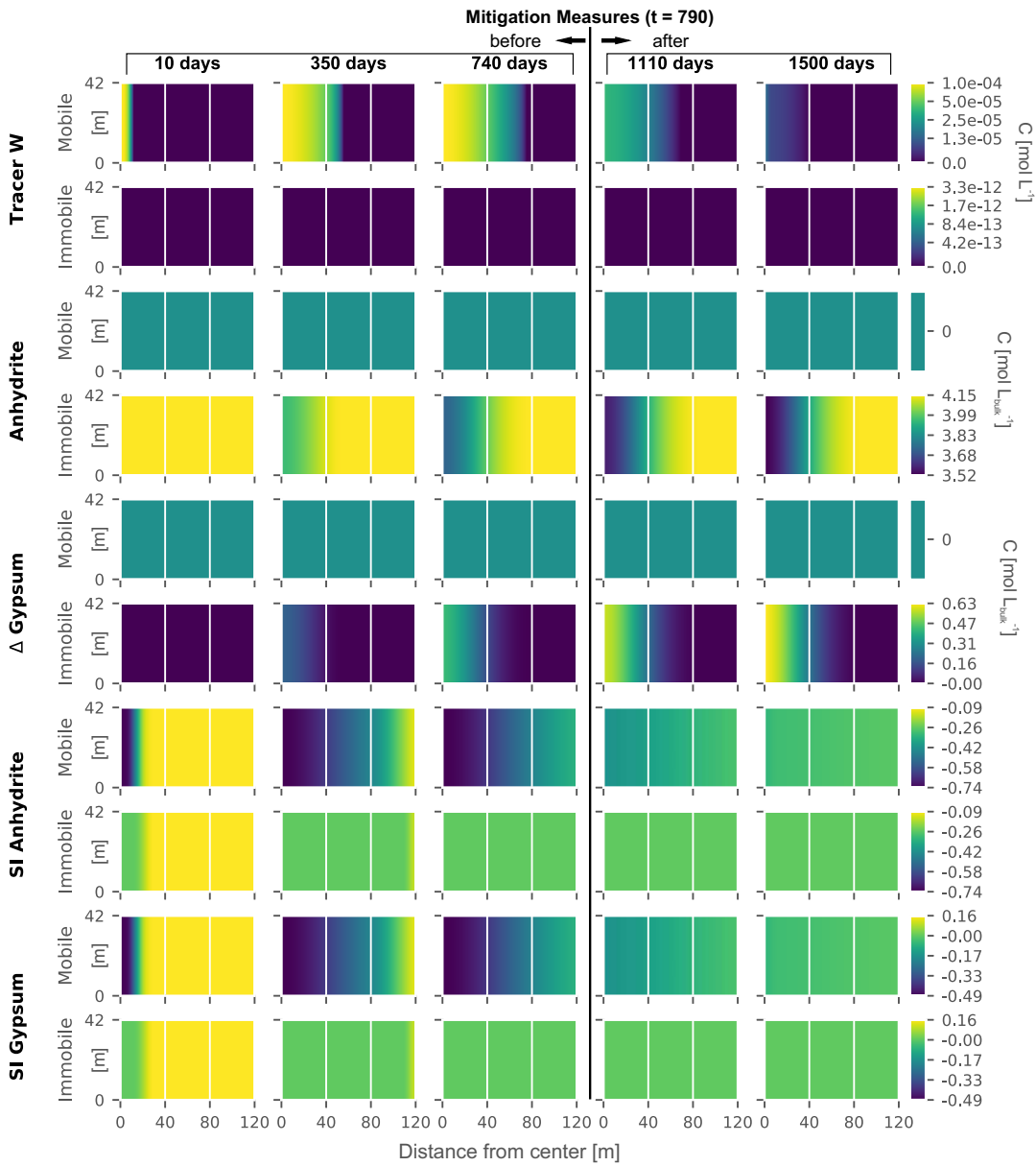


Figure 3.7: Simulated concentrations of water tracer (W), the mineral anhydrite and the change in gypsum concentration, and saturation index (SI) of anhydrite and gypsum along the investigated cross-section of the symmetric radial model. Mineral concentrations are given with respect to liter of bulk volume. Five representative points in time before (10, 350 and 740 days) and after (1110 and 1500 days) initiation of the mitigation measures (t = 790) are visualized for a radial extent of 120 m.

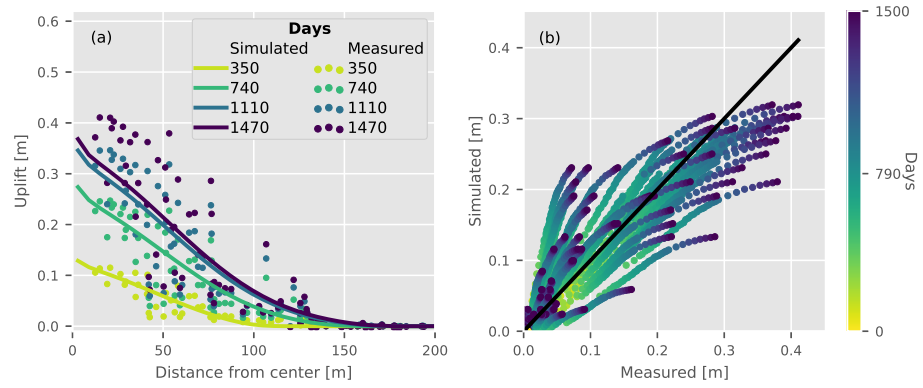


Figure 3.8: (a) Comparison of geodetic heave measurements with simulated uplift along the cross-section for four representative points in time (see legend). (b) 1:1 relationship of measured vs. simulated uplift. The evolution of the observation points over time is indicated by the color scale.

tively good fit of uplift values because total volume estimates are increasingly affected by deviations between simulated and measured uplift rates with distance from the model center (Figure 3.6). Furthermore, while uplift rates at the inflow boundary are relatively high (causing the comparatively large average simulated uplift values depicted in Figure A.1), they have little effect on the simulated total volume of the heave due to the radial model geometry. Thus, changes in volume from uplift close to the center of the model domain are insignificant.

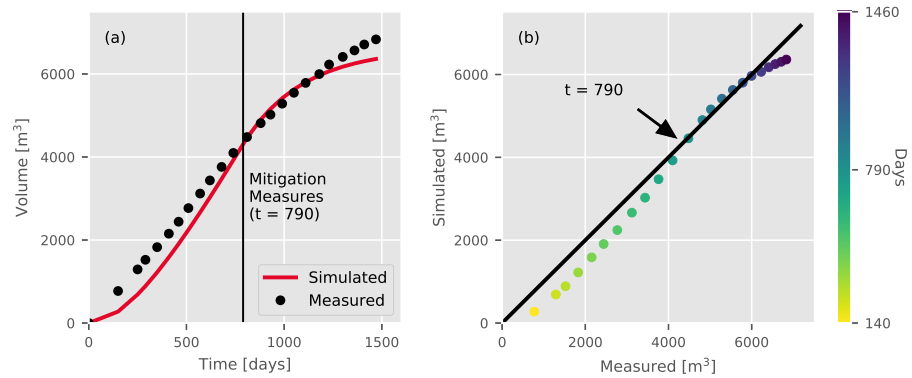


Figure 3.9: (a) Comparison of the volume increase of the heave body measured at the surface with the volume increase due to anhydrite to gypsum transformation calculated with the model. (b) 1:1 relationship of measured vs. simulated volume increase. The volume increase over time is indicated by the color scale.

According to stoichiometric calculations, the remaining water within the swelling zone would only have been sufficient to sustain another 635 m<sup>3</sup> of gypsum crystals from precipitation and a volume increase

of  $96 \text{ m}^3$ , considering a mean geomechanical bulking coefficient of 0.16. These simulation results indicate that the residual water in the system was exhausted by the anhydrite to gypsum transformation during the second simulation phase, which caused a near cessation of the uplift process. At the study site, however, attenuated uplift was observed even well beyond the end of the simulated period ( $t > 1500$  days). An explanation for this discrepancy is that either our hypothesis of  $Q_{P2}$  approaching zero is not valid and significant amounts of water still intrude into the swelling zone after the start of the mitigation measures ( $t > 790$  days); or that the model underestimated the initial flow rate  $Q_{P1}$  and larger amounts of water have been stored within the swelling zone and are subsequently made available, for example by expansive clay minerals such as corrensite, or adsorbed water (Hauber et al., 2005), or through capillary suction.

However, the systematic deviation in the volume estimates could also hint at some unidentified and uncaptured processes. For example, the feedback from mechanical stress on flow conditions is not represented in the model. While the adopted bulking coefficient  $\gamma$  accounts for the effect of in-situ stresses on deformation, it does not consider the feedback associated with the opening of fractures and pathways from gypsum crystal growth, as well as crystal growth in existing porosities, on the flow simulation. To account for this feedback, time-dependent permeability changes, the total porosity, the porosity ratio and the hydraulic conductivity would require updating while the mass transfer rate coefficient  $\zeta$  would have to be variable over time. The consideration of this process would likely increase the accessibility of water to anhydrite grains, which may explain the under-estimation of the heave volume in the simulations. At the same time, neither clay swelling due to hydration of clay minerals nor osmotic water uptake is considered. These processes proceed much faster than sulfate swelling and facilitate initial water access to the formation, thus providing an additional explanation for the underestimated heave volume. Similarly, the redistribution of pore water from clay interlayer/surfaces (i.e., dehydration of clays) into the free porosity (effective porosity) may enhance water availability, also leading to an under-estimation of the actual uplift rates, especially during simulation phase two, when water inflow ceases. However, progression and intensity of the redistribution are dependent on temperature, pressure and the concentration gradient between inter-layer pore water and the effective porosity and may even require explicit consideration of a third model domain.

The observed heave at the ground surface during the first simulation phase and before implementation of the mitigation measures (pumping) could to some extent also be attributed to a rise in pore water pressure while water was intruding into the swelling zone, thereby acting as a lifting force and reducing the effective stress. Similarly,

reduced pore water pressures might be partially responsible for reduced uplift rates after the mitigation measures. This would mean that the reaction-induced observed uplift is initially over-, and later, underestimated by the model. Another consideration is that the actual local geological setting is more complex than its representation in the numerical model. Thus, the formation of gypsum at a particular location may not express itself as uplift directly above that location (Eq. 3.11).

The deviations between the simulated and observed heave can also have a variety of other reasons. For example, setting the initial sulfate mineral concentration in the mobile domain to zero neglects the fact that a fraction of the mineral mass may be in direct contact with the water of the PFPs. This could cause anhydrite dissolution and possibly also gypsum crystallization in the discontinuities, assuming that the critical concentration for gypsum precipitation is reached in the mobile domain under the prevailing flow conditions (i.e., comparatively high flow rates). Consequently, the change in rock volume and the amount of anhydrite being dissolved, particularly in the initial phase, may be more pronounced than predicted by the calibrated model. Furthermore, due to size exclusion effects, only a fraction of the water-bearing immobile porosity might be available for diffusive transport, thereby affecting the mineral-fluid interaction area to be considered (Huysmans and Dassargues, 2005). Additionally, due to the lack of more detailed observation data, the hydraulic conductivity of the swelling zone was only represented by a single value, resulting in a unidirectional flow field (c.f., Figure 3.7). A spatially differentiated parameterization of the swelling zone, especially in the vertical direction, would contribute to a more realistic model of the hydrodynamic conditions and the spread of the reaction front. To this end, continuous head measurements or laboratory scale investigations on changes in permeability during swelling could have assisted with filling some of the remaining knowledge gaps.

### 3.5.3 Estimated parameters

Final calibrated values of the key model parameters along with the corresponding initial estimates deduced from field measurements and literature data are listed in Table 3.2 and 3.3. The estimated horizontal conductivity coincides well with values reported from the unleached Gypsum Keuper formation at depths between 50 to 100 m bgl by Ufrecht (2017) and thus are considered plausible.

The estimated flow rate  $Q_{P1} = 2.9 \times 10^{-4} \text{ m}^3 \text{ s}^{-1}$  was above the minimal flow rate of  $1.3 \times 10^{-4} \text{ m}^3 \text{ s}^{-1}$  that was stoichiometrically required to provide sufficient water to allow for the total observed volume increase of  $6833 \text{ m}^3$  at the ground surface after 1500 days. This can mostly be attributed to the low value of  $\gamma$ , substantially increasing

Table 3.2: Hydraulic parameter initial values taken from two reports (LGRB, 2010, 2012) and literature data (Domenico and Mifflin, 1965) together with PEST++ model parameter estimates, posterior standard deviation (STDV) and parameter boundaries.

PARAMETER	SYMBOL	UNIT	INITIAL VALUE	MODEL ESTIMATE	POSTERIOR STDV
Hydraulic Conductivity <sup>a</sup>	$K_h$	$\text{m s}^{-1}$	$1.0 \times 10^{-7}$	$3.5 \times 10^{-7}$	$7.8 \times 10^{-8}$
Flow Rate Phase 1 <sup>a</sup>	$Q_{P1}$	$\text{m}^3 \text{s}^{-1}$	$1.3 \times 10^{-4}$	$2.9 \times 10^{-4}$	$6.6 \times 10^{-5}$
Flow Rate Phase 2 <sup>a</sup>	$Q_{P2}$	$\text{m}^3 \text{s}^{-1}$	0.0	$8.4 \times 10^{-8}$	$7.9 \times 10^{-8}$
Specific Storage	$S_s$	$\text{m}^{-1}$	$1.0 \times 10^{-4}$	$1.0 \times 10^{-4}$	$6.1 \times 10^{-5}$

<sup>a</sup>Inversion model input value units were in  $\text{d}^{-1}$ .

the amount of precipitated gypsum required to attain the observed deformation. As expected, the inflow estimated for the second simulation phase remained close to zero ( $Q_{P2} = 8.4 \times 10^{-8} \text{ m}^3 \text{ s}^{-1}$ ), thus adding little to the total increase in volume.

The inversely determined parameter  $b$  of 2.5 is similar to the estimate by Ramon, Alonso, and Olivella (2017) and yields a bulking coefficient  $\gamma$  of  $0.15 \pm 0.11$  (For further details on  $\gamma$  refer to the supporting information). Thus, according to the theoretical basis of  $\gamma$  a large part of the gypsum crystals precipitates in already existing cavities and therefore does not cause significant deformation. Consequently, future work should consider a direct coupling with the geomechanics in order to account for changes in porosity caused by gypsum precipitation and anhydrite dissolution. In general, however, it can be assumed that the changes in the porosity caused by precipitation are partially compensated by the aforementioned development of new flow paths and voids, and therefore, despite the lack of feedback and excepting these processes in the model, the porosity estimates can still be considered plausible.

The total porosity was included as an adjustable parameter estimated by PEST++. Estimated values correspond well to the average measured porosity of 7.7% (LGRB, 2010). The mobile porosity was initially set to 3.0%, based on measurements of free water content, but was successively reduced to 0.6% during the model calibration. Thus, the connected pore space containing mobile water contributes only a small fraction to the total porosity, but at the same time results in a relatively high fluid velocity of  $5.4 \times 10^{-5} \text{ m s}^{-1}$ , which promotes rapid lateral spread. Accordingly, the estimated immobile porosity is relatively high at 7.1% (91.7% of the total porosity). These results emphasize that even if the proportion of discontinuities facilitating ad-

vection within the rock volume is small, water inflow into the swelling zone is sufficient to trigger and sustain swelling.

The estimated value for  $k_{1/2}$ , which exerts an additional control on the mineral-fluid interaction, was estimated at  $1.6 \times 10^{-6} \text{ mol L}^{-1}$  during the inversion. Based on the estimated  $k_{1/2}$  value, the anhydrite reaction rate reaches 99% for the maximum estimated water tracer inflow concentration of  $1.0 \times 10^{-4} \text{ mol L}^{-1}$ . The water tracer concentration gradient between the mobile and immobile domain remains steep throughout the simulation, indicating that the transfer (diffusion) rate of the water tracer into the matrix is the decisive factor for the rate of anhydrite dissolution and, therefore, the chemical transformation process.

The model-estimated reaction rate constants for anhydrite dissolution and gypsum precipitation are  $k_A = 2.4 \times 10^{-5} \text{ mol m}^{-2} \text{ s}^{-1}$  and  $k_G = 3.2 \times 10^{-6} \text{ mol m}^{-2} \text{ s}^{-1}$ , respectively. Both values compare well with previously reported ranges ( $k_A = 0.4\text{--}4.0 \times 10^{-5} \text{ mol m}^{-2} \text{ s}^{-1}$ ,  $k_G = 0.2\text{--}3.1 \times 10^{-5} \text{ mol m}^{-2} \text{ s}^{-1}$ ) (Serafeimidis and Anagnostou, 2012a). The surface area determined by means of geometric measures of individual particles or crystals, assuming a single particle size, is an idealization, neglecting particle size distribution, surface roughness and porosities and thus typically underestimates the reactive surface area (Rimstidt and Barnes, 1980). On the other hand, selective and non-uniform precipitation limited to active mineral sites, such as growing gypsum crystals, may cause the reactive surface area to be smaller than the geometric surface area and highly variable in space and time. Overall, this emphasizes the importance of assessing the reactive surface area when it comes to determining meaningful reaction rates.

Furthermore, the specific surface area, and thus the reaction rate of reactive minerals, is also affected by the matrix porosity  $\theta_{im}$  (i.e., volume of water in contact with the solid phase) and the mineral volume fraction, both parameters being estimated by the model. The estimated mineral fractions of gypsum (13.7%) and anhydrite (19.1%) were in good agreement with the average values ( $13.6 \pm 21.2$ )% and ( $20.2 \pm 17.8$ )% that were measured in the swelling zone. Ramon and Alonso (2013) demonstrated that the initial anhydrite content has a strong effect on the intensity of the swelling process. Moreover, in cases where anhydrite is not only present as finely dispersed particles but also as distinct layers, diffusion can become a rate-controlling factor for anhydrite dissolution because of the self-sealing effect of growing gypsum layers, a process that can cause porosities to decrease over time (Serafeimidis and Anagnostou, 2013). At the same time, the reactive surface area in contact with the aqueous solution is much smaller (Rauh and Thuro, 2007; Wittke, 2014). The mineral content estimate for anhydrite can therefore be taken as the minimum value that is required to achieve the simulated anhydrite dissolution

Table 3.3: Reactive and solute transport as well as mechanical fitting parameter initial values taken from survey (LGRB, 2010) and literature data (Barton and Wilde, 1971; Ramon, Alonso, and Olivella, 2017; Serafeimidis and Anagnostou, 2013) together with PEST++ model parameter estimates, posterior standard deviation (STDV) and parameter boundaries.

PARAMETER	SYMBOL	UNIT	INITIAL VALUE	MODEL ESTIMATE	POSTERIOR STDV
Gypsum Rate Constant <sup>c</sup>	$k_G$	$\text{mol m}^{-2} \text{s}^{-1}$	$2.9 \times 10^{-6}$	$3.2 \times 10^{-6}$	$2.6 \times 10^{-6}$
Anhydrite Rate Constant <sup>c</sup>	$k_A$	$\text{mol m}^{-2} \text{s}^{-1}$	$2.2 \times 10^{-5}$	$2.4 \times 10^{-5}$	$1.9 \times 10^{-5}$
Half Saturation Constant <sup>b,c</sup>	$k_{1/2}$	$\text{mol L}^{-1}$	$1.0 \times 10^{-6}$	$1.0 \times 10^{-6}$	$1.3 \times 10^{-6}$
Tracer Concentration	$C_W$	$\text{mol L}^{-1}$	$1.0 \times 10^{-4}$	$1.0 \times 10^{-4}$	$9.5 \times 10^{-5}$
Mass Transfer Rate <sup>b,c</sup>	$\zeta$	$\text{s}^{-1}$	$1.0 \times 10^{-10}$	$2.4 \times 10^{-10}$	$4.9 \times 10^{-11}$
Gypsum Volume Fraction <sup>d</sup>	$\phi_G$	%	13.6	13.7	6.2
Anhydrite Volume Fraction <sup>d</sup>	$\phi_A$	%	20.2	19.1	8.7
Total Porosity <sup>d</sup>	$\theta_{\text{tot}}$	%	7.7	7.7	3.0
Porosity Ratio	$\phi_{\text{ratio}}$	[-]	$3.9 \times 10^{-1}$	$8.8 \times 10^{-2}$	$3.4 \times 10^{-2}$
Mobile Porosity <sup>a,d</sup>	$\theta_m$	%	3.0	0.6	-
Immobile Porosity <sup>a,d</sup>	$\theta_{\text{im}}$	%	4.7	7.1	-
Mechanical Fitting Parameter	$b$	[-]	2.0	2.5	$2.3 \times 10^{-1}$

<sup>a</sup> Values derived from total porosity and ratio estimates.

<sup>b</sup> Initial values are not supported by literature data and were estimated.

<sup>c</sup> Inversion model input value units were  $\text{d}^{-1}$ .

<sup>d</sup> Inversion model input values were in decimals instead of percentage.

rates, but can be considerably higher for massive anhydrite banks and low diffusion coefficients in general.

### 3.5.4 Parameter uncertainty analysis

An evaluation of the calculated posterior parameter covariance of the PEST++ calibrated model in conjunction with the prior information showed that the uncertainty in the estimated parameters has been notably reduced upon calibration (Figure 3.10a). The relative reduction in uncertainty, which is indicated by the relative change in variance of the estimated parameter values, was nearly 100 % for the mechanical fitting parameter ( $b$ ), the transfer rate parameter ( $\zeta$ ), the flow rate ( $Q_{P1}$ ) and the hydraulic conductivity ( $K_h$ ), and at least 35 % for all other parameters. Thus, parameters are generally well informed by the observation data.

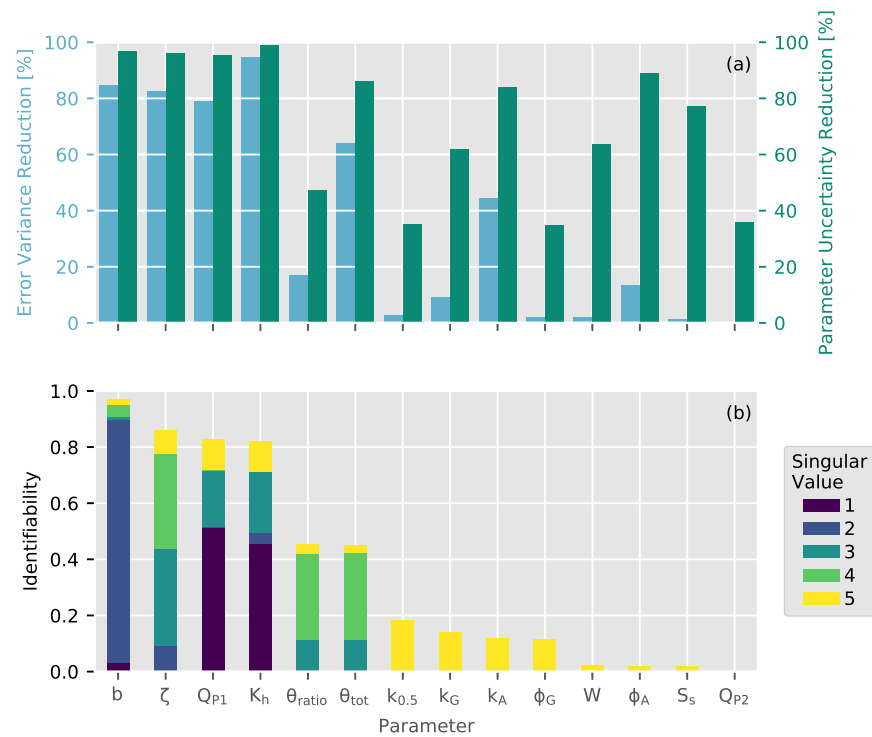


Figure 3.10: (a) The reduction in error variance together with the relative reduction in parameter uncertainty based on the upper and lower boundaries of the prior distributions and posterior parameter covariance. (b) Identifiability of the PEST++ estimated parameters, color coded by the individual contribution of singular values, with warmer colors correspond to higher index singular values.

However, the relatively small reductions in parameter uncertainty of the geochemical parameters indicate that they may not be reliably determined by the model. This is confirmed by the calculated iden-

tifiability measure, assuming a calibration solution space dimension of five (Figure 3.10b). With a value of one indicating complete identifiability, the values below 0.2 of the geochemical parameters  $b$  are low in comparison, as is the value of the flow rate during phase two of the simulation ( $Q_{P2}$ ) at  $1.0 \times 10^{-3}$ . The composite scale sensitivity for those parameters was also low in comparison, indicating that low parameter identifiability is likely due to insensitivity. Thus, the low identifiability of the geochemical parameters show that these parameters can be compared only to a limited extent with literature values. Conversely, the geomechanical fitting parameter  $b$  has a high identifiability. It is quite sensitive and thus decisive for the model result.

In conjunction with the relative parameter error reduction (Figure 3.10a), it is apparent that for the four most identifiable parameters, parameter error has been dramatically reduced upon calibration (Doherty and Hunt, 2009). Overall, the parameter uncertainty analysis shows that data from geodetic measurement networks are generally suitable as observation data for calibration of the model.

It is important to note that due to some simplifying assumptions in our modeling approach (i.e., the aforementioned unrecognized physical processes and missing feedback mechanisms), and the presence of systematic patterns in the residuals, there may be bias in our parameter estimates, which may prevent them from being implemented directly at another site. Nevertheless, the overall methodology proposed in this study is itself applicable to any other site where similar processes are occurring.

### 3.6 CONCLUSIONS

In this study we developed a numerical modeling approach that quantifies the swelling-induced heave as a function of the geochemical transformation from anhydrite to gypsum. Our process-based approach provides an important link between the spatially and temporally varying heave and a range of key hydrogeological, solute and reactive transport processes. The results for the selected study site show a generally good agreement with the geodetic monitoring data, while the model parameters that were estimated via nonlinear regression were found to be plausible. The four most identifiable parameters were the mechanical fitting parameter  $b$ , the mass transfer rate  $\zeta$ , the flow rate  $Q_{P1}$  and the hydraulic conductivity  $K_h$  with values of 2.5,  $2.4 \times 10^{-10} \text{ s}^{-1}$ ,  $3.5 \times 10^{-7} \text{ m s}^{-1}$  and  $2.9 \times 10^{-4} \text{ m}^3 \text{ s}^{-1}$ , respectively. Furthermore, the estimate of both the anhydrite and gypsum reaction rate constants compared particularly well with literature values. The model results indicate that diffusion plays a decisive role in controlling the rate of anhydrite dissolution and therefore, the transformation and swelling process. Ultimately, these results contribute to a better understanding of the controls of the swelling mechanisms that

occur in clay-sulfate rocks and assist with assessing the feasibility of mitigation measures to counteract the swelling problem.

The developed dual domain reactive transport modeling approach is able to simulate transient hydrogeological and geochemical conditions in swelling clay-sulfate rocks. For our study site, the model reproduced observed ground heave by post processing the simulated spatially and temporally variable transformation of anhydrite to gypsum, thus providing a promising and easy-to-implement approach for the field-scale simulation of the swelling and heave process. The approach captures the swelling process reasonably well, although some of the model's limitations will need to be addressed in future studies.

With respect to our study site, the model results of this work support the assumption that heave at the ground surface in the city of Staufen is a consequence of a locally changing groundwater flow regime and the thereby induced hydrogeochemical disequilibrium.

The interplay between chemical reactions, changes in rock structure and texture, and fluid transport properties remain critical for the prediction of hydrological and geochemical processes in swelling clay-sulfate rocks. In order to improve implementation of the chemical reaction processes, anhydrite dissolution along fracture surfaces (mobile domain) and heterogeneous gypsum crystal growth within discontinuities as well as the pore matrix may explicitly be considered as proposed by Serafeimidis and Anagnostou (2012a). The present model may also be extended to include a mechanical model in order to couple changes in rock structure and texture (i.e., changing porosity and sealing effects), and the reaction rates and hydraulic conductivity. Finally, in light of the spatial variability of the geodetic measurements, heave data might be integrated even more effectively by weighting the observation data according to their orientation to the anisotropy axes, or by using representative 2D cross-section models along the major anisotropy axes instead of a radial symmetrical model.

### 3.7 ACKNOWLEDGMENTS

Financial support for D. Schweizer from the German Research Foundation (DFG) under grant number BU 2993/2-1 and from the Graduate School for Climate and Environment (GRACE) is gratefully acknowledged. We thank the Geological Survey of Baden-Wuerttemberg (LGRB), especially Gunther Wirsing and Clemens Ruch, for the provision of digital data. We also thank the Landratsamt Breisgau - Hochschwarzwald and the city of Staufen for the provision of geodetic measurements. The observation data used are listed in the references (LGRB, 2010, 2012), Table 3.1 and the supporting information. Furthermore, two model scripts used to generate the model input files

and to couple the MODFLOW and PHT<sub>3</sub>D models with PEST are provided in the supporting information.



## Part IV

### ANALYZING THE HEAVE OF AN ENTIRE CITY: MODELING OF SWELLING PROCESSES IN CLAY-SULFATE ROCKS

This study is submitted to the Elsevier journal *Engineering Geology* and is under review. Part IV contains the submitted manuscript.



## ANALYZING THE HEAVE OF AN ENTIRE CITY: A CASE STUDY

---

### ABSTRACT

Ground source heat pump (GSHP) systems play a key role in the exploitation of shallow geothermal energy as a renewable energy source. In clay-sulfate rocks, however, rock swelling is a major threat to the success of GSHP projects that may require extensive and costly countermeasures to mitigate the effects. Swelling is in these cases triggered by water ingress into expansive anhydrite bearing rock layers, followed by the chemical transformation of the sulfate mineral anhydrite to gypsum upon contact with water. Thus, assessing, understanding and quantifying coupled hydraulic and geochemical changes in the swelling zone is essential for selecting effective countermeasures. The present study examines these processes for a study site in Staufen, Germany, where an improper borehole heat exchanger (BHE) installation has allowed ingress of water into the clay-sulfate bearing strata of the Gipskeuper, followed by swelling and substantial heave of the land surface. A reactive transport model was employed to isolate the key processes and to evaluate a range of mitigation scenarios. The model simulations allowed for the assessment of (i) water inflow into the swelling zone, (ii) water availability for the transformation of anhydrite into gypsum within the swelling zone, and (iii) the potential for future swelling for each of the considered scenarios. Our results indicate that even with incomplete BHE sealing, water flow into the swelling zone and thus the swelling process can be arrested through appropriate hydraulic countermeasures. In contrast, our worst case scenario simulation predicts a further 10 cm of heave at the ground surface by 2025. The results illustrate the importance of integrating geological, hydraulic and geochemical information when assessing and predicting the efficiency of site-specific mitigation measures.

### 4.1 INTRODUCTION

Utilizing shallow geothermal energy is an increasingly popular form of renewable energy in many parts of the world (Lund and Boyd, 2016). A well-established technology to exploit this source of energy is the use of ground source heat pump (GSHP) systems (Sanner et al., 2003). While the technology has enormous potential in saving energy used for heating and cooling of buildings, and thus reducing global CO<sub>2</sub> emissions (Bayer et al., 2012), it also entails a range of

site-specific risks (Butscher, Huggenberger, Auckenthaler, et al., 2011). In recent years several incidents of GSHP installations caused significant damages to houses, for example in Germany (Fleuchaus and Blum, 2017) and in France (Catoire et al., 2017; Kimmel and Hadadou, 2016). One of the main risks and causes of damage lies in accidentally triggering hydraulic short circuits, i.e., in facilitating a hydraulic connection between previously separated aquifers as a result of a GSHP installation (Grimm et al., 2014). While consequences can be manifold, a hydraulic short circuit is particularly problematic when geological formations with clay and sulfate minerals are involved, such as the commonly found Triassic Gipskeuper (“Gypsum Keuper” or Grabfeld-Fm.) formation in Germany (Anagnostou, Serafeimidis, et al., 2014).

Clay-sulfate rocks swell upon contact with water due to two partially superimposed processes (Butscher, Breuer, et al., 2018; Butscher, Mutschler, et al., 2016): (i) Clay swelling through hydration and osmotic water uptake (Madsen and Müller-Vonmoos, 1989), and (ii) sulfate swelling, a chemical transformation of anhydrite ( $\text{CaSO}_4$ ) into gypsum ( $\text{CaSO}_4 \cdot 2\text{H}_2\text{O}$ ). The latter process is considered to be the main mechanism of swelling in such rocks (e.g., Wittke, 2014), resulting in a net volume increase of up to 61 % and producing very high swelling pressures of up to 16 MPa (Steiner, 1993).

Hydraulic short circuits induced by improper borehole heat exchanger (BHE) installation can cause swelling processes that result in considerable heave of the ground surface and massive damage to houses and infrastructure. For example, noteworthy occurrences in Germany include incidents at sites in Böblingen, Rudersberg and Staufen im Br. (LGRB, 2010, 2013, 2015) as summarized by Fleuchaus and Blum (2017).

Mitigation measures to stop the swelling process typically include (re-)grouting of the defective (improperly cemented) boreholes and the installation of pumping wells. Both are aimed at preventing additional water ingress into the anhydrite bearing strata. However, there is typically a lack of detailed data and process understanding, thus preventing a reliable prediction of the rate and duration of the swelling and associated uplift (Butscher, Mutschler, et al., 2016). The main reason for this uncertainty is that it is generally unknown how much water has already entered the swelling zone, and how much of it remains available for the transformations of anhydrite into gypsum. In addition, regional and local groundwater flow and hydrological boundary conditions decisively influence the swelling process (Butscher, Einstein, et al., 2011; Butscher, Huggenberger, and Zechner, 2011; Butscher, Huggenberger, Zechner, and Einstein, 2011). However, it also remains unclear how well any hydraulic mitigation measures can prevent additional water ingress once the local hydrogeological conditions are disturbed. In order to more reliably predict

the efficiency of remediation measures, a more comprehensive process understanding and quantitative tools that simulate and quantify the key processes are urgently needed. The perhaps most important knowledge gap appears to be a lack of understanding on how the various hydrogeological and geochemical processes interact. Therefore, a coupled quantification of these processes, which explicitly accounts for the feedback between these mechanisms, plays a crucial role for improving our conceptual understanding and quantitative forward predictions of swelling processes. Tackling this challenge, several different numerical model approaches for simulating the swelling of clay-sulfate rocks were developed in recent years, mostly, however, investigating the swelling processes in the context of tunnel constructions (e.g., Anagnostou, 1993; Oldecop and Alonso, 2012; Olivella and Alonso, 2008; Ramon and Alonso, 2018; Ramon, Alonso, and Olivella, 2017). These models all incorporate coupled hydro-mechanical-chemical processes with the objective of providing a detailed description of the swelling process. Their application identified gypsum crystal growth as the driving mechanism of swelling. On the other hand, Schweizer, Prommer, Blum, Siade, et al. (2018) developed a novel reactive transport model approach that jointly considers both, swelling from gypsum precipitation due to the spatio-temporal changes in geochemical as well as the shift in hydraulic regimes that is caused by geotechnical engineering activities. In their study, geodetic monitoring data of the ground heave at their study site in Staufen was employed to guide the development and calibration of a radial-symmetric, and thus geometrically simplified field-scale model and to subsequently identify critical processes and model parameters.

In the present study we eliminate many of the previously made simplifications and refine our earlier developed reactive transport model by incorporating a significant portion of the geological complexity that was originally defined by a detailed 3D geological model of the study area (Schweizer, Blum, et al., 2017). This allows us now to explicitly and more realistically account for the impact of the local groundwater flow patterns and the water ingress that was induced via the BHE drillings that created some preferential flow paths (PFP). We use this refined model to explore different mitigation measures and to assess their efficiency on slowing down or even stopping the clay swelling process. We also employed these new model simulations to investigate the origin of the ingressing water and to more precisely quantify the role of water availability for the transformation of anhydrite into gypsum in the swelling zone. Eventually the results were used to assess the future swelling potential for each of the investigated scenarios.

## 4.2 STUDY SITE

Our study site is located in the historic city of Staufen in South-West Germany (Figure 4.1), where an improper BHE installation into the local clay-sulfate bearing formation has caused severe damage. Since the drilling of the vertical BHEs in 2007, the city of Staufen has been subject to ground heave with uplift rates of up to 11 mm month<sup>-1</sup> (LGRB, 2010), which is still ongoing. To date this has resulted in a total ground heave of up to 60 cm. Overall the incident caused damage to more than 250 houses with costs so far exceeding 50 Mio. € (Fleuchaus and Blum, 2017). From previous analysis of the case it is now evident that the incomplete annular sealing (improper cementation) of at least one of the seven drilled BHE created a hydraulic connection between a previously separated artesian aquifer and the overlying Gipskeuper (Grimm et al., 2014; LGRB, 2010; Ruch and Wirsing, 2013; Sass and Burbaum, 2010). Due to the ingress of water, anhydrite embedded in the Gipskeuper was chemically transformed into gypsum, which in turn led to a net increase in rock volume and, thus, swelling.

Various mitigation measures started in 2009, including (i) (re-)grouting of the defective BHE; and (ii) installation of pumping wells into the artesian aquifer underlying the Gipskeuper, with the aim of lowering the hydraulic potential in this aquifer below the level of the swelling zone (Ruch and Wirsing, 2013). Although these measures have effectively reduced the ground surface heave rates, they have so far failed to completely stop the swelling.

Supporting the design and planning of the mitigation measures, an extensive exploration campaign was carried out to investigate the geological, hydrogeological and chemical conditions of the subsurface in the vicinity of the affected area (Benz and Wehnert, 2012; LGRB, 2010, 2012). This included detailed measurements of groundwater hydrochemical compositions, piezometric heads, hydraulic transmissivities, storage coefficients and porosities, as well as drill core investigations and a seismic campaign to determine the geological strata, their thickness and composition. Furthermore, a geodetic observation network comprising 106 measurement points was set up to monitor the surface deformation at the study site (Figure 4.1). Between January 2008 and March 2015, a total of 67 surveys at irregular intervals of between 11 and 161 days were performed. The intervals were adapted to the uplift dynamics and increased progressively.

Geologically, Staufen is located at the eastern margin of the southern Upper Rhine Graben (URG) within the so called "Sulzburg-Staufener Vorbergzone" (Genser, 1958). This zone is a transition zone between the graben itself to the west and the crystalline massive of the Black Forest to the east, where it is delimited by the eastern main boarder fault (EMBF) (Groschopf et al., 1981). The zone is composed

of staggered fault blocks that got trapped at the graben margin during rifting, thereby creating a zone of high structural complexity. At the study site, this zone mainly consists of steeply inclined Mesozoic strata, typically displaced by west dipping faults and covered by Quaternary sediments (Sawatzki and Eichhorn, 1999) (Figure 4.2).

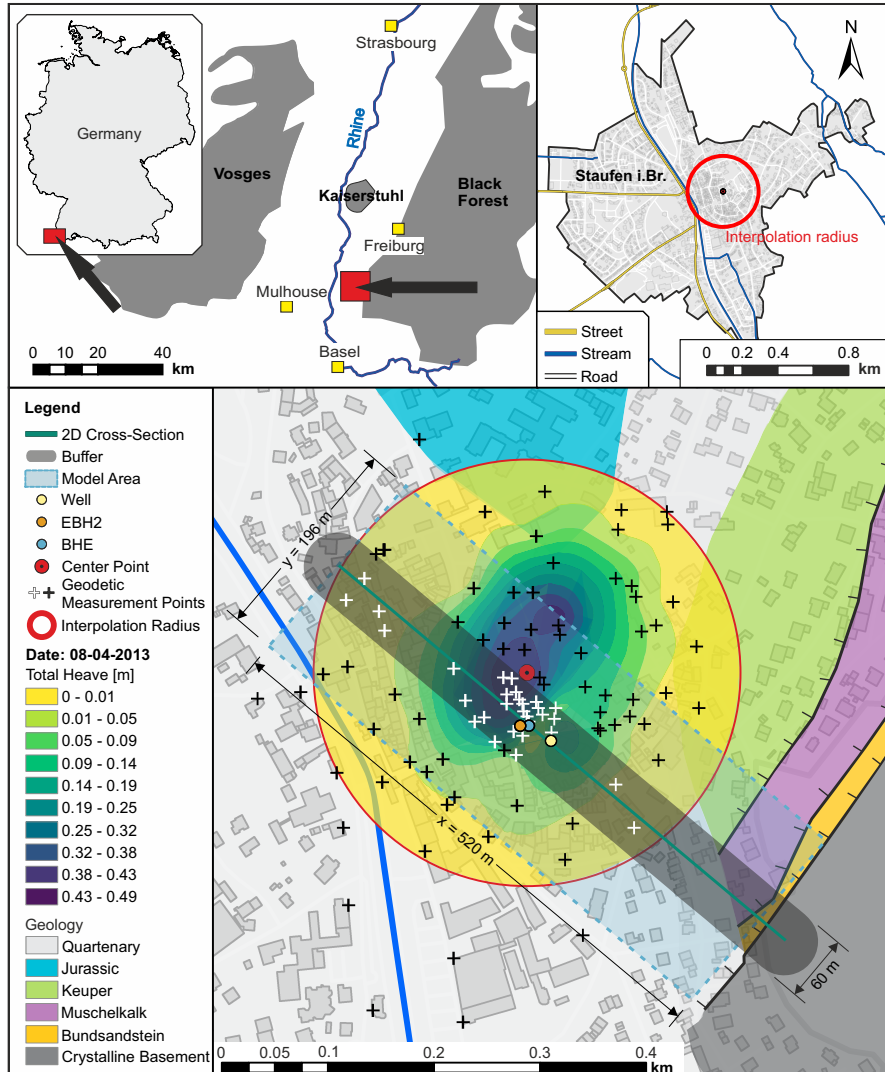


Figure 4.1: Overview of the study site (BHE = borehole heat exchanger, EBH2 = site investigation well).

In the present study, three particular formations play an important role: (1) The Gipskeuper (Grabfeld-Fm., Table 4.1), which contains the anhydrite bearing strata (swelling zone), underlain by (2) the Lettenkeuper (Erfurt-Fm.) and (3) the Upper Muschelkalk (Rottweil-Fm.) (Figure 4.2). The latter two are artesian aquifers, which are both thought to be responsible for groundwater inflow into the swelling zone via the defective BHE drillings. The Lettenkeuper is a fractured rock aquifer of 5 to 10 m thickness composed of alternating sandstone, mudstone and dolomitic limestone. The Upper Muschelkalk consists

Table 4.1: Stratigraphy and geological formations with terminology used by regional geologists and the nomenclature according to STD (2016) given in brackets.

STRATIGRAPHY			FORMATION	
Triassic	Keuper	Middle	km2	Schilfsandstein (Stuttgart-Fm.)
			km1	Gipskeuper (Grabfeld-Fm.)
	Lower	ku	Lettenkeuper (Erfurt-Fm.)	
	Muschelkalk	Upper	mo	Oberer Hauptmuschelkalk (Rottweil-Fm.)

of karstified carbonate rock, which represents a regional aquifer of approximately 60 m thickness. Hydrochemical analysis confirmed that prior to the geothermal drilling, these three geological formations were hydraulically separated (LGRB, 2010).

The rocks of the Gipskeuper are composed of mudstone and marlstone with an average thickness of 100 to 110 m. The formation contains both anhydrite ( $\text{CaSO}_4$ ) and gypsum ( $\text{CaSO}_4 \cdot \text{H}_2\text{O}$ ). Based on the degree of leaching and the presence of either anhydrite or gypsum as the dominating sulfate-mineral, the formation is divided into three zones (Ufrecht, 2017; Wittke, 2014). The first zone is the weathered Gipskeuper, where all sulfate was dissolved and ultimately depleted, which created an aquifer of high permeability (gypsum karst). This zone is typically found at the top and bottom of the formation. The boundary to the second zone, the non-weathered Gipskeuper, is given by the upper (at the top) and lower (at the bottom) gypsum level (UGL and LGL, respectively). The non-weathered Gipskeuper is rich in sulfates and generally of very low permeability. The mineralogical composition in the Gipskeuper changes gradually from a zone where gypsum is the sole sulfate mineral (second zone) towards the center of the formation, where an increasing proportion of anhydrite (third zone, swelling zone) is found. The upper and lower anhydrite level (UAL and LAL) mark the boundary of the third zone where anhydrite appears, hence also delineating the swelling zone. The swelling zone is also characterized by a high content of the expansive clay mineral corrensite (up to 40%; LGRB, 2010). Thin layers of clay, anhydrite and gypsum alternate in this zone, and millimeter-sized anhydrite nodules are finely dispersed within the clay matrix (LGRB, 2010). Although permeability is generally low, sections of increased permeability are evidenced by drilling fluid losses in one of the exploration boreholes (see site investigation well EKB2 at 76.4 m bgl in Figure 4.2), indicating the presence of fractures or PFPs that facilitate lateral groundwater flow.

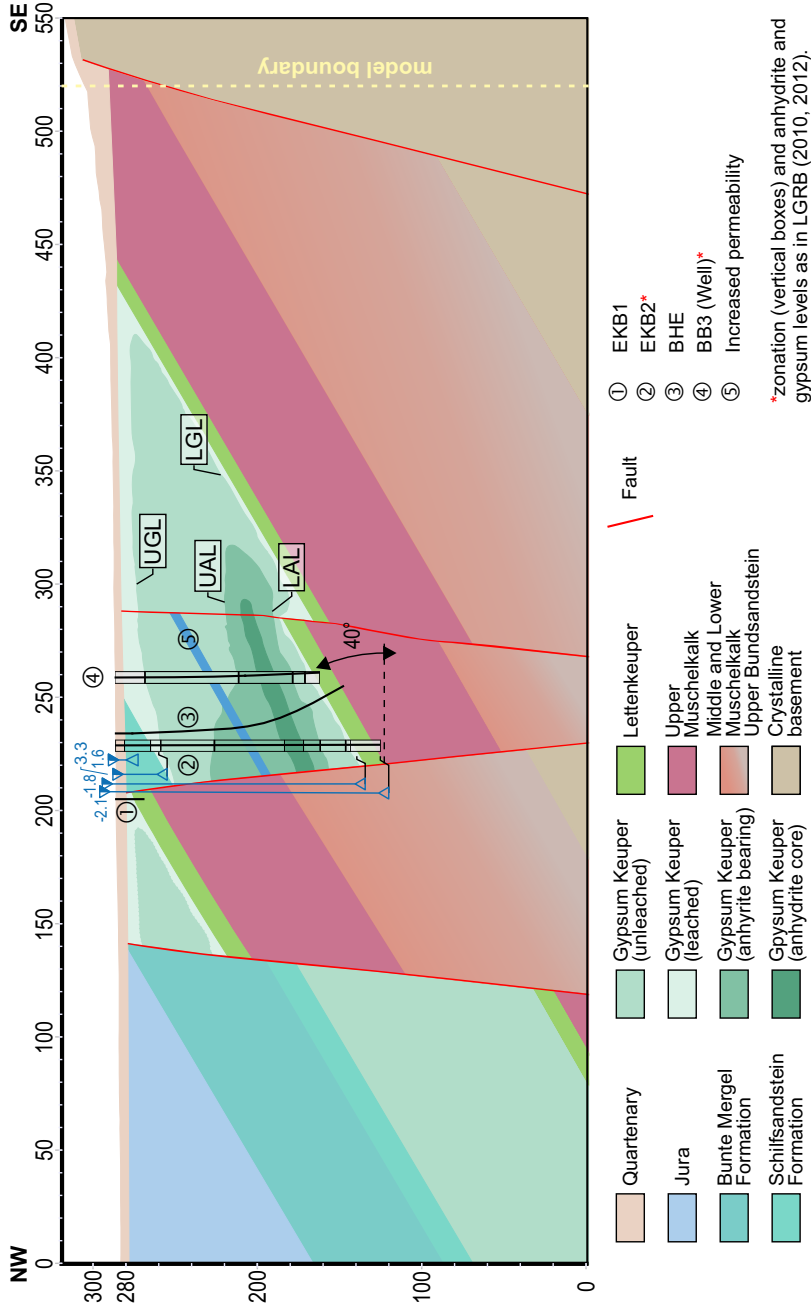


Figure 4.2: 2D cross section as adapted from the 3D geological Model. German stratigraphic nomenclature of the Triassic used by regional geologists (Ezold and Franz, 2005; Nitsch et al., 2005), which partly differs from the new denotation of the geological formations (Table 4.1). UGL = Upper Gypsum Level, UAL = Upper Anhydrite Level, LAL = Lower Anhydrite Level, LGL = Lower Gypsum Level, EKB1 and EKB2 = site investigation wells.

### 4.3 MODELING APPROACH

#### 4.3.1 *Modeling tools*

Flow simulations were carried out with the USGS finite-difference model MODFLOW-2005 (Version 1.12.00), which simulates groundwater flow in saturated porous media (Harbaugh, 2005; Harbaugh et al., 2017). FloPy (Bakker et al., 2016) was used for pre- and post-processing. Reactive transport was simulated using the reactive multicomponent transport model PHT3D (Prommer et al., 2003). It combines the geochemical model PHREEQC-2 (Parkhurst and Appelo, 1999) with the solute transport model MT3DMS (Zheng, 2010). Model calibration was conducted with the nonlinear parameter estimator PEST++ (Doherty, 2015; Welter et al., 2015). All pre- and post-processing scripts were executed in Python (versions 3.6.6).

#### 4.3.2 *Numerical modeling framework*

##### 4.3.2.1 *Overview*

The principal geological framework underpinning the reactive transport modeling study was defined by an earlier constructed 3D geological model (Schweizer, Blum, et al., 2017). The present study, however, focused on a complex representative 2D transect (Figure 4.2), which was extracted from the 3D geological model. The selected transect is oriented in NW-SE direction parallel to the main groundwater flow direction (approximately perpendicular to the graben structure). It includes the BHE drilling site, the extent of the heave body at the ground surface, and all (known) relevant geological structures that may impact the swelling phenomena at the site. The zonation of the Gipskeuper (weathered Gipskeuper and non-weathered Gipskeuper containing gypsum and/or anhydrite) was based on exploration data published in LGRB (2010, 2012). Given their close proximity (<20 m), the seven installed BHE on site are represented as one single BHE in the model.

##### 4.3.2.2 *Spatial and temporal discretization*

The model domain has a vertical extent ( $z$ ) of 320 m and includes the geological strata down to the base of the artesian aquifers under the swelling zone. The horizontal extent ( $x$ ) is 520 m, with the main boundary fault of the graben near the southeastern model boundary. The 2D transect is extended on both sides in the  $y$ -direction by 98 m to result in a 2.5D (“quasi-3D”) model. This step was necessary in order to assign volumetric flow rates to the pumping wells that correspond to measured pumping rates. The 2.5D transect approach was selected as it reduced the overall computational costs dramatically, compared

Table 4.2: Stress periods of the numerical model.

STRESS PERIOD	DURATION <sup>a</sup> [DAYS]	DESCRIPTION	END DATE OF PERIOD
0	1	Steady state before geothermal drilling	3 <sup>rd</sup> Sept 2007
1	810	Geothermal drilling; inflow of groundwater along defective BHE	17 <sup>th</sup> Nov 2009
2	30	Grouting of the BHE to stop inflow of groundwater	18 <sup>th</sup> Dec 2009
3	320	Pumping in EKB2 at $1.35 \text{ l s}^{-1}$	1 <sup>st</sup> Nov 2010
4	120	Pumping in EKB2 at $2.35 \text{ l s}^{-1}$	1 <sup>st</sup> Mar 2011
5	820 <sup>b</sup>	Pumping in EKB2 and BB3 at $2.15$ and $3.55 \text{ l s}^{-1}$	1 <sup>st</sup> June 2013
6	2040	Pumping in EKB2 and BB3 at $1.8$ and $2.3 \text{ l s}^{-1}$	1 <sup>st</sup> Jan 2019
7	2190	Pumping continues for scenario S1, but not for scenarios S2 and S3	1 <sup>st</sup> Jan 2025

<sup>a</sup> numbers are rounded to the nearest tens.

<sup>b</sup> end of calibration period after 770 days.

to a full 3D model. The grid resolution was set to 4 m in the vicinity of the BHE and pumping wells (EKB2 and BB3), increasing stepwise to 8 m and 16 m in the x- and y-direction, respectively. Layer thicknesses were set constant at 4 m.

The total simulation period was 6330 days, discretized into time steps of 10 days. The start of the simulation coincides with the start of the BHE drillings on 3<sup>rd</sup> September 2007. Seven stress periods were used to account for the varying hydraulic stresses caused by the drilling and mitigation measures (i.e., grouting and pumping). Stress periods 1 to 5 were based on data documented by LGRB (2010, 2012), while stress periods 6 and 7 reflect future behavior and thus the assumptions that were made for the corresponding remediation scenarios (Table 4.2).

#### 4.3.3 Setup of the flow model

The model simulates saturated flow in porous media. Estimates for hydraulic conductivities were mainly deduced from site-specific transmissivity measurements (LGRB, 2010), complemented by literature data (LUBW, 2005) and partially estimated via nonlinear regression using PEST++ (Table 4.3). Hydraulic conductivities were assumed to

be isotropic, because the steeply inclined strata strongly deviate from the orientation of the model grid. The specific storage  $S_s$  was set to  $1.0 \times 10^{-5} \text{ m}^{-1}$  for all strata, except for the aquitards of the Jurassic (J) and the Middle Muschelkalk and Bundsandstein strata (MSaqt), for which  $S_s$  was set to  $1.0 \times 10^{-6} \text{ m}^{-1}$  (Domenico and Mifflin, 1965).

At the northwestern model boundary (towards the graben), a constant head boundary was applied. Corresponding to measurements in the closest exploration borehole (LGRB, 2010) hydraulic heads were set to 282 m at the top and successively increased to 284 m at the bottom. The lower part of the southeastern model boundary (towards the graben shoulder) was defined as a no-flow boundary (contact to the crystalline basement behind the main boundary fault). The upper section of this boundary was defined as a constant head boundary (Quaternary and Muschelkalk aquifers). With a constant head value set to 288.5 m this results in an average hydraulic head gradient of 1.25 % within the model domain, coinciding with regional scale measurements (LGRB, 1977). The groundwater recharge rate was set to a uniform value of  $200 \text{ mm yr}^{-1}$  throughout the model domain (LUBW, 2012)). The model's lower boundary coincides with the top of the underlying aquitard and was therefore defined as a no-flow boundary.

The BHE drilling and the two extraction wells were implemented as multi node wells using the MNW<sub>2</sub> package for MODFLOW (Konikow et al., 2009). The hydraulic conductance (CWC) of the well skin (i.e., gravel pack or damaged backfilling) was calculated based on the skin ( $r_{\text{skin}}$ ) and well radius ( $r_w$ ), and the hydraulic conductivity of the skin ( $k_{\text{skin}}$ ). The latter value was estimated via nonlinear regression, while the radii were taken from LGRB (2010, 2012). The EKB<sub>2</sub> and BB<sub>3</sub> drillings (both pumping wells) at the center of the model are implemented in the model with an offset to the transect of 8 m and 4 m, respectively. Faults in the model were implemented using the horizontal flow barrier (HFB) package for MODFLOW (Hsieh and Freckleton, 1993), which changes the cell to cell conductance along the fault through a characteristic value. This value is equal for all faults of the model and estimated via nonlinear regression.

#### 4.3.4 Setup of the reactive transport model

The reactive transport modeling framework is based on the approach presented by Schweizer, Prommer, Blum, Siade, et al. (2018). In brief, this framework includes: a) the chemical reaction of anhydrite to gypsum, b) a "dual domain" approach separating the domain into a mobile domain to represent relatively rapid advective flow/transport, e.g., in fractures and other preferential flow paths and an immobile, reactive domain (rock matrix), with mass transfer between the two domains being driven by concentration gradients c) the use of a "water tracer" that traces inflowing water into the swelling zone. The tracer

Table 4.3: Hydraulic and transport model properties of geological units.

GEOLOGICAL UNIT	SYMBOL	HYDRAULIC CONDUCTIVITY [M/S]	EFFECTIVE POROSITY	IMMOBILE POROSITY
Quaternary	Q	$5.0 \times 10^{-4}$	0.11 (b)	0.21 (b)
Jurassic	J	$1.0 \times 10^{-8}$	0.20	0.10
Bunte Mergel	km3	$1.0 \times 10^{-7}$	0.20	0.10
Schilfsandstein	km2	$8.0 \times 10^{-6}$	0.09 (b)	0.1 (b)
Gipskeuper (unweathered)	km1	$1.0 \times 10^{-10}$	0.02 (b)	0.04 (b)
Gipskeuper (weathered)	km1w	$2.0 \times 10^{-5}$	0.16 (b)	0.16 (b)
Gipskeuper (anhydrite bearing)	km1A	$9.6 \times 10^{-7}$ (a)	0.04 (a)	0.04 (a)
Gipskeuper (fractured)	km1f	$8.3 \times 10^{-5}$ (a)	0.05 (a)	0.04 (a)
Gipskeuper (anhydrite core)	km1c	$1.0 \times 10^{-10}$	0.01 (b)	0.02 (b)
Lettenkeuper	ku	$1.0 \times 10^{-5}$	0.02 (b)	0.05 (b)
Upper Muschelkalk	mo	$5.0 \times 10^{-5}$	0.06 (b)	0.10 (b)
Upper Muschelkalk (below swelling zone)	moS	$6.0 \times 10^{-5}$ (a)	0.16	0.10
Middle Muschelkalk and Buntsandstein aquitards	MSaqt	$1.0 \times 10^{-8}$	0.30	0.10

(a) estimated via nonlinear regression (i.e., via PEST++).

(b) averaged based on measurement (LGRB, 2010).

is a water constituent of all aquifers of the model. By following this approach, only water that intrudes from aquifers into the swelling zone triggers and subsequently “feeds” the chemical transformation of anhydrite to gypsum. In the following, the term “ingressed water” is used for the water tracer to describe the water that has entered the swelling zone.

The effective porosity of geological formations in the model is taken from drill core measurements (LGRB, 2010), or assumed at 20 %, where no measurements were available (Table 4.3). The longitudinal dispersivity was estimated via nonlinear regression and the ratio of transverse vs longitudinal dispersivity was fixed at 0.1. The chemical groundwater compositions that were employed in the model correspond to measured compositions at the study site (LGRB, 2010, 2012). Lateral inflow and recharge concentrations of the water tracer and other water constituents were set equal to the initial ambient water compositions.

#### 4.3.5 Calculation of heave

The change (net increase) in rock volume from dissolved anhydrite and precipitated gypsum within the swelling zone and the resulting heave at the ground surface were calculated based on the approach presented in full detail in Schweizer, Prommer, Blum, Siade, et al. (2018). Briefly, the approach accounts for the effective vertical stress  $\sigma'_z$  in the swelling zone exerted by the overburden, and comprises a bulking (swelling) coefficient  $\gamma$ , as introduced by Oldecop and Alonso (2012) and Ramon and Alonso (2013). This coefficient is used to establish a relationship between stress and strain, i.e., it modifies the change in rock volume originating from gypsum crystal growth depending on stress conditions:

$$\gamma = \gamma_{\max} e^{-b\sigma'}, \quad (4.1)$$

where  $\gamma_{\max}$  is the bulking coefficient at  $\sigma = 0$  (no stress), which was set to the value 2 (according to Ramon, Alonso, and Olivella, 2017),  $b$  is a fitting parameter estimated during the inversion process, and  $\sigma'$  is the effective stress. This approach accounts for the often observed fact that swelling deformation (heave) can be reduced by the opposing vertical effective stress exerted by the overburden on the swelling zone (Grob, 1972; E. Pimentel, 2007).

The heave at the land surface originating from the (stress-modified) volume increase in the swelling zone was calculated based on an approach by Mogi (1958). The approach is commonly used as an analytical volcano deformation source model (Lisowski, 2006). However, Heimlich et al. (2015) showed that it can also be used to relate geodetic measurements of uplift to water leakage from an improperly sealed borehole. Thus, in the absence of a fully process-based

mechanical model, this approach can provide a reasonable approximation for the propagation of the deformation in the swelling zone to the ground surface. In this approximation the surface deformation is expressed as a function of the volume increase of a spherical source, which is embedded in an isotropic elastic half-space (Figure 4.3). The approach accounts for the elastic deformation of the strata above the swelling zone. However, the model assumes isotropic and homogeneous conditions and neglects the orientation of the geological strata.

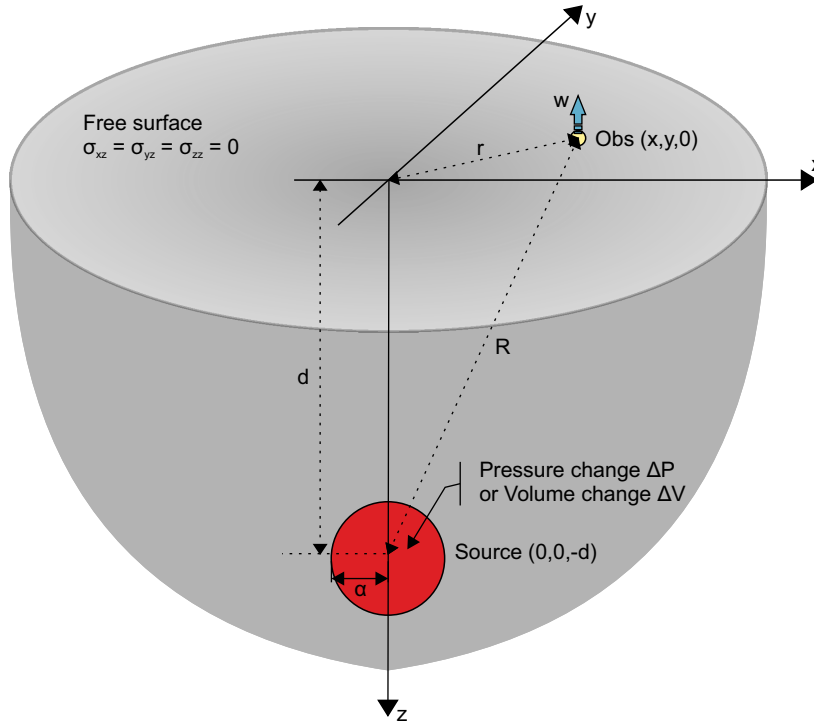


Figure 4.3: Coordinate system and geometric relationships (after Lisowski, 2006) used to calculate surface heave from an embedded spherical source based on an approach by Mogi (1958).

According to the model by Mogi (1958), the vertical displacement  $w$  for a particular point on a free surface  $(x, y, 0)$  can be expressed as:

$$w = \alpha^3 \Delta P \frac{(1 - \nu)}{\mu} \left( \frac{d}{R^3} \right), \quad (4.2)$$

where  $\nu$  is the Poisson's ratio;  $\mu$  the shear modulus of the rock;  $\Delta P$  the pressure change at the spherical source with radius  $\alpha$  (m) located at depth  $d$  (m); and  $R$  the radial distance (m) from the center of the source to a point on the free surface.

The change in volume  $\Delta V$  of the source (due to gypsum crystal growth) approximately relates to the change in pressure as (Mogi, 1958):

$$\Delta V \approx \frac{\Delta P}{\mu} \pi \alpha^3 \quad (4.3)$$

Assuming that each model cell  $c$  of the swelling zone corresponds to a source  $p$  with a change in volume  $\Delta V$ , surface deformation at a particular location  $L_{(x,y)}$  at the ground surface of the model domain and for a specific point in time  $t_p$  of the simulation can be expressed as:

$$w_{(t_p)} = \sum_{t=0}^{t_p} \sum_{p \in c} \left( \Delta V_G(p, t) \frac{(1-v)}{\pi} \right) \frac{d_p}{R^3} \quad (4.4)$$

with  $v$  set to 0.25 (Lisowski, 2006). A Python (version 3.6.6) script was written to implement this relation between volume increase in the swelling zone and heave at the land surface into the model.

#### 4.3.6 Model calibration

The period employed for model calibration started on 3<sup>rd</sup> September 2007 and extended over 2050 days. Initial parameter estimates were taken from the data collected during the site characterization by LGRB (2010, 2012) (hydraulic conductivity, porosity, well properties), and complemented by literature data (hydraulic conductivity, specific storage, mechanical fitting parameter) (Domenico and Mifflin, 1965; LUBW, 2012; Ramon and Alonso, 2013).

The inversion of the reactive transport model was constrained by two types of observation data characterizing the deformation at the ground surface: (1) point observations of the absolute uplift from the geodetic monitoring network within a 30 m buffer around the model transect (total of 1365 points in space and time; see Figure 4.1), and (2) interpolated volumes of the heave body for selected 32 points in time during the first 2050 days of the simulation period. Uplift data were directly compared to the model output along the transect by projecting the measurement points orthogonally onto the transect. The volumetric values were calculated by interpolating the point observation data for each point in time. A detailed description of the calculation of the heave volume from the geodetic data can be found in (Schweizer, Prommer, Blum, Siade, et al., 2018). The heave volume was added as an additional calibration constraint because the observed heave body is characterized by a pronounced anisotropy, which cannot be fully captured along a transect. In addition, piezometric head measurements within the Schilfsandstein (km<sub>2</sub>), Gipskeuper (km<sub>1</sub>), Lettenkeuper (ku) and Upper Muschelkalk (mo) were used to constrain head values of the model. These data were supplemented by head values observed in EKB2 and BB3 during groundwater extraction between  $t = 1311$  and 1631 days of the simulation to constrain the hydraulic impact of the extraction wells.

#### 4.3.7 *Mitigation scenarios*

Based on the actual mitigation measures implemented at the Staufen site, three scenarios were developed and examined to quantify and compare the effect of individual measures on the water availability in the swelling zone, and to predict the heave development at the ground surface. For each mitigation scenario, the amount of water available for the chemical transformation of anhydrite to gypsum was calculated using the reactive transport model, and water budgets were calculated to determine the amount of water entering the swelling zone from different sources.

The first scenario S1 was used as the base scenario. It corresponds to the actually implemented mitigation strategy (LGRB, 2010, 2012) with grouting of the defective boreholes and groundwater draw-down by two extraction wells (EKB2 and BB3, Figure 4.1). All seven grouted BHE were assumed as being completely tight, such that no further water access via the boreholes into the swelling zone occurred or occurs in the future. Averaged pumping rates used in this scenario were based on the data provided by LGRB (2010, 2012). The pumping rates in the periods beyond 2012 are scenarios. Overall, they result in a drawn-down of the piezometric head in the Lettenkeuper and Upper Muschelkalk below the level of the swelling zone. A third well installed in 2015 was not included in the model, as the model only considers countermeasures implemented prior 31<sup>st</sup> December 2012. In scenario S1, it is assumed that pumping continues beyond 1<sup>st</sup> January 2019 at a steady rate until 1<sup>st</sup> January 2025.

Two alternative mitigation scenarios were simulated, both also using the calibrated parameter set employed for scenario S1. Scenario S2 (without pumping) considers a stoppage of pumping after 1<sup>st</sup> January 2019. Scenario S3 (without pumping and seal) considers stoppage of pumping after 1<sup>st</sup> January 2019 and, in addition, the sealing of the geothermal boreholes was assumed to be only partially effective (i.e., water flow via the boreholes is still possible after grouting, albeit at a reduced rate). In all scenarios, the BHE drilling implemented in the model was assumed to be completely tight above the upper gypsum level (UGL, see Figure 4.2), such that water access from above the swelling zone is avoided. An summary of the simulation scenarios is given in Table 4.4.

## 4.4 RESULTS AND DISCUSSION

### 4.4.1 *Calibrated model*

#### 4.4.1.1 *Groundwater flow and reactive transport*

The measured piezometric heads and groundwater drawdown from the extraction wells are generally well reproducible by the model sim-

Table 4.4: Overview of simulated scenarios.

PROPERTY	SCENARIO		
	S1	S2	S3
Description	Base scenario	Without pumping	Without pumping and seal
BHE sealed above UGL	Yes	Yes	Yes
Sealing of BHE successful	Yes	Yes	No
Pumping after 1 <sup>st</sup> January 2019	Yes	No	No
Skin value <sup>a</sup> previous to grouting	$1.0 \times 10^{-4}$	$1.0 \times 10^{-4}$	$1.0 \times 10^{-4}$
Skin value <sup>a</sup> after grouting	$1.0 \times 10^{-10}$	$1.0 \times 10^{-10}$	$1.0 \times 10^{-7}$

<sup>a</sup> value in  $\text{m s}^{-1}$ .

ulations (Figure 4.4). During active pumping periods, residuals between measured and simulated heads at EKB2 and BB3 are 2.74 m and 1.34 m, respectively. The skin values characterizing the hydraulic conductivity of the open well screens of EKB2 and BB3 were estimated at  $1.8 \times 10^{-7} \text{ m s}^{-1}$  and  $3.7 \times 10^{-7} \text{ m s}^{-1}$ , respectively. These values are low compared to literature values between  $3.0 \times 10^{-4} \text{ m s}^{-1}$  and  $3.0 \times 10^{-2} \text{ m s}^{-1}$ ; Domenico and Schwartz, 1997 and may be the result of an overestimated permeability of the aquifers, where the screens are installed. In case of the BHE drilling, the estimated skin value of  $1.0 \times 10^{-4} \text{ m s}^{-1}$  reflects the incomplete backfilling (improper cementation) of the borehole. The hydraulic characteristic value of the faults was estimated at  $6.9 \times 10^{-7} \text{ m}^2 \text{ s}^{-1}$ , therefore leading to an only minor impact of the simulated faults on the groundwater flow patterns.

The calibrated model was used to analyze the hydraulic changes that were caused by the BHE installation and the subsequent mitigation measures. Figure 4.5 shows the impact of the BHE drilling on the groundwater flow patterns, and in particular the flow of water via the drilling into the swelling zone. The water inflow is concentrated on the PFPs of the swelling zone, with high local permeability (Table 4.3: km1f), as indicated by the red arrows in the figure. Water spreads laterally parallel to the geological strata along the PFPs and is thus available for the chemical transformation of anhydrite into gypsum at distances of more than 50 m from the defective BHE drilling.

The implemented mitigation measures (grouting of the defective boreholes and installation of the extraction wells) effectively stopped water inflow into the swelling zone via the BHE in the simulation (Figure 4.6). Groundwater extraction caused a steep hydraulic gradient between the extraction wells and the surrounding aquifer. Groundwater pumping in EKB2 alone (stress periods 2 - 4), however, was

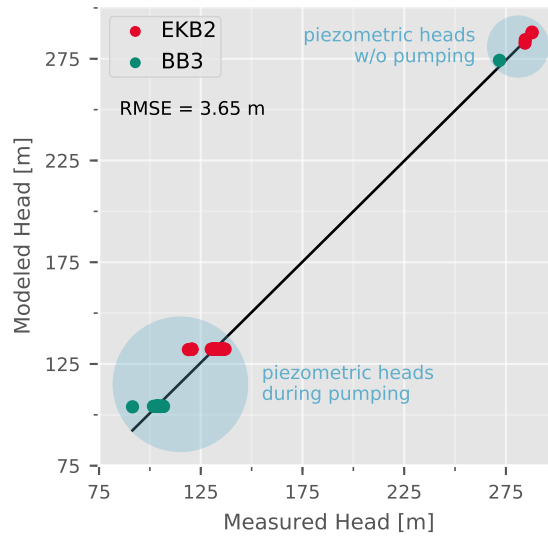


Figure 4.4: Calibration scatter plot showing modeled and measured piezometric heads.

not sufficient to lower the piezometric head below the swelling zone. The piezometric head in proximity of the well's open screen was simulated at 282 m. In contrast, simulated heads for the ku and mo aquifer in proximity of the BHE remained as high as 287 m and thus, above the piezometric head in the swelling zone (283 m). Thus, in our simulation the observed decrease of water inflow into the swelling zone can be attributed to the grouting of the defective boreholes. The combined groundwater extraction in both wells (stress periods 5 - 7), however, effectively lowered the piezometric head in proximity of the BHE (271 m) below the piezometric head of the swelling zone. In this case, the applied mitigation measures are effectively redundant: Grouting and pumping both prevent water inflow into the swelling zone. With respect to pumping, the results illustrate that an adequate planning of the groundwater extraction (with respect to the number, location and pumping rates of the wells) is crucial for a successful mitigation of the swelling problem.

The calibrated reactive transport model quantified the chemical transformation of anhydrite to gypsum in the swelling zone. The simulations show in particular the effect of the mitigation measures on the availability of the ingressed water and the rate of gypsum crystal growth (Figure 4.7). The mitigation measures (grouting of the defective BHE drilling and pumping in both wells) effectively reduced the content of ingressed water in the mobile domain of the swelling zone, which dropped from 58 to 8% (Figure 4.7 top). The overall rate of gypsum crystal growth was therefore reduced by 86% from 1.18 to 0.17 mol d<sup>-1</sup> (Figure 4.7 bottom). At the end of the calibration period (14<sup>th</sup> April 2013), only about 1% of the anhydrite in the swelling zone

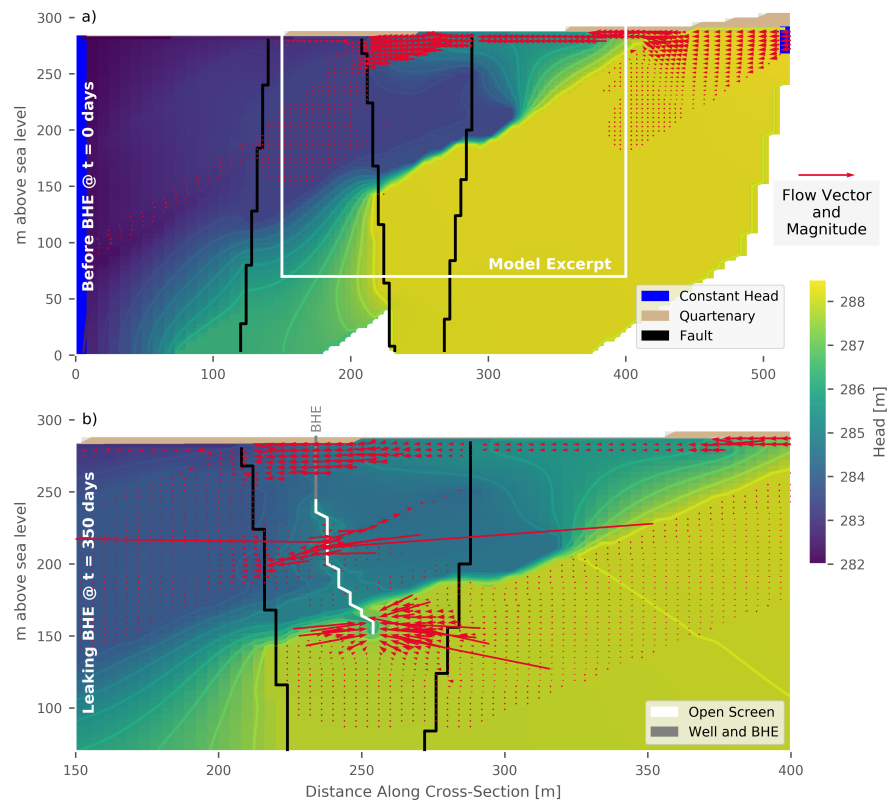


Figure 4.5: Hydraulic head distribution (a) before and (b) after the installation of the BHE drilling. (b) shows a magnified extract of the model domain. The red arrows, indicating flow direction and magnitude, show high water inflow from the Lettenkeuper and Muschelkalk aquifers into the defect BHE drilling at the bottom and high water outflow from the drilling into the swelling zone in the central part of the drilling.

was converted into gypsum. This suggests that there is still a large potential for future swelling upon further contact with water.

#### 4.4.1.2 Simulated heave

Simulated and measured (i.e., interpolated from heave measurements) volumes of the heave body at the ground surface are in good agreement, with an average residual of  $310\text{ m}^3$  for all 32 points in time being compared (Figure 4.8a). However, while the general heave dynamics (i.e., trend of dying-out after the mitigation measures) are well captured by the model, results also show two distinct characteristic deviations. First, maximum uplift and the heave rate along the model transect are systematically underestimated by the model and remain below the observation values from the geodetic monitoring (Figure 4.8b and 4.8c). The maximum simulated uplift amounts only to 0.30 m, compared to measured 0.54 m at the end of the calibration period ( $t = 2050$ ). Secondly, the lateral offset between the simulated

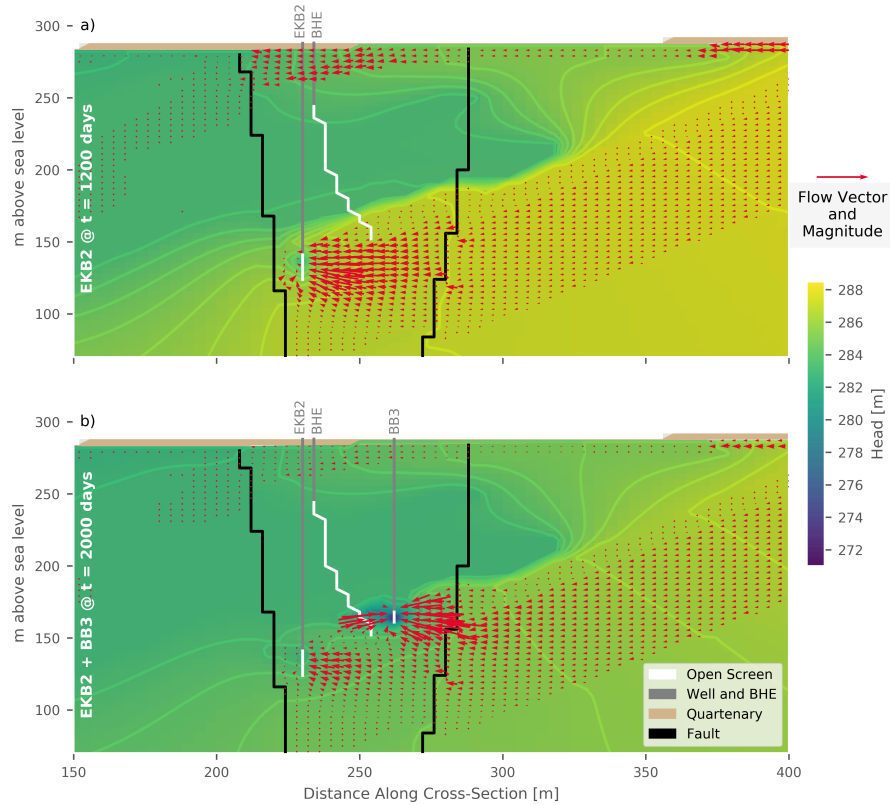


Figure 4.6: Hydraulic head distribution after implementation of mitigation measures with grouting of the defective BHE drilling and (a) pumping only in EKB2; (b) pumping both in EKB2 and BB3. In a), the piezometric head at the lower end of the BHE is still above the level of the swelling zone. Only successful grouting prevents water inflow into the swelling zone via the BHE. In b), water inflow into the swelling zone is prevented both by grouting and by drawdown of the piezometric head in the aquifers under the swelling zone.

and measured uplift maximum at the ground surface (center of heave) approximates to 35 m along the model transect (Figure 4.8d).

These deviations are due to the propagation of volume increase in the subsurface to the ground surface using the model by Mogi (1958). It assumes isotropic and homogenous conditions, while at the study site the geological strata are steeply inclined with large displacements along faults. Although the complex geological setting is well considered in the flow and reactive transport model to simulate the processes being effective in the swelling zone, the mechanical response of the swelling zone's overburden is strongly simplified. Moreover, no feedback mechanisms between hydraulic, chemical and mechanical processes are implemented in the model. For example, the volume change in the swelling zone due to gypsum crystal growth has neither an effect on the permeability, nor on the reactive mineral surfaces. As a result the shape of the simulated heave body does not closely repre-

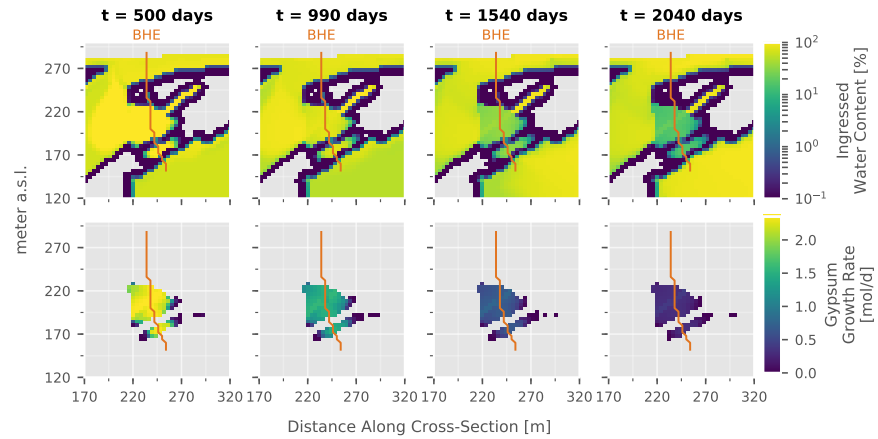


Figure 4.7: Top: Simulated content of ingressed water, illustrating the decrease in water content available for the transformation of anhydrite into gypsum in the swelling zone due to the mitigation measures. Bottom: Rate of gypsum crystal growth in the swelling zone. As an effect of the mitigation measures, the formation of gypsum (and hence swelling) is strongly reduced.

sent the observed shape, i.e., the maximum heave is underestimated and the heave is too dispersed (Figure 4.9), whereas simulated and observed heave body volumes are in good agreement (Figure 4.8a).

An attempt of geomechanical modeling of the heave at the Staufen site was undertaken by Benz and Wehnert (2012) using a finite-element numerical model. Their constitutive model, which was based on Grob's swelling law (Grob, 1972; Schädlich et al., 2013), was able to reproduce the observed swelling behavior while considering the mechanical response of the overburden. However, the maximum applied swelling stress ( $\sigma_0 = 9$  MPa) represents the upper limit of empirical values in clay-sulfate rocks (Steiner, 1993) and no chemical or hydrogeological processes were considered. In addition, it remains unclear whether Grob's swelling law is indeed applicable to anhydrite-clay swelling (Butscher, Breuer, et al., 2018).

Finally, a possible further reason for the differences between the modeled and observed geometry of the heave body in the present study might be the unknown lateral extent of the swelling zone, which in the model depends on the geometry of PFPs and the zonation of the Gipskeuper. These features are well constrained by the exploration boreholes regarding depth, but not regarding their lateral extent.

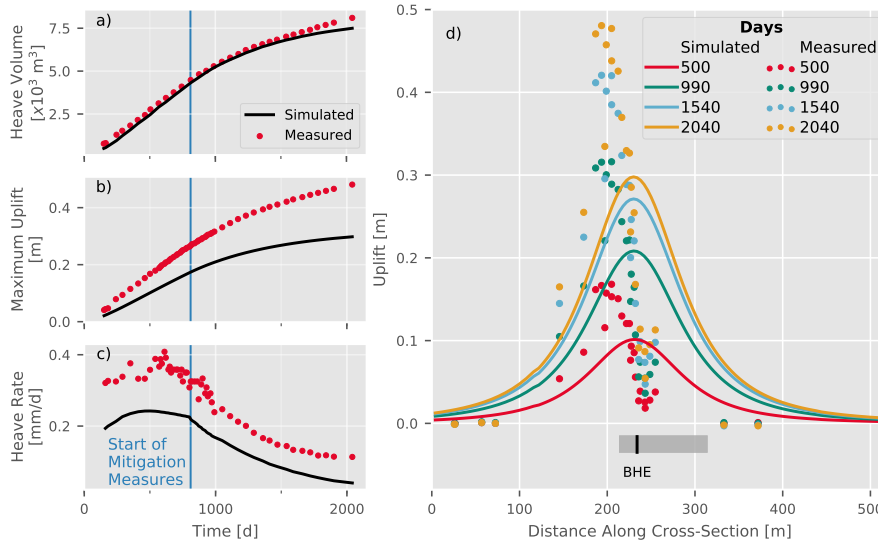


Figure 4.8: Left: Simulated and measured heave volume at the ground surface, maximum uplift and heave rate. Right: Projected uplift at the ground surface for four representative points in time during the calibration period. The grey box at the bottom represents the lateral extent of the swelling zone in the subsurface.

#### 4.4.2 Assessment of mitigation measures

##### 4.4.2.1 Water flow into the swelling zone

A strength of the developed model is its ability to simulate the processes responsible for water inflow from different sources into the swelling zone, including the hydraulic effects of human activities such as the BHE drillings and mitigation measures, and to evaluate the water availability for the chemical transformation of anhydrite into gypsum under changing hydraulic boundary conditions. In order to determine the amount and origin of water entering the swelling zone and to evaluate the hydraulic impact of all simulated scenarios in more detail, water budgets were calculated for defined phases of the overall model simulation period (Figures 4.10 and 4.11). Three sources and sinks of water were distinguished: 1) the BHE drilling, 2) the Gipskeuper strata without anhydrite surrounding the swelling zone (Zone 2), and 3) all other strata of the model domain (Zone 3). The water budget calculations show that flow rates into the swelling zone were as low as  $0.49 \text{ m}^3 \text{ d}^{-1}$  before the geothermal drillings, while afterwards, they dramatically increased to  $57 \text{ m}^3 \text{ d}^{-1}$  (Figure 4.10). In comparison, Schweizer, Prommer, Blum, Siade, et al. (2018) estimated a value of  $25 \text{ m}^3 \text{ d}^{-1}$  after the drillings for the strongly simplified case of this previous study. The significantly higher inflow rate in the present study illustrates the large impact of considering hydrogeological conditions in more detail.

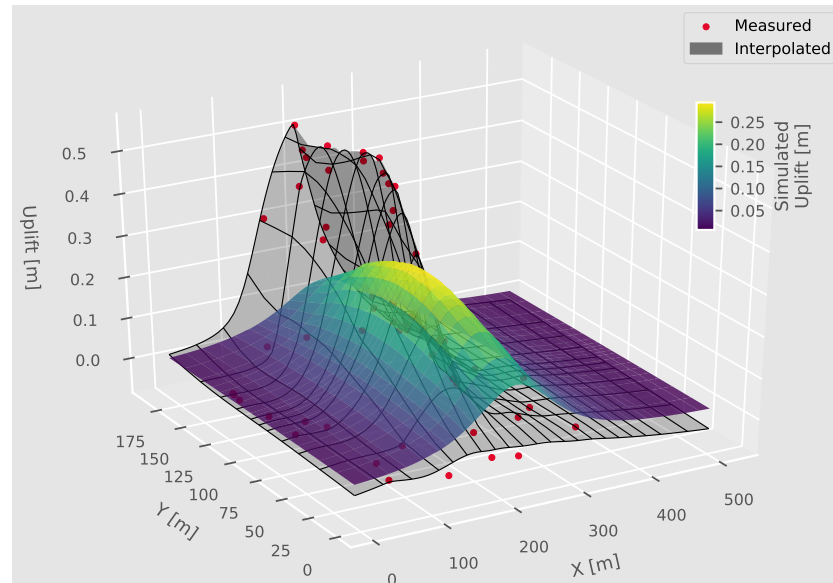


Figure 4.9: 3D view of simulated and observed heave body ( $t = 2050$  days). The projection of the simulated volume increase in the swelling zone onto the land surface results in a lower but wider heave body compared to observed heave, and a shift of the heave center.

After the start of the mitigation measures ( $t > 840$  days), water inflow into the swelling zone via the BHE immediately decreases to zero, and original hydraulic conditions were restored in scenarios S1 and S2 (Figure 4.11). Scenario S2 also indicates that water access to the swelling zone is still prevented after stopping pumping on 1<sup>st</sup> January 2019 ( $t > 4140$  days). This underpins that the sealing of the BHE has superimposed the mitigation through pumping and indicates that a successful sealing of the BHE through grouting is sufficient to stop swelling under the given model assumptions.

Scenario S3 accounts for situations where it is not possible to effectively seal all BHE. This may be the case at the Staufen site, where one of the BHE has collapsed at the bottom (below 105 m) during installation and could therefore not be grouted (LGRB, 2012). In this scenario, water inflow via the BHE continues throughout the simulation period and thus, swelling never completely stops. However, pumping has a significant effect on the water availability and strongly reduces water flow into the swelling zone (and thus swelling). In particular, the extraction well BB3 proved to be well placed and effective, maintaining an inflow rate into the swelling zone via the BHE as low as  $0.41 \text{ m}^3 \text{ d}^{-1}$ . The effectiveness of this mitigation measure becomes especially apparent once pumping is stopped in this scenario ( $t > 4140$  days): inflow rates immediately rise back to  $1.83 \text{ m}^3 \text{ d}^{-1}$ , and consequently the amount of water available for swelling increases again.

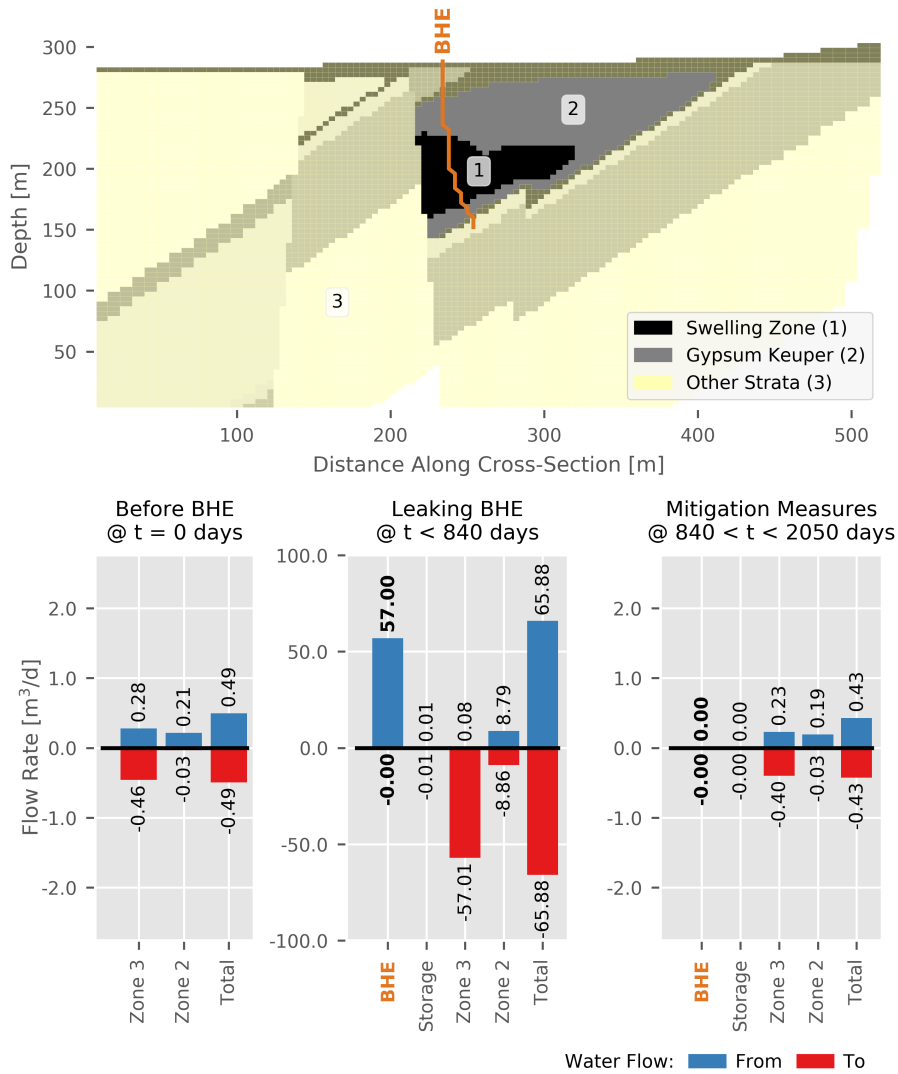


Figure 4.10: Top: Subdivision of the model domain into three distinct zones to evaluate sources and sinks of water available for the transformation of anhydrite into gypsum in the swelling zone. Bottom: Water budgets of the swelling zone calculated for the scenario S<sub>1</sub> before (left) and after the BHE drillings (middle), and after the implementation of the mitigation measures (right). The calculated water budgets show water inflow into the swelling zone via the defective geothermal drillings and the successful stop of water inflow after mitigation. Note the different scales of the axes of ordinates.

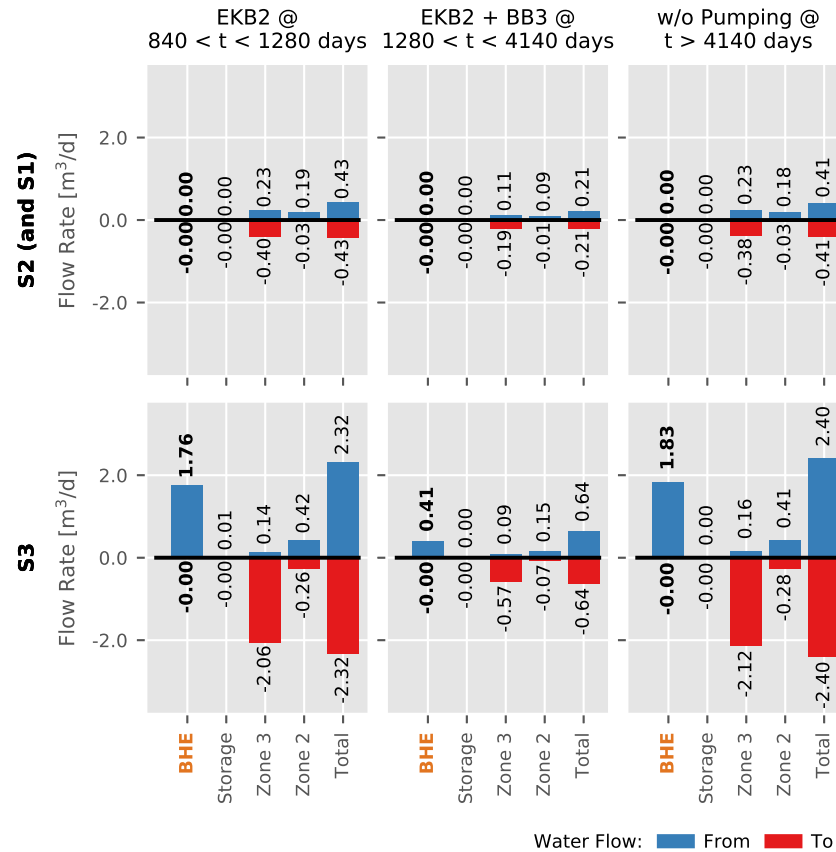


Figure 4.11: Water budgets of the swelling zone for scenario S2 (top) and scenario S3 (bottom) after the start of the mitigation measures. While mitigation measures can be successfully assessed for scenario S2 (independent of the pumping measures), the mitigation success for scenario S3 depends on the pumping activity. Only pumping in both wells (EKB2 and BB3) effectively prevents water inflow into the swelling zone.

This illustrates that in case of incomplete sealing of the BHE, adequate groundwater extraction measures are of paramount importance for the mitigation success. The planning of groundwater drawdown by extraction wells requires not only an adequate dimensioning of the well (in terms of pumping rates), but also careful selection of the well location. Scenario S3 also suggests that additional measures are required to completely stop the swelling. At the study site, such additional measures were implemented through the installation of a third extraction well in 2015.

#### 4.4.2.2 Prediction of uplift

The progress of uplift was calculated for all three scenarios and compared to the measured uplift. Just as in the simulations with the calibrated model (see section 4.4.1.2), the simulated maximum uplifts

of all scenarios remain below the observed values. In scenarios S<sub>1</sub> and S<sub>2</sub>, uplift ceases completely after approximately 3500 days (Figure 4.12a), and the total amount of available ingressed water drops to zero (Figure 4.12b). Consequently, both scenarios predict a successful mitigation. Moreover, scenario S<sub>2</sub> suggests that no further pumping is required to stop the swelling if the BHE is completely sealed. In contrast, S<sub>3</sub> shows a continued uplift at a low but steady rate after implementation of the mitigation measures. Uplift even increases again when pumping stops from 1<sup>st</sup> January 2019 onward. In the coming six years (until 2025), about 10 cm of additional heave is predicted by the model for this scenario. This again suggests that the continued pumping is crucial for mitigation success where a complete sealing of the BHE was not achieved. In such cases the further progress of the uplift strongly depends on the remaining permeability of the incompletely sealed BHE, but also on the hydraulic properties of the aquifers and the swelling zone.

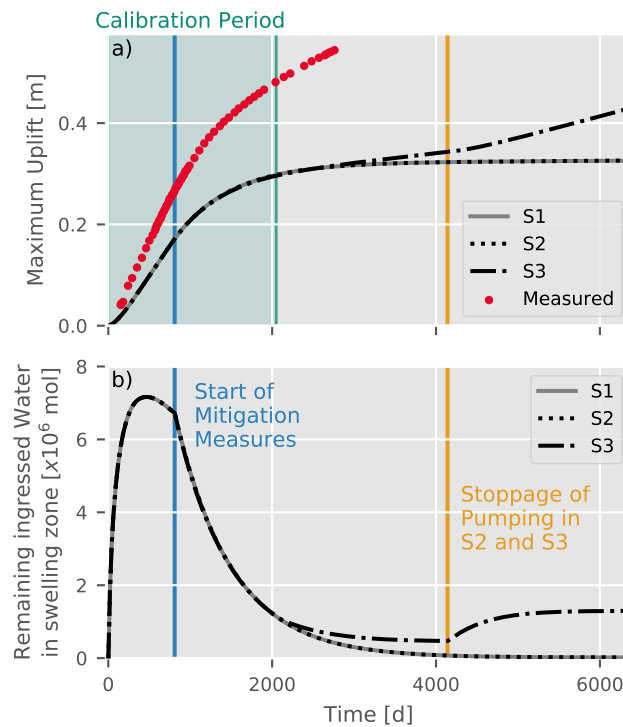


Figure 4.12: Maximum uplift at the ground surface (top) and water availability in the swelling zone (bottom) for the three simulated scenarios. Scenarios S<sub>1</sub> and S<sub>2</sub> show successful mitigation measures that stop the swelling. Scenario S<sub>3</sub> with still incompletely sealed BHE suggests reduced but continuing swelling after the mitigation measures.

#### 4.4.2.3 Transferability and application

The presented countermeasures are also applicable to other, similar cases of damage in connection with BHE drillings, where the ingress of water into a swelling zone is due to a hydraulic short circuit. In general, the response to the implemented measures is almost instantaneous and reflected in a reduction in heave at the ground surface (Figure 4.13). Thus, it can be quickly determined, whether the measures were effective in stopping water from accessing the swelling zone and feeding the chemical transformation of anhydrite to gypsum. For example, the sealing of BHE drillings successfully reduced uplift rates at two separate sites in Böblingen, Germany (LGRB, 2015), with measurable effects immediately after implementation (Figure 4.13b). However, while countermeasures ultimately led to a decline in uplift rates from 5.5 and 2.9 mm month<sup>-1</sup>, respectively, to almost zero (Anderssohn, 2015), long time series of measurements are required to evaluate the further course of swelling and whether additional countermeasures are needed. Hence, for an effective and timely planning of feasible countermeasures, a comprehensive understanding of the swelling process, underpinned by predictive models are crucial.

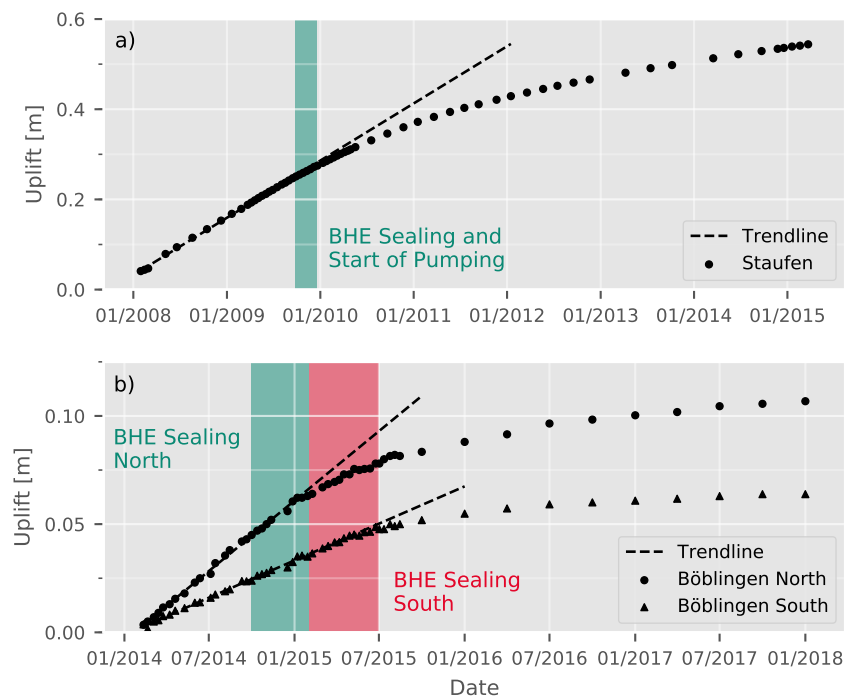


Figure 4.13: Effect of hydraulic countermeasures on the development of the uplift at the ground surface at sites located in the city of a) Staufen and b) Böblingen (data extracted from LGRB (2015) and information available at <https://www.erdhebungen-bb.de/start/Newsletter/Archiv.html>).

#### 4.5 CONCLUSION

The overall aim of this study was to further refine our understanding and predictions of the effects that various mitigation measures may have on the progress of swelling in clay-sulfate rocks. To achieve this we successfully applied our earlier developed numerical approach to the complex geological setting of the study site. Our results demonstrate that the model is generally capable of reproducing the swelling-induced ground heave in Staufen and can be used to estimate its future course. Thus, the presented and well-established approach (reactive transport modeling) shows to be a viable tool for planning measures that counteract the swelling of clay-sulfate rocks in GSHP damage cases and other engineering activities, such as tunneling, road and bridge construction.

The study highlights the importance of adequate geological, hydraulic and geochemical site information including the hydraulic properties of PFPs and the BHE drilling to assess the swelling potential. By localizing and quantifying water fluxes into the swelling zone and the geochemical processes taking place therein, the presented approach allows for the identification and improved evaluation of measures to counteract the swelling problem. For example, our model-based analysis of three different mitigation scenarios suggests that even in case of incomplete BHE sealing, water flow into the swelling zone can be stopped at the study site by appropriate pumping. However, the projection of the swelling-induced volume increase in the subsurface to the ground surface by means of a simplifying analytical model appears to lead to an inaccurate prediction of the shape of the heave body. Coupling of the presented hydro-chemical model with a mechanical model may further improve the accuracy of the model results, which should be attempted in future work. In addition, other indicators such as the temperature signal of the exothermic chemical reaction of anhydrite to gypsum could be used in the future to optimize the calibration and parameterization of the model and to increase its predictive accuracy.

#### 4.6 ACKNOWLEDGMENTS

Financial support for D. Schweizer from the German Research Foundation (DFG) under grant number BU 2993/2-1 and from the Graduate School for Climate and Environment (GRACE) is gratefully acknowledged. We thank the Geological Survey of Baden-Wuerttemberg (LGRB), especially Dr. Gunther Wirsing and Dr. Clemens Ruch, for the provision of digital data.



## Part V

### SYNTHESIS AND DISCUSSION

In this part I summarize the key findings I obtained in the individual studies with respect to the research objectives stated in the introduction. I further discuss aspects important to the overall modeling approach, and I propose opportunities for future research.



SYNTHESIS AND DISCUSSION

---

## 5.1 SUMMARY

Predicting the swelling of clay-sulfate rocks requires a thorough understanding of the underlying processes and controls, with numerical models playing a key role. Hence, the two overarching goals of modeling in this thesis are to improve the *ability to predict* and to gain a *comprehensive understanding* of the system under consideration. The individual studies in Chapter 2 to 4 are each devoted to a partial aspect of these two goals and are briefly summarized below with regard to their contribution.

In the first study, an adequate 3D geological model, considering the geological framework at the study site was developed, which is used as a basis for the numerical modeling in the further course of the thesis. Essentially, the prevailing geological conditions strongly influence the flow of groundwater and determine the characteristics of the swelling zone. However, geological site models are rarely challenged as precursors to numerical models. Due to the high structural complexity of the subsurface at the study site Staufen and ambiguity in the sparse and noisy data available, a unique representation of the subsurface structure is not feasible (under-determined problem). Applying the concept of information entropy, uncertainties in subsurface structures are quantified and visualized, thus providing the basis for a better understanding of the underlying causes of uncertainty and a systematic approach to compare different model interpretations. The results show that uncertainties persist in the 3D geological model, even if all available geological data are taken into account. It becomes apparent that the distribution of uncertainties in the 3D geological model depends on the actual identified subsurface structures (e.g., faults and folds), which in turn vary widely with the geological data available. It is shown that parsimonious models may underestimate uncertainty locally, highlighting the need for adequate consideration of structural uncertainties in site investigation. Therefore, of the four individual 3D geological model interpretations that have been developed, only the most sophisticated model with the lowest average entropy (i.e. the minimum total uncertainty) is used as the geometric basis of the numerical models in this thesis. The 3D geological model integrates the available geological information at the study site, thereby delimiting the location of geological formations, major aquifers and geological structures relevant to the swelling phenomenon. Overall, the presented approach makes it pos-

sible to systematically minimize structural uncertainties during the data collection phase and to subsequently adapt/re-evaluate model interpretations through newly available data and insights. Thus, it can also be a useful tool during ongoing site investigations to improve the efficiency of exploration campaigns and provide a basis for cost-benefit analysis.

The second study makes use of the extensive and detailed datasets available for the study site, which include hydrogeological, geochemical and geomechanical data as well as geodetic measurements to monitor ground heave. Based on this data, a novel conceptual and numerical modeling approach is proposed to gain a better understanding of the swelling process in clay-sulfate rock and take a step towards predicting its evolution in space and time. The developed modeling approach, which focuses on a reactive transport model, aims at the quantification of swelling-induced heave at the ground surface as a function of the reaction kinetics of anhydrite and gypsum as well as the availability of water in the system. Overall, the inversion process results in a plausible model (i.e., parameterization is largely consistent with literature values and measurements on site) that simulates swelling-induced heave in accordance with geodetic measurement. The model results show that the exchange of water and solutes between preferential flow paths and the rock matrix greatly affects the intensity and spatial extent of the simulated swelling processes. The diffusive transport into the rock matrix essentially determines the effective rate of the anhydrite dissolution and is therefore a decisive factor for the chemical transformation of anhydrite into gypsum and the swelling process. Most notably, diffusion-limited swelling is relevant for rocks with low permeability, for example for compact anhydrite layers. In addition, the model results emphasize the importance of assessing the reactive surface area when it comes to determining reaction kinetics of the minerals and the intensity of the swelling process. The presented approach uses the initial mineral content (volume fraction) and the porosity of the matrix (i.e. the water volume in contact with the solid phase) as parameters in the inversion process, providing a straight forward implementation of the specific surface area. The estimated reaction rate constants for anhydrite dissolution ( $k_A = 2.4 \times 10^{-5} \text{ mol m}^{-2} \text{ s}^{-1}$ ) and gypsum precipitation ( $k_G = 3.2 \times 10^{-6} \text{ mol m}^{-2} \text{ s}^{-1}$ ) are in good agreement with literature values from laboratory experiments. Thus, they are suitable for describing observed swelling rates and the simulation results also suggest their transferability to the field scale. Further identifiable parameters include the hydraulic conductivity, the flow rate and the mass transfer rate with values of  $2.9 \times 10^{-4} \text{ m}^3 \text{ s}^{-1}$ ,  $3.5 \times 10^{-7} \text{ m s}^{-1}$  and  $2.4 \times 10^{-10} \text{ s}^{-1}$ , respectively. Thus, the model provides important information about the hydraulic controls of the swelling process, which are often difficult to assess during incidents with swelling clay-sulfate

rocks. However, although parameters are generally well informed by the observation data, the conducted uncertainty analysis also indicates that, in particular, geochemical parameters may not be reliably determined by the model because of their low identifiability and sensitivity. In light of this, observation data more specifically constraining the geochemical model parameters may be added to improve the solution of the inverse problem and thus, the representation of the geochemical processes in the model. Nonetheless, the proposed modeling approach provides a promising and easy-to-implement approach for the simulation of the swelling process and swelling-induced heave at the field scale, which can be easily expanded and built upon. Last but not least, the results of the study ultimately contribute to a better understanding of the controls of the swelling mechanisms and the thereby occurring processes in clay-sulfate rocks.

The third study focuses on the aspect of prediction by investigating the future course of the swelling phenomenon at the study site using different simulation scenarios. By combining the findings and results of the previous two studies, the developed numerical modeling approach to describe the hydrogeological and geochemical processes of the swelling phenomenon is successfully applied to the complex geological situation in Staufen. The model is able to capture the observed swelling process, and the evolution of the swelling-induced heave in space and time can be estimated. However, the physical representation of the swelling-induced heave process due to the increase in volume of a spherical source embedded in an isotropic elastic half-space leads to a partially inaccurate representation of the observed heave body. Despite these limitations, the otherwise refined model allows the simulation of different causes of water flow into the source zone, taking into account human activities such as BHE drilling and mitigation measures and their hydraulic effects. Thus, the approach can be used to quantify, visualize and predict water access to, and availability for the chemical transformation of anhydrite into gypsum in the swelling zone, under changing hydraulic boundary conditions. The model results show that the water spreads rapidly along the preferred flow paths parallel to the geological strata, expanding the swelling zone to 50 meters from the source of water inflow (i.e. the defective BHE drilling). Furthermore, the efficiencies of various hydraulic measures, particularly for GSHP systems, can be analyzed in detail comparing different mitigation scenarios. For example, analysis of three different mitigation scenario simulations for the study site indicates that continued pumping can stop water access to the swelling zone, even if a complete sealing (i.e. grouting) of the BHE is not guaranteed. The practical applicability of hydraulic countermeasures is underpinned by the successful implementation in connection with similar incidents involving clay-sulfate swelling. The findings of

this study provide an improved scientific basis and tool for the planning of mitigation strategies meeting the swelling problem. They are relevant to GSHP damage cases and to other engineering activities, such as tunneling, road and bridge construction, ultimately bridging the gap between a basic understanding of the swelling phenomenon and application-oriented questions.

## 5.2 DISCUSSION AND OUTLOOK

At the heart of this thesis lies the development of a conceptual model and the application of a reactive transport model approach to investigate the phenomenon of swelling and its hydrogeological and geochemical processes on a large spatial scale. In doing so, I applied various approaches to uncertainty assessment, parameter estimation and consideration of coupled processes. Uncertainty assessment was relevant to the development of a 3D geological model and the consideration of ambiguities in the geological data. It was also required in determining parameter uncertainties and model identifiability of the reactive transport model. Parameter estimation was imperative for the estimation of the reaction kinetics of the swelling process as well as key hydraulic and mass transport properties of the swelling zone. Process-based, coupled modeling was essential in relating the evolution of the swelling process to the multi-scale effects of changing hydraulic conditions and to their interaction with geochemical processes. The latter facilitated an application-oriented assessment of hydraulic mitigation measures to counteract the swelling process. Through these approaches, I was able to address the objectives outlined in Chapter 1.2 and thus make a significant contribution to understanding the swelling process. At the same time, opportunities for further research opened up during the investigation, not all of which could be pursued, while some aspects considered could benefit from further research. In the following I address noteworthy issues related to the consideration of coupled processes and the assessment of uncertainties. In the latter case, I mainly focus on geological models. Last but not least, I further elaborate on potential for future research and opportunities to expand on the presented approaches.

### *Assessment of geological uncertainty and its relevance to the swelling phenomenon*

In order to establish a comprehensive structural geological 3D model, the required geological information, particularly in the case of a complex geological setting, can be extensive. However, data are usually sparse, inaccurate, of varying quality and their interpretation is often ambiguous. Hence, geological models contain significant uncertainty (Caers, 2011; Lark et al., 2013; Wellmann, Horowitz, et al., 2010) that

needs to be addressed in order to have confidence in the validity of the model (Jessell, Pakyuz-charrier, et al., 2018).

The uncertainty assessment workflow which I presented in Chapter 2 (Figure 2.4) accounts for structural uncertainty by perturbing geological structures (faults and horizons) either based on alternative surface interpretations or according to an assigned probability distribution to generating multiple model realization. Although some of the structural uncertainties could thus be identified, there is still limited consideration of the uncertainty of the input parameters and data (geometric, geophysical, or model-specific). This is partly due to the implicit modeling engine used in the geological modeling workflow, which is tailored for mineral exploration and has limited functionality to assess uncertainty.

Alternative approaches to understanding uncertainty, specifically in conjunction with the the potential-field interpolation method, generate multiple model realizations by manipulating the model-specific parameters themselves, such as parameters related to the cokriging algorithm (Aug et al., 2005; Chilès et al., 2004). In addition, Monte Carlo methods have been introduced to geological modeling for the purpose of characterizing uncertainty, which exploit the ability of implicit modeling methods to automate geological modeling steps from stochastic parameters and their probability functions (Jessell, Ailleres, et al., 2010; Lindsay, Aillères, et al., 2012; Pakyuz-Charrier et al., 2018; Wellmann, Horowitz, et al., 2010). Adapting the workflow to these approaches could considerably improve the assessment and mitigation of uncertainty while enabling input data uncertainty propagation all through the process of implicit geological modeling.

A suitable and advanced open-source implementation of an implicit geological modeling method based on a potential-field approach and with emphasis on uncertainty analysis has recently become available through *GemPy* (De La Varga et al., 2019). It offers transparency, allows manipulation of the underlying algorithms and enables stochastic geological modeling and inversions for advanced scientific investigations. Thus, it provides a promising opportunity that could be used in future research to better determine the impact of geological conditions on the swelling phenomenon and possibly extend the probabilistic approach to the numerical model and the inversion of the swelling process. Ultimately, this will improve the basis for further analysis and prediction of the swelling process, as uncertainties regarding, for example, the extent and location of the swelling zone are better taken into consideration.

#### *The importance of preferential flow paths to the swelling process*

Regardless of the geological modeling methodology used, the numerical modeling approach to groundwater flow simulations with *MOD-*

*FLOW* (Harbaugh, 2005; Harbaugh et al., 2017) has some limitations that complicate a comprehensive and automated consideration of a complex 3D geological model and thus, requires cumbersome manual editing steps of the model domain. As a result, important geological information from the original 3D geological model is lost. The quasi-3D model used in the final case study of Chapter 4 is a compromise between a sufficiently complex and yet efficient representation of the available geological information, which may not fully reflect the conditions relevant to the swelling process. For instance, the structured, rectilinear grid of the underlying finite difference numerical method in *MODFLOW* is not suited for an adequate implementation of structures characteristic to hard-rock, such as discrete fracture networks or faults in connection with large displacements and steeply inclined layers.

However, flow processes along preferential flow paths (e.g. fractures, faults or a near-wellbore damage zone) may play a major role in the access of groundwater to the swelling zone. Faults in particular can act as barriers to groundwater flow, but they can also contain highly fractured zones of increased permeability parallel to the faults orientation (Caine et al., 1996), that provide a link between aquifers and the swelling zone (Butscher, Einstein, et al., 2011; Butscher, Huggenberger, and Zechner, 2011). The implementation of discrete fractures as PFPs in the swelling zone was circumvented by a dual-domain approach used in this thesis. It assumes that PFPs are static (i.e. with a predefined location at the start of the simulation) and homogeneously distributed in the swelling zone, although their distribution and properties may vary over space and time.

In order to better implement these structures in the flow and transport model, methods for mesh adaptation and flexible discretization as well as options to include time-varying geometries are required to enable an accurate spatial representation of the geology. But even more importantly, an interface with the implicit geological modeling method is required, that allows for automated transfer of geometries to the numerical model. While an unstructured grid method is provided with *MODFLOW-USG*, compatibility with *Phl3D* (Prommer et al., 2003) is still missing. On the other hand, an interface for automation may be provided through Python as the common platform of both *GemPy* (De La Varga et al., 2019) and *FloPy* (Bakker et al., 2016). In contrast, groundwater models based on the finite element method, such as *FEFLOW*, generally allows for a highly flexible meshing strategy and thus, could be more suitable to simulate water access to the swelling zone along faults, as was shown by Butscher, Huggenberger, and Zechner (2011) and Butscher, Huggenberger, Zechner, and Einstein (2011). Together with the *PhreeqcRM* (Parkhurst and Wissmeier, 2015) reaction model to perform equilibrium and kinetic reaction calculations for reactive transport, it may even present an alternative ap-

proach to investigate the hydrogeological and geochemical processes of the swelling phenomenon.

In any case, future research should expand on the presented approach by facilitating consideration of discrete PFPs, because they may enable large-scale water access to otherwise almost impermeable anhydrite layers. And since the availability of water, in turn, determines the swelling process, considering all possible flow paths for water access to the swelling zone is crucial to ultimately gain a comprehensive understanding of the system.

*Considering coupled processes in swelling clay-sulfate rocks*

Finally, one major limitation of the presented modeling approach to simulate hydrogeological and geochemical processes involved in the swelling of clay-sulfate rocks lies in the sequential processing and execution of the flow, transport/chemical and mechanical models. Feedback between physical processes is limited and mostly unidirectional (flow  $\rightarrow$  transport/chemistry  $\rightarrow$  mechanics), therefore some processes and controls remain uncaptured. In fact, a number of mutual interactions exists that must be simultaneously taken into account in analyses. For example, the impact of mechanical stress from gypsum crystal growth on flow and transport simulations is not considered in the model, but likely crucial to the evolution of the swelling process. Full consideration would require updating of properties such as permeability, mobile and immobile porosity or the mass transfer rate at each time step of the simulation. This type of feedback is not accounted for in the code of *Pht3D*, mostly because it is tailored towards the simulation of reactive transport problems (e.g., contaminant transport), which usually do not require coupling with a mechanical model. For this reason, swelling-induced heave was calculated separately in a post-processing step, using volumetric changes due to gypsum precipitation rather than the induced mechanical stress. Hence, full coupling with a mechanical model, although challenging, is the next logical step in model development to better account for the mutual interactions of the physical processes in the subsurface and link them to the observed swelling-induced heave at the ground surface. Especially the latter may greatly improve the conditions of the inverse problem. In addition, a mechanical model is needed to explicitly consider the effects of “clay swelling” on the rock matrix and thus, the (long-term) evolution of the swelling process and the dynamics of the system.

On the other hand, due to the mathematical similarities between heat and mass transport, the presented approach can readily be extended by a thermal model using the *Pht3D* code (Hecht-Méndez et al., 2010). A thermal model could account for the effects of temperature change on the water activity and the equilibrium concentration

of minerals (Serafeimidis and Anagnostou, 2014b), triggered by the exothermic chemical reaction of anhydrite to gypsum itself or the inflow of water from aquifers outside the swelling zone. Furthermore, the thermal model could be used to simulate the temperature signal of the exothermic reaction and thus, optimize the calibration and parameterization of the model, increasing its predictive accuracy.

However, computational costs for simulation and model calibration in this thesis are already relatively high, with run times of up to three days to complete a single model run on a standard PC. The run time sums up to a few weeks for several model runs required for the parameter estimation in the studies of Chapter 3 and 4. Nevertheless, there is still huge potential for improving computational performance through parallelization. This would be a prerequisite for any major model extension, including a thermal or mechanical model, or a more detailed and complete 3D model representation. Other approaches to the simulation of the swelling processes include coupled hydro-mechanical-chemical (HMC) analysis (Oldecop and Alonso, 2012; Ramon and Alonso, 2013, 2018; Ramon, Alonso, and Olivella, 2017) and offer parallelization (e.g. the finite element code *Code\_Bright*, Olivella, Gens, et al., 1996). However, they are not as versatile as a reactive transport model either in their consideration of the actual hydrogeological and geochemical conditions at the field scale or in modeling the effects of groundwater inflow on geochemical conditions. In addition, all the approaches described here have in common that they can be difficult to customize and expand without extensive programming skills. A promising alternative in this regard may be presented by MOOSE (Multiphysics Object Oriented Simulation Environment), a finite element framework that allows straight forward modular development and coupling of physical processes as “kernels” with automatic parallelization and built-in mesh adaptation.

Ultimately, future research should focus on developing a comprehensive modeling approach for the swelling phenomenon that couples hydraulic, chemical, mechanical and thermal processes, and that can easily be extended by new physical processes, without the need for post-processing or different modeling frameworks. In particular, given the diverse interactions of physical processes and the non-linearity of the system, it is to be expected that substantial model adaptations are still needed to improve the *ability to predict* and to gain a *comprehensive understanding* of the swelling phenomenon.

## Part VI

### APPENDIX

The content of [A.1](#) and [A.2](#) has been published in *Solid Earth and Water Resources Research* as supporting information to the studies presented in Part II and III.



## APPENDIX

## A.1 APPENDIX OF PART II

A.1.1 *Structural uncertainty workflow parameters*

The Structural Uncertainty workflow of SKUA requires a set of parameters and input modes to be defined by the modeler.

For each fault, three different input modes were available: 1) constant symmetry, 2) move with others (MWO) and 3) fixed. A maximum displacement and probability distribution was assigned when available for the input mode. Minor faults and those indirectly constrained by surrounding faults or boreholes were set to “move with others”. All other faults were set to constant symmetry. Maximum displacement values are either averaged by combining multiple sources (gk1, gk4, tec3) or by an “educated guess” by the authors. To allow for a realistic distribution of realizations around our average estimate we chose a Gaussian distribution in all cases. A summary of all used fault parameter settings is shown in Table A.1.

Table A.1: Fault parameter settings used in the Structural Uncertainty Workflow of SKUA.

FAULT	INPUT MODE	MAXIMUM DISPLACEMENT [M]	DISTRIBUTION	MODEL
gk1	constant symmetry	45	Gaussian	1,2,3,4
gk3	MWO	NA	NA	1,2,3,4
gk4	constant symmetry	70	Gaussian	1,2,3,4
tec3	constant symmetry	10	Gaussian	1,2,3,4
KP1	MWO	NA	NA	1,2,3,4
StrnA	MWO	NA	NA	3,4
StrnE	constant symmetry	10	Gaussian	3,4
Strn1	MWO	NA	NA	4
Strn2	constant symmetry	10	Gaussian	4
Strn3	constant symmetry	5	Gaussian	4
Strn4	MWO	NA	NA	4
Strn6	constant symmetry	10	Gaussian	4
Strn7	constant symmetry	5	Gaussian	4
Strn8	constant symmetry	5	Gaussian	4

NA = not applicable; MWO = move with others

Table A.2: Variogram parameter settings used in the Structural Uncertainty Workflow of SKUA.

VARIABLE	VALUE	VARIABLE	VALUE
R1 (max)	1000 m	Azimuth	305 °
R2 (max)	1000 m	Dip	140 °
R3 (vertical)	200 m	Plunge	0 °

In addition to the three above mentioned input modes, a fourth setting "existing surface" is available to model the uncertainty of horizons. The existing surface input mode uses an alternative surface interpretation to constrain model realizations. We constructed alternative surface interpretations that reflect a maximum deviation in dip and azimuth of  $\pm 5^\circ$  from the original horizon surfaces. Horizons for perturbation were chosen based on the premises that a continuous representative horizon surface, build from input data during explicit modeling (Figure 4) was available across all fault blocks. For Model 4, an alternative surface interpretation was possible only for unit ku, because the domain was strongly fragmented after adding the seismic data; and no other unit could be represented continuously across all fault blocks. Furthermore, perturbations applied to an initial surface were spatially correlated using a variogram with the same parameter values for all four models (Table A.2).

Maximum displacement was determined based on the unit thickness information (Figure 3) and constraints from wells. The applied settings reflect an overall possible displacement of 30 m across all horizons, while avoiding unrealistic thickness perturbations of the relatively narrow ku unit by applying constraints on its upper and lower boundary surfaces (MWO or existing surface). All horizon parameter settings are summarized in Table A.3.

Table A.3: Horizon parameter settings used in the Structural Uncertainty Workflow of SKUA.

Unit	INPUT MODE	MAXIMUM DISPLACEMENT [M]	HONOR WELL	MODEL
DTM	fixed	NA	NA	1,2,3,4
j	MWO	NA	Yes	1,2,3,4
km3	constant symmetry	30	NA	1,2,3,4
km2	existing surface	surface	Yes	1
km2	MWO	NA	Yes	2,3,4
km1	existing surface	surface	Yes	1,2,3
km1	MWO	NA	Yes	4
ku	constant symmetry	30	Na	1
ku	existing surface	surface	Yes	2,3,4
mo	MWO	NA	NA	1,2
mo	MWO	NA	Yes	3,4
mm.mu	constant symmetry	30	NA	1,2,3,4
so	constant symmetry	30	NA	1,2,3,4
base	constant symmetry	30	NA	1,2,3,4

NA = not applicable; MWO = move with others

## A.2 APPENDIX OF PART III

Detailed model results of uplift rates at the ground surface and of the determined bulking coefficient are presented. Mean simulated uplift rates were calculated using a sliding mean function with a window of five. The value of the bulking coefficient  $\gamma$  was used to calculate deformation due to the precipitation of gypsum crystals. This coefficient is effectively constrained by the parameters  $b$  and  $\gamma_{\max}$ , which depend on the effective stress  $\sigma'$  prevailing in every cell of the model domain. The Python script `RadModel.py` is used to generate the MODFLOW and PHT3D input files, while the `PostProcessing.py` script calculates changes in heave and volume from the model outputs, subsequently used for calibration in PEST. The two observations data files (S5 and S6) contain the measured point and interpolated volume uplift information used to calibrate the model. The scripts and observation data files are available under the following URL: <https://agupubs.onlinelibrary.wiley.com/doi/10.1029/2018WR023579>

A.2.1 *Uplift rates*

Modeled and observed uplift rates at the ground surface are compared in detail and their variability is analyzed in space and time in Figure A.1. For locations close to the center of the heave cone ( $x < 12$  m), observation points were unavailable for calibration (Figure A.1). Overall, mean simulated uplift rates are in good agreement with measured rates, but are elevated for  $x < 60$  m. However, these uplift rates for locations close to the model center are only representative for a small fraction of the total radial model surface area and volume (6.3%). For values of  $x > 60$  m on the other hand, total uplift and uplift rates (Figure 10a and 9) drop as expected, but remain below the average measured values throughout the simulation time. Overall, except for early times (before 200 days), measured and average simulated mean uplift rates are in good agreement for the simulation period prior to the start of the mitigation measures ( $(9.6 \pm 3.5) \times 10^{-2}$  and  $(8.9 \pm 2.0) \times 10^{-2}$  mm d<sup>-1</sup>), but rapidly diverge afterwards ( $(8.2 \pm 2.3) \times 10^{-2}$  and  $(3.7 \pm 2.4) \times 10^{-2}$  mm d<sup>-1</sup>).

A.2.2 *Bulking coefficient*

For  $\gamma_{\max} = 2$  and  $b = 2.51$  (inversely estimated by the model calibration), the bulking coefficient  $\gamma$  ranges from 0.04 to 0.48. Due to the changing inflow conditions, the pore water pressures are reduced from phase one to two and thus also the maximum value of the coefficient drops from 0.48 to 0.37. Furthermore, maximum values can be found at the top and generally to the left hand specified flow bound-

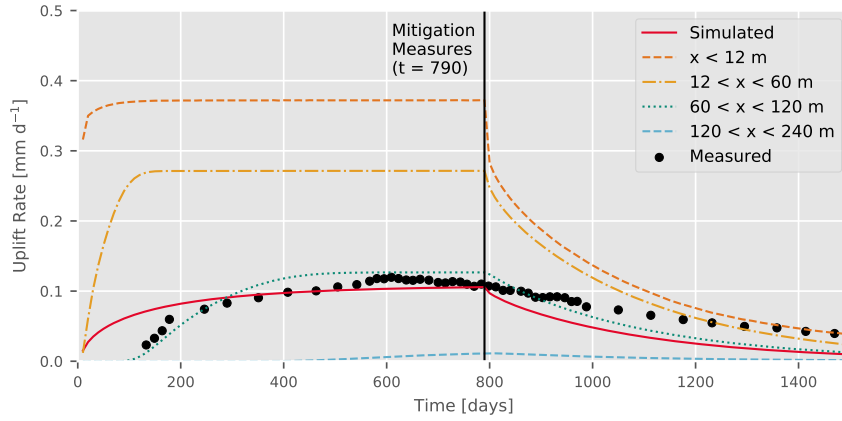


Figure A.1: Mean simulated (red line) and measured (black dots) uplift rates of the entire heave cone as well as mean simulated uplift rates in selected ranges of distances from the heave center.

ary of the model domain where the effective stress is low and pore pressures are high, respectively.

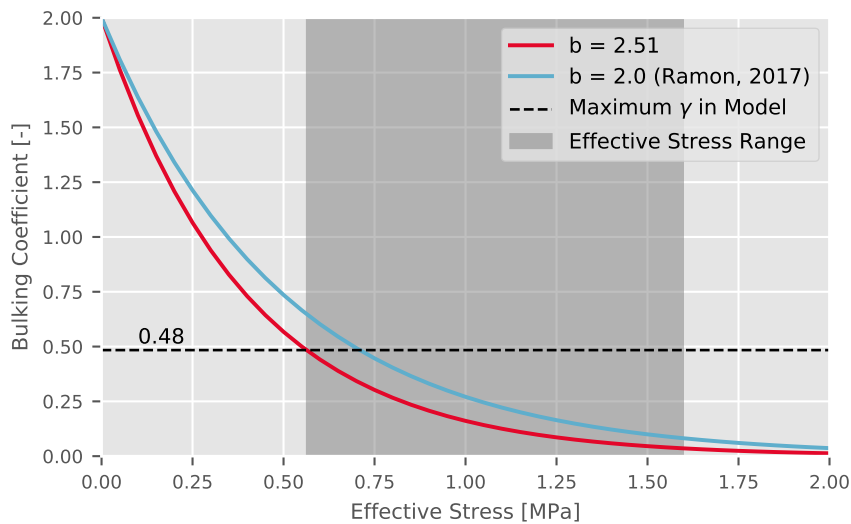


Figure A.2: The bulking coefficient  $\gamma$  as a function of the effective stress  $\sigma'$  and the fitting parameter  $b$ . The grey area indicates the range of  $\sigma'$ , and the dashed line the maximum bulking coefficient encountered in the model.



## BACK MATTER



## BIBLIOGRAPHY

---

- Alonso, E. E. (2012). Crystal growth and geotechnics. In *Riv. ital. di geotech.* (p. 13).
- Alonso, E. E., Berdugo, I., & Ramon, A. (2013). Extreme expansive phenomena in anhydritic-gypsiferous claystone: the case of Lilla tunnel. *Géotechnique*, 63(7), 584–612. doi:[10.1680/geot.12.P.143](https://doi.org/10.1680/geot.12.P.143)
- Alonso, E. E., & Olivella, S. (2008). Modelling Tunnel Performance in Expansive Gypsum Claystone. In *12th int. conf. int. assoc. comput. methods adv. geomech.* (pp. 891–910). Goa, India.
- Alonso, E. E., & Ramon, A. (2013). Heave of a railway bridge induced by gypsum crystal growth: field observations. *Géotechnique*, 63(9), 707–719. doi:[10.1680/geot.12.P.034](https://doi.org/10.1680/geot.12.P.034)
- Amstad, C., & Kovári, K. (2001). *Untertagbau in quellfähigem Fels - Travaux souterrains dans des roches gonflantes*. Institut für Geotechnik, Professur für Untertagbau, Eidgenössische Technische Hochschule Zürich. Zürich, Switzerland.
- Anagnostou, G. (1992). *Untersuchungen zur Statik des Tunnelbaus in quellfähigem Gebirge* (Doctoral dissertation, ETH Zürich).
- Anagnostou, G. (1993). A model for swelling rock in tunnelling. *Rock Mech. Rock Eng.* 26(4), 307–331. doi:[10.1007/BF01027115](https://doi.org/10.1007/BF01027115)
- Anagnostou, G. (1995). Seepage flow around tunnels in swelling rock. *Int. J. Numer. Anal. Methods Geomech.* 19(10), 705–724. doi:[10.1002/nag.1610191004](https://doi.org/10.1002/nag.1610191004)
- Anagnostou, G., Pimentel, E., & Serafeimidis, K. (2010). Swelling of sulphatic claystones - some fundamental questions and their practical relevance. *Geomech. Tunn.* 3(5), 567–572. doi:[10.1002/geot.201000033](https://doi.org/10.1002/geot.201000033)
- Anagnostou, G., Serafeimidis, K., & Vrakas, A. (2014). On the Occurrence of Anhydrite in the Sulphatic Claystones of the Gypsum Keuper. *Rock mechanics and rock Engineering*. doi:[10.1007/s00603-014-0568-y](https://doi.org/10.1007/s00603-014-0568-y)
- Anderssohn, J. (2015). *Satellitenbasierte Bodenbewegungsmessung in Böblingen, Deutschland*. Landratsamt Böblingen (LRABB). Böblingen, Germany.
- Appelo, C. A. J., & Postma, D. (2005). *Geochemistry, Groundwater and Pollution* (2nd). Amsterdam: A.A. Balkema Publishers.
- Aug, C., Chilès, J.-P., Courrioux, G., & Lajaunie, C. (2005). 3D Geological Modelling and Uncertainty: The Potential-field Method. In O. Leuangthong & C. V. Deutsch (Eds.), *Geostatistics banff 2004* (pp. 145–154). doi:[10.1007/978-1-4020-3610-1\\_15](https://doi.org/10.1007/978-1-4020-3610-1_15)
- Bakker, M., Post, V., Langevin, C. D., Hughes, J. D., White, J. T., Starn, J. J., & Fienen, M. N. (2016). Scripting MODFLOW Model Devel-

- opment Using Python and FloPy. *Groundwater*, 54(5), 733–739. doi:[10.1111/gwat.12413](https://doi.org/10.1111/gwat.12413)
- Bárdossy, G., & Fodor, J. (2001). Traditional and New Ways to Handle Uncertainty in Geology. *Nat. Resour. Res.* 10(3), 179–187. doi:[10.1023/A:1012513107364](https://doi.org/10.1023/A:1012513107364)
- Barton, A. F. M., & Wilde, N. M. (1971). Dissolution Rates of Polycrystalline Samples of Gypsum and Orthorhombic Forms of Calcium Sulphate by a Rotating Disc Method. *Trans. faraday Soc.* 67, 3590–3597. doi:[10.1039/TF9716703590](https://doi.org/10.1039/TF9716703590)
- Bayer, P., Saner, D., Bolay, S., Rybach, L., & Blum, P. (2012). Greenhouse gas emission savings of ground source heat pump systems in Europe: A review. *Renew. Sustain. Energy Rev.* 16(2), 1256–1267. doi:[10.1016/j.rser.2011.09.027](https://doi.org/10.1016/j.rser.2011.09.027)
- Behrmann, J. H., Hermann, O., Horstmann, M., Tanner, D. C., & Bertrand, G. (2003). Anatomy and kinematics of oblique continental rifting revealed: A three-dimensional case study of the southeast Upper Rhine graben (Germany). *Am. Assoc. Pet. Geol. Bull.* 87(7), 1105–1121. doi:[10.1306/02180300153](https://doi.org/10.1306/02180300153)
- Benz, T., & Wehnert, M. (2012). *Schadensfall Staufen im Breisgau - Zweiter Bericht zu den Berechnungen der zeitlichen Entwicklung der Hebungsprozesse.*
- Berdugo, I. R., Alonso, E. E., Romero, E., & Gens, A. (2009a). Tunneling and Swelling in Triassic Sulphate-Bearing Rocks. Part I -Case studies from Baden-Württemberg. *Rev. Epsil.* (12), 13–36.
- Berdugo, I. R., Alonso, E. E., Romero, E., & Gens, A. (2009b). Tunneling and Swelling in Triassic Sulphate-Bearing Rocks. Part II -Case studies from Jura Mountains. *Rev. Epsil.* (12), 39–53.
- Bistacchi, A., Massironi, M., Superchi, L., Zorzi, L., Francese, R., Giorgi, M., Chistolini, F., & Genevois, R. (2013). A 3D Geological Model of the 1963 Vajont Landslide. *Ital. J. Eng. Geol. Environ.* 2013(6), 531–539. doi:[10.4408/IJEGE.2013-06.B-51](https://doi.org/10.4408/IJEGE.2013-06.B-51)
- Blount, C., & Dickson, F. (1973). Gypsum-anhydrite equilibria in systems CaSO<sub>4</sub>-H<sub>2</sub>O and CaCO<sub>4</sub>-NaCl-H<sub>2</sub>O. *Am. Mineral.* 58(1941), 323–331.
- Boncio, P., Lavecchia, G., & Pace, B. (2004). Defining a model of 3D seismogenic sources for Seismic Hazard Assessment applications: The case of central Apennines (Italy). *J. Seismol.* 8(3), 407–425. doi:[10.1023/B:JOSE.0000038449.78801.05](https://doi.org/10.1023/B:JOSE.0000038449.78801.05)
- Bond, C. E. (2015). Uncertainty in structural interpretation: Lessons to be learnt. *J. Struct. Geol.* 74, 185–200. doi:[10.1016/j.jsrg.2015.03.003](https://doi.org/10.1016/j.jsrg.2015.03.003)
- Butscher, C., Breuer, S., & Blum, P. (2018). Swelling laws for clay-sulfate rocks revisited. *Bull. Eng. Geol. Environ.* 77(1), 399–408. doi:[10.1007/s10064-016-0986-z](https://doi.org/10.1007/s10064-016-0986-z)

- Butscher, C., Einstein, H. H., & Huggenberger, P. (2011). Effects of tunneling on groundwater flow and swelling of clay-sulfate rocks. *Water Resour. Res.* 47, 1–17. doi:[10.1029/2011WR011023](https://doi.org/10.1029/2011WR011023)
- Butscher, C., & Huggenberger, P. (2007). Implications for karst hydrology from 3D geological modeling using the aquifer base gradient approach. *J. Hydrol.* 342(1-2), 184–198. doi:[10.1016/j.jhydrol.2007.05.025](https://doi.org/10.1016/j.jhydrol.2007.05.025)
- Butscher, C., Huggenberger, P., Auckenthaler, A., & Bänninger, D. (2011). Risikoorientierte Bewilligung von Erdwärmesonden. *Grundwasser*, 16(16), 13–24. doi:[10.1007/s00767-010-0154-5](https://doi.org/10.1007/s00767-010-0154-5)
- Butscher, C., Huggenberger, P., & Zechner, E. (2011). Impact of tunneling on regional groundwater flow and implications for swelling of clay-sulfate rocks. *Eng. Geol.* 117(3-4), 198–206. doi:[10.1016/j.enggeo.2010.10.018](https://doi.org/10.1016/j.enggeo.2010.10.018)
- Butscher, C., Huggenberger, P., Zechner, E., & Einstein, H. H. (2011). Relation between hydrogeological setting and swelling potential of clay-sulfate rocks in tunneling. *Eng. Geol.* 122(3-4), 204–214. doi:[10.1016/j.enggeo.2011.05.009](https://doi.org/10.1016/j.enggeo.2011.05.009)
- Butscher, C., Mutschler, T., & Blum, P. (2016). Swelling of Clay-Sulfate Rocks: A Review of Processes and Controls. *Rock Mech. Rock Eng.* 49(4), 1533–1549. doi:[10.1007/s00603-015-0827-6](https://doi.org/10.1007/s00603-015-0827-6)
- Caers, J. (2011). Introduction. In *Model. uncertain. earth sci.* (Chap. Introducti, pp. 1–8). doi:[10.1002/9781119995920.ch1](https://doi.org/10.1002/9781119995920.ch1)
- Caine, J. S., Evans, J. P., & Forster, C. B. (1996). Fault zone architecture and permeability structure. *Geology*, 24(11), 1025–1028. doi:[10.1130/0091-7613\(1996\)024<1025](https://doi.org/10.1130/0091-7613(1996)024<1025)
- Campbell, S. D. G., Merritt, J. E., Dochartaigh, B. É. Ó., Mansour, M., Hughes, A. G., Fordyce, F. M., Entwisle, D. C., Monaghan, A. A., & Loughlin, S. C. (2010). 3D geological models and their hydrogeological applications: supporting urban development – a case study in Glasgow-Clyde, UK. *Zeitschrift der Dtsch. Gesellschaft für Geowissenschaften*, 161(2), 251–262. doi:[10.1127/1860-1804/2010/0161-0251](https://doi.org/10.1127/1860-1804/2010/0161-0251)
- Catoire, S., Guignard, P., & Jean-François, M. (2017). *Modalités de gestion et d'indemnisation des dégâts occasionnés par un forage géothermique sur la commune de Lochwiller (Bas-Rhin)*. Ministère de L'Environnement, De L'Énergie et de la Mer.
- Caumon, G., Collon-Drouaillet, P., Le Carlier de Veslud, C., Viseur, S., & Sausse, J. (2009). Surface-Based 3D Modeling of Geological Structures. *Math. Geosci.* 41(8), 927–945. doi:[10.1007/s11004-009-9244-2](https://doi.org/10.1007/s11004-009-9244-2)
- Caumon, G., Tertois, A.-L., & Zhang, L. (2007). Elements for Stochastic Structural Perturbation of Stratigraphic models. In *Proc. pet. geostatistics*. doi:[10.3997/2214-4609.201403041](https://doi.org/10.3997/2214-4609.201403041)

- Cherpeau, N., & Caumon, G. (2015). Stochastic structural modelling in sparse data situations. *Pet. Geosci.* 21(4), 233–247. doi:[10.1144/petgeo2013-030](https://doi.org/10.1144/petgeo2013-030)
- Cherpeau, N., Caumon, G., & Lévy, B. (2010). Stochastic simulations of fault networks in 3D structural modeling. *Comptes Rendus Geosci.* 342(9), 687–694. doi:[10.1016/j.crte.2010.04.008](https://doi.org/10.1016/j.crte.2010.04.008)
- Chilès, J. P., Aug, C., Guillen, a., & Lees, T. (2004). Modelling the Geometry of Geological Units and its Uncertainty in 3D From Structural Data : The Potential-Field Method. *Orebody Model. Strateg. Mine Plan. - Spectr.* 14, (November), 22–24.
- Christoffersen, J., & Christoffersen, M. R. (1976). The kinetics of dissolution of calcium sulphate dihydrate in water. *J. Cryst. Growth*, 35(1), 79–88. doi:[10.1016/0022-0248\(76\)90247-5](https://doi.org/10.1016/0022-0248(76)90247-5)
- Collon, P., Steckiewicz-Laurent, W., Pellerin, J., Laurent, G., Caumon, G., Reichart, G., & Vaute, L. (2015). 3D geomodelling combining implicit surfaces and Voronoi-based remeshing: A case study in the Lorraine Coal Basin (France). *Comput. Geosci.* 77, 29–43. doi:[10.1016/j.cageo.2015.01.009](https://doi.org/10.1016/j.cageo.2015.01.009)
- Culshaw, M. (2005). From concept towards reality: developing the attributed 3D geological model of the shallow subsurface. *Q. J. Eng. Geol. Hydrogeol.* 38(3), 231–284. doi:[10.1144/1470-9236/04-072](https://doi.org/10.1144/1470-9236/04-072)
- Dai, Z., Kan, A. T., Shi, W., Zhang, N., Zhang, F., Yan, F., Bhandari, N., Zhang, Z., Liu, Y., Ruan, G., & Tomson, M. B. (2017). Solubility Measurements and Predictions of Gypsum, Anhydrite, and Calcite Over Wide Ranges of Temperature, Pressure, and Ionic Strength with Mixed Electrolytes. *Rock Mech. Rock Eng.* 50(2), 327–339. doi:[10.1007/s00603-016-1123-9](https://doi.org/10.1007/s00603-016-1123-9)
- De La Varga, M., Schaaf, A., & Wellmann, F. (2019). GemPy 1.0: Open-source stochastic geological modeling and inversion. *Geosci. Model Dev.* 12(1), 1–32. doi:[10.5194/gmd-12-1-2019](https://doi.org/10.5194/gmd-12-1-2019)
- De Luca, A., & Termini, S. (1972). A definition of a nonprobabilistic entropy in the setting of fuzzy sets theory. *Inf. Control*, 20(4), 301–312. doi:[10.1016/S0019-9958\(72\)90199-4](https://doi.org/10.1016/S0019-9958(72)90199-4)
- Doherty, J. (2015). *Calibration and Uncertainty Analysis for Complex Environmental Models*. Brisbane, Australia: Watermark Numerical Computing.
- Doherty, J. (2016). Model-independent parameter estimation user manual Part II: PEST utility support software. Brisbane, Australia: Watermark Numerical Computing.
- Doherty, J., & Hunt, R. J. (2009). Two statistics for evaluating parameter identifiability and error reduction. *J. Hydrol.* 366(1-4), 119–127. doi:[10.1016/j.jhydrol.2008.12.018](https://doi.org/10.1016/j.jhydrol.2008.12.018)
- Domenico, P., & Mifflin, M. (1965). Water from Low-Permeability Sediments and Land Subsidence. *Water Resour. Res.* 1(4), 563–566.

- Domenico, P., & Schwartz, F. W. (1997). *Physical and Chemical Hydrogeology* (2nd). New York: John Wiley & Sons, Inc.
- Einstein, H. H. (1996). Tunnelling in difficult ground - Swelling behaviour and identification of swelling rocks. *Rock Mech. rock Eng.* 29(3), 113–124.
- Etzold, A., & Franz, M. (2005). Ein Referenzprofil des Keupers im Kraichgau – zusammengesetzt aus mehreren Kernbohrungen auf Blatt 6718 Wiesloch (Baden-Württemberg). Freiburg i. Br.: LGRB.
- Feehley, C. E., Zheng, C., & Molz, F. J. (2000). A dual-domain mass transfer approach for modeling solute transport in heterogeneous aquifers: Application to the Macrodispersion Experiment (MADE) site. *Water Resour. Res.* 36(9), 2501–2515. doi:[10.1029/2000WR900148](https://doi.org/10.1029/2000WR900148)
- Fjar, E., Holt, R., Raaen, A., Risnes, R., & Horsrud P. (1993). Petroleum related rock mechanics. *Int. J. Rock Mech. Min. Sci. Geomech. Abstr.* 30(5), 320. doi:[10.1016/0148-9062\(93\)92632-Z](https://doi.org/10.1016/0148-9062(93)92632-Z)
- Fleuchaus, P., & Blum, P. (2017). Damage event analysis of vertical ground source heat pump systems in Germany. *Geotherm. Energy*, 5(1), 10. doi:[10.1186/s40517-017-0067-y](https://doi.org/10.1186/s40517-017-0067-y)
- Frank, T., Tertois, A. L., & Mallet, J. L. (2007). 3D-reconstruction of complex geological interfaces from irregularly distributed and noisy point data. *Comput. Geosci.* 33(7), 932–943. doi:[10.1016/j.cageo.2006.11.014](https://doi.org/10.1016/j.cageo.2006.11.014)
- Freyer, D., & Voigt, W. (2003). Crystallization and Phase Stability of CaSO<sub>4</sub> and CaSO<sub>4</sub>-Based Salts. *Monatshefte für Chemie / Chem. Mon.* 134(5), 693–719. doi:[10.1007/s00706-003-0590-3](https://doi.org/10.1007/s00706-003-0590-3)
- Genser, H. (1958). *Geologie der Vorbergzone am südwestlichen Schwarzwaldrand zwischen Staufen und Badenweiler* (Doctoral dissertation).
- Genser, H. (1959). Stratigraphie und Tektonik der Vorbergzone am südwestlichen Schwarzwaldrand zwischen Staufen und Badenweiler. *Berichte der Naturforschenden Gesellschaft zu Freibg. im Breisgau*, 49, 59–112.
- Gonçalvès, J., Rousseau-Gueutin, P., de Marsily, G., Cosenza, P., & Violette, S. (2010). What is the significance of pore pressure in a saturated shale layer? *Water Resour. Res.* 46(4), 1–16. doi:[10.1029/2009WR008090](https://doi.org/10.1029/2009WR008090)
- Grimm, M., Stober, I., Kohl, T., & Blum, P. (2014). Schadensfallanalyse von Erdwärmesondenbohrungen in Baden-Württemberg. *Grundwasser*, 19(4), 275–286. doi:[10.1007/s00767-014-0269-1](https://doi.org/10.1007/s00767-014-0269-1)
- Grob, H. (1972). Schwellendruck im Belchentunnel (Swelling pressure in the Belchen tunnel). In *Int. symp. tunneling* (pp. 99–119). Luzern, Switzerland.
- Groschopf, R., Guntram, K., Leiber, J., Maus, H., Ohmert, W., Schreiner, A., & Wimmenauer, W. (Eds.). (1981). *Erläuterung zur Geologie-*

- chen Karte von Freiburg im Breisgau und Umgebung 1:25000* (2.). Stuttgart: Geologisches Landesamt Baden-Württemberg.
- Gysel, M. (1977). A contribution to the design of a tunnel lining in swelling rock. *Rock Mech.* 10, 55–71. doi:[10.1007/BF01261802](https://doi.org/10.1007/BF01261802)
- Hack, R., Orlic, B., Ozmutlu, S., Zhu, S., & Rengers, N. (2006). Three and more dimensional modelling in geo-engineering. *Bull. Eng. Geol. Environ.* 65(2), 143–153. doi:[10.1007/s10064-005-0021-2](https://doi.org/10.1007/s10064-005-0021-2)
- Harbaugh, A. (2005). *MODFLOW-2005: The U.S. Geological Survey modular ground-water model — the ground-water flow process*. doi:[10.3133/tm6A16](https://doi.org/10.3133/tm6A16)
- Harbaugh, A., Langevin, C., Hughes, J., Niswonger, R., & Konikow, L. (2017). MODFLOW-2005 version 1.12.00, the U.S. Geological Survey modular ground-water model. U.S. Geological Survey Software Release.
- Hardie, L. (1967). The gypsum-anhydrite equilibrium at one atmosphere pressure. *Am. Mineral.* 52(1903), 171–200.
- Hassen, I., Gibson, H., Hamzaoui-Azaza, F., Negro, F., Rachid, K., & Bouhlila, R. (2016). 3D geological modeling of the Kasserine Aquifer System, Central Tunisia: New insights into aquifer geometry and interconnections for a better assessment of groundwater resources. *J. Hydrol.* 539, 223–236. doi:[10.1016/j.jhydrol.2016.05.034](https://doi.org/10.1016/j.jhydrol.2016.05.034)
- Hauber, L., Jordan, P., & Madsen, F. (2005). *Tonminerale und Sulfate als Ursache für druckhaftes Verhalten von Gesteinen. Ursachen und Wirkungen des Quellvorganges* (tech. rep. No. 4306). Geologisch-palaeontologisches Institut der Universität Basel. Basel, Switzerland.
- He, S., Oddo, J. E., & Tomson, M. B. (1994). The Seeded Growth of Calcium Sulfate Dihydrate Crystals in NaCl Solutions up to 6 m and 90°C. *J. Colloid Interface Sci.* 163(2), 372–378. doi:[10.1006/jcis.1994.1116](https://doi.org/10.1006/jcis.1994.1116)
- Hecht-Méndez, J., Molina-Giraldo, N., Blum, P., & Bayer, P. (2010). Evaluating MT3DMS for heat transport simulation of closed geothermal systems. *Ground Water*, 48(5), 741–756. doi:[10.1111/j.1745-6584.2010.00678.x](https://doi.org/10.1111/j.1745-6584.2010.00678.x)
- Heimlich, C., Gourmelen, N., Masson, F., Schmittbuhl, J., Kim, S., & Azzola, J. (2015). Uplift around the geothermal power plant of Landau (Germany) as observed by InSAR monitoring. *Geotherm. Energy*, 3(2015), 1–12. doi:[10.1186/s40517-014-0024-y](https://doi.org/10.1186/s40517-014-0024-y)
- Henke, K. F., Kaiser, W., & Nagel, D. (1975). Geomechanische Untersuchungen im Gipskeuper - Forschungsberichte über Durchführung eines felsmechanischen Grossversuches in der Nordröhre des Wagenburgtunnels in Stuttgart. *Strassenbau und Strassenverkehrstechnik*, 184, 149–162.
- Hill, A. E. (1937). The Transition Temperature of Gypsum to Anhydrite. *J. Am. Chem. Soc.* 59(11), 2242–2244. doi:[10.1021/ja01290a039](https://doi.org/10.1021/ja01290a039)

- Holden, L., Mostad, P., Nielsen, B. F., Gjerde, J., Townsend, C., & Ottesen, S. (2003). Stochastic structural modeling. *Math. Geol.* 35(8), 899–914. doi:[10.1023/B:MATG.0000011584.51162.69](https://doi.org/10.1023/B:MATG.0000011584.51162.69)
- Hou, W., Yang, L., Deng, D., Ye, J., Clarke, K., Yang, Z., Zhuang, W., Liu, J., & Huang, J. (2016). Assessing quality of urban underground spaces by coupling 3D geological models: The case study of Foshan city, South China. *Comput. Geosci.* 89, 1–11. doi:[10.1016/j.cageo.2015.07.016](https://doi.org/10.1016/j.cageo.2015.07.016)
- Hsieh, P. A., & Freckleton, J. R. (1993). *Documentation of a computer program to simulate horizontal-flow barriers using the U.S. Geological Survey's modular three-dimensional finite-difference ground-water flow model*. U.S. Geological survey. doi:[10.3133/ofr92477](https://doi.org/10.3133/ofr92477)
- Huysmans, M., & Dassargues, A. (2005). Review of the use of Péclet numbers to determine the relative importance of advection and diffusion in low permeability environments. *Hydrogeol. J.* 13(5–6), 895–904. doi:[10.1007/s10040-004-0387-4](https://doi.org/10.1007/s10040-004-0387-4)
- Jeannin, P. Y., Eichenberger, U., Sinreich, M., Vouillamoz, J., Malard, a., & Weber, E. (2013). KARSYS: A pragmatic approach to karst hydrogeological system conceptualisation. Assessment of ground-water reserves and resources in Switzerland. *Environ. Earth Sci.* 69(3), 999–1013. doi:[10.1007/s12665-012-1983-6](https://doi.org/10.1007/s12665-012-1983-6)
- Jeschke, A. A., & Dreybrodt, W. (2002). Pitfalls in the determination of empirical dissolution rate equations of minerals from experimental data and a way out: An iterative procedure to find valid rate equations, applied to Ca-carbonates and -sulphates. *Chem. Geol.* 192(3–4), 183–194. doi:[10.1016/S0009-2541\(02\)00135-3](https://doi.org/10.1016/S0009-2541(02)00135-3)
- Jeschke, A. A., Vosbeck, K., & Dreybrodt, W. (2001). Surface controlled dissolution rates of gypsum in aqueous solutions exhibit nonlinear dissolution kinetics. *Geochim. Cosmochim. Acta*, 65(1), 27–34. doi:[10.1016/S0016-7037\(00\)00510-X](https://doi.org/10.1016/S0016-7037(00)00510-X)
- Jessell, M. W., Ailleres, L., & de Kemp, E. A. (2010). Towards an integrated inversion of geoscientific data: What price of geology? *Tectonophysics*, 490(3–4), 294–306. doi:[10.1016/j.tecto.2010.05.020](https://doi.org/10.1016/j.tecto.2010.05.020)
- Jessell, M. W., Pakyuz-charrier, E., Lindsay, M., Giraud, J., & de Kemp, E. (2018). Assessing and Mitigating Uncertainty in Three Dimensional Geologic Models in Contrasting Geologic Scenarios. (21), 63–74. doi:[10.5382/SP.21.04](https://doi.org/10.5382/SP.21.04)
- Julio, C., Caumon, G., & Ford, M. (2015). Sampling the uncertainty associated with segmented normal fault interpretation using a stochastic downscaling method. *Tectonophysics*, 639, 56–67. doi:[10.1016/j.tecto.2014.11.013](https://doi.org/10.1016/j.tecto.2014.11.013)
- Keck, C. (2017). *Die Geothermie Katastrophe in Staufeu - Eine Stadt in Bewegung*. Stuttgart.
- Kessler, H., Turner, a. K., Culshaw, M., & Royse, K. (2008). Unlocking the potential of digital 3D geological subsurface models for geotechnical engineers. In *Eur. econference int. assoc. eng. geol.*

- (pp. 15–20). Madrid: Asociacion Espanola de Geologia Aplicada a la Ingenieria.
- Kimmel, M., & Hadadou, R. (2016). *Evaluation du potentiel de gonflement résiduel des évaporites au droit du lotissement Weingarten à Lochwiller ( Bas-Rhin )*. Geoderis.
- Kinkeldey, C., Maceachren, A. M., Riveiro, M., & Schiewe, J. (2015). Evaluating the effect of visually represented geodata uncertainty on decision-making: systematic review, lessons learned, and recommendations. *Cartogr. Geogr. Inf. Sci.* doi:10.1080 / 15230406.2015.1089792
- Kirschke, D. (1995). Neue Versuchstechniken und Erkenntnisse zum Anhydritschwellen (New experimental techniques and insights in anhydrite swelling). In *Taschenb. für den tunnelbau 1996* (pp. 203–225). Essen, Germany: Verlag Gllückauf.
- Klir, G. J. (2005). *Uncertainty and Information: Foundations of Generalized Information Theory*. doi:10.1002/0471755575.ch3
- Konikow, L., Hornberger, G., Halford, K., & Hanson, R. (2009). Revised multi-node well (MNW2) package for MODFLOW ground-water flow model. U.S. Geological Survey Techniques and Methods.
- Kontrec, J., Kralj, D., & Brečević, L. (2002). Transformation of anhydrous calcium sulphate into calcium sulphate dihydrate in aqueous solutions. *J. Cryst. Growth*, 240(1-2), 203–211. doi:10.1016 / S0022-0248(02)00858-8
- Kovári, K., & Chiaverio, F. (2007). Modular yielding support for tunnels in heavily swelling rock. In *Stuva conf.* Cologne, Germany: Studiengesellschaft für Unterirdische Verkehrsanlagen e.V.
- Kresic, N. (2007). *Hydrogeology and Groundwater Modeling* (2nd ed.). Boca Raton, FL: CRC Press.
- Laird, D. A. (2006). Influence of layer charge on swelling of smectites. *Appl. Clay Sci.* 34(1-4), 74–87. doi:10.1016/j.clay.2006.01.009
- Langevin, C. D. (2008). Modeling Axisymmetric Flow and Transport. *Ground Water*, 46(4), 579–590. doi:10.1111 / j.1745-6584.2008.00445.x
- Lark, R. M., Mathers, S. J., Thorpe, S., Arkley, S. L. B., Morgan, D. J., & Lawrence, D. J. D. (2013). A statistical assessment of the uncertainty in a 3-D geological framework model. *Proc. Geol. Assoc.* 124(6), 946–958. doi:10.1016/j.pgeola.2013.01.005
- Lasaga, A. C. (1984). Chemical kinetics of water-rock interactions. *J. Geophys. Res.* 89(B6), 4009–4025. doi:10.1029/JBo89iBo6p04009
- Lasaga, A. C., Soler, J. M., Ganor, J., Burch, T. E., & Nagy, K. L. (1994). Chemical weathering rate laws and global geochemical cycles. *Geochim. Cosmochim. Acta*, 58(10), 2361–2386. doi:10.1016 / 0016-7037(94)90016-7

- Leung, Y., Goodchild, M. F., Lin, C. C., Leung, Y., Goodchild, M. F., & Lin, C. C. (1992). Visualization of fuzzy scenes and probability fields. *Comput. Sci. Stat.* 24, 416–422.
- LGRB. (1977). *Erläuterung zur hydrogeologischen Karte von Baden - Württemberg, Oberrheingebiet, Bereich Kaiserstuhl - Markgräflerland*. Landesamt für Geologie, Rohstoffe und Bergbau (LGRB). Freiburg.
- LGRB. (2010). *Geologische Untersuchungen von Baugrundhebungen im Bereich des Erdwärmesondenfeldes beim Rathaus in der historischen Altstadt von Staufen i. Br.* Landesamt für Geologie, Rohstoffe und Bergbau (LGRB).
- LGRB. (2012). *Zweiter Sachstandsbericht zu den seit dem 01.03.2010 erfolgten Untersuchungen im Bereich des Erdwärmesondenfeldes beim Rathaus in der historischen Altstadt von Staufen i. Br.* Landesamt für Geologie, Rohstoffe und Bergbau (LGRB).
- LGRB. (2013). *Geologische Untersuchungen von Baugrundhebungen im Bereich des Neubaugebiets „Im Kiesel“ in Rudersberg - Zumhof*. Landesamt für Geologie, Rohstoffe und Bergbau Baden - Württemberg.
- LGRB. (2015). *Geologische Untersuchungen von Baugrundhebungen im nordöstlichen Stadtgebiet von Böblingen (Hebungsgebiet "Nord")*. Landesamt für Geologie, Rohstoffe und Bergbau Baden-Württemberg. Freiburg.
- Lindsay, M., Aillères, L., Jessell, M. W., de Kemp, E. A., & Betts, P. G. (2012). Locating and quantifying geological uncertainty in three-dimensional models: Analysis of the Gippsland Basin, south-eastern Australia. *Tectonophysics*, 546–547, 10–27. doi:[10.1016/j.tecto.2012.04.007](https://doi.org/10.1016/j.tecto.2012.04.007)
- Lindsay, M., Jessell, M. W., Aillères, L., Perrouty, S., de Kemp, E., & Betts, P. G. (2013). Geodiversity: Exploration of 3D geological model space. *Tectonophysics*, 594, 27–37. doi:[10.1016/j.tecto.2013.03.013](https://doi.org/10.1016/j.tecto.2013.03.013)
- Lindsay, M., Perrouty, S., Jessell, M. W., & Aillères, L. (2014). Inversion and Geodiversity: Searching Model Space for the Answers. *Math. Geosci.* 46, 971–1010. doi:[10.1007/s11004-014-9538-x](https://doi.org/10.1007/s11004-014-9538-x)
- Lippmann, F. (1976). Corrensite, a swelling clay mineral, and its influence on floor heave in tunnels in the Keuper formation. *Bull. Eng. Geol. Environ.* 14(1), 65–68.
- Lisowski, M. (2006). Analytical volcano deformation source models. In D. Dzurisin (Ed.), *Volcano deform. - geod. monit. tech.* (Chap. 8, pp. 279–304). Heidelberg: Springer Praxis Books.
- Liu, G., Zheng, C., & Gorelick, S. M. (2007). Evaluation of the applicability of the dual-domain mass transfer model in porous media containing connected high-conductivity channels. *Water Resour. Res.* 43(12), 1–12. doi:[10.1029/2007WR005965](https://doi.org/10.1029/2007WR005965)
- Liu, J., Tang, H., Zhang, J., & Shi, T. (2014). Glass landslide: the 3D visualization makes study of landslide transparent and virtual-

- ized. *Environ. Earth Sci.* 72(10), 3847–3856. doi:[10.1007/s12665-014-3183-z](https://doi.org/10.1007/s12665-014-3183-z)
- LUBW. (2005). *Geotope im Regierungsbezirk Freiburg* (1.). Karlsruhe: Baden-Württemberg, Landesanstalt für Umweltschutz.
- LUBW. (2012). *Wasser- und Bodenatlas Baden-Württemberg (WaBoA)* (4th). Stuttgart: Landesanstalt für Umwelt, Messungen und Naturschutz Baden-Württemberg (LUBW).
- Lund, J. W., & Boyd, T. L. (2016). Direct utilization of geothermal energy 2015 worldwide review. *Geothermics*, 60, 66–93. doi:[10.1016/j.geothermics.2015.11.004](https://doi.org/10.1016/j.geothermics.2015.11.004)
- MacDonald, G. (1953). Anhydrite-gypsum equilibrium relations. *Am. J. Sci.* 884–898.
- Madsen, F., & Müller-Vonmoos, M. (1989). The swelling behaviour of clays. *Appl. Clay Sci.* 4(2), 143–156. doi:[10.1016/0169-1317\(89\)90005-7](https://doi.org/10.1016/0169-1317(89)90005-7)
- Madsen, F., & Nuesch, R. (1991). The swelling behaviour of clay-sulfate rocks. *7th ISRM Congr.* 285–288.
- Mallet, J. L. (1992). Discrete Smooth Interpolation in geometric modelling. *Comput. Des.* 24(4), 178–191.
- Mallet, J.-L. (2004). Space – Time Mathematical Framework for Sedimentary Geology. *Math. Geol.* 36(1), 1–32. doi:[10.1023/B:MATG.0000016228.75495.7c](https://doi.org/10.1023/B:MATG.0000016228.75495.7c)
- Mann, J. C. (1993). Uncertainty in Geology. In J. C. Davis & U. C. Herzfeld (Eds.), *Comput. geol. - 25 years prog.* (p. 298). New York: Oxford University Press, Inc.
- Marsal, D. (1952). Der Einfluß des Druckes auf das System CaSO<sub>4</sub>-H<sub>2</sub>O. *Heidelberger Beiträge zur Mineral. und Petrogr.* 3, 289–296.
- Mogi, K. (1958). Relations between the Eruptions of Various Volcanes and the Deformations of the Ground Surfaces around them. *Bull. Earthq. Res. Inst.* 36, 99–134. doi:[10.1016/j.epsl.2004.04.016](https://doi.org/10.1016/j.epsl.2004.04.016)
- Mullin, J. (2001). Crystal growth. In *Crystallization* (4th, pp. 216–288). doi:[10.1016/B978-075064833-2/50008-5](https://doi.org/10.1016/B978-075064833-2/50008-5)
- Nancollas, G. H., & Purdie, N. (1964). The kinetics of crystal growth. *Q. Rev. Chem. Soc.* 18(1), 1–20. doi:[10.1039/qr9641800001](https://doi.org/10.1039/qr9641800001)
- NDA. (2010). *Geological Disposal: An overview of the generic disposal system safety case* (tech. rep. No. December). Nuclear Decommissioning Authority.
- Nitsch, E., Beutler, G., Hauschke, N., Etzold, A., & Laaß, M. (2005). Detailed stratigraphic correlation of the Grabfeld Formation (Keuper Group, Triassic) from the Hochrhein region to the Baltic Sea. *Hallesches Jahrb. für Geowissenschaften*, 19, 135–150.
- Oldecop, L., & Alonso, E. E. (2012). Modelling the degradation and swelling of clayey rocks bearing calcium-sulphate. *Int. J. Rock Mech. Min. Sci.* 54, 90–102. doi:[10.1016/j.ijrmms.2012.05.027](https://doi.org/10.1016/j.ijrmms.2012.05.027)
- Olivella, S., & Alonso, E. E. (2008). Gas flow through clay barriers. *Géotechnique*, 58(3), 157–176. doi:[10.1680/geot.2008.58.3.157](https://doi.org/10.1680/geot.2008.58.3.157)

- Olivella, S., Gens, A., Carrera, J., & Alonso, E. E. (1996). Numerical formulation for a simulator (CODE\_BRIGHT) for the coupled analysis of saline media. *Eng. Comput. (Swansea, Wales)*, 13(7), 87–112. doi:[10.1108/02644409610151575](https://doi.org/10.1108/02644409610151575)
- Pakyuz-Charrier, E., Lindsay, M., Ogarko, V., Giraud, J., & Jessell, M. W. (2018). Monte Carlo simulation for uncertainty estimation on structural data in implicit 3-D geological modeling, a guide for disturbance distribution selection and parameterization. *Solid Earth*, 9(2), 385–402. doi:[10.5194/se-9-385-2018](https://doi.org/10.5194/se-9-385-2018)
- Panteleit, B., Jensen, S., Seiter, K., Budde, H., & McDiarmid, J. (2013). A regional geological and groundwater flow model of Bremen (Germany): an example management tool for resource administration. *Zeitschrift der Dtsch. Gesellschaft für Geowissenschaften*, 164(4), 569–580. doi:[doi:10.1127/1860-1804/2013/0035](https://doi.org/10.1127/1860-1804/2013/0035)
- Paradigm. (2015). *SKUA-GOCAD - Paradigm 15.5 User Guide*.
- Park, H., Scheidt, C., Fenwick, D., Boucher, A., & Caers, J. (2013). History matching and uncertainty quantification of facies models with multiple geological interpretations. *Comput. Geosci.* 17(4), 609–621. doi:[10.1007/s10596-013-9343-5](https://doi.org/10.1007/s10596-013-9343-5)
- Parkhurst, D. L., & Appelo, C. A. J. (1999). *User's guide to PHREEQC (Version 2) - A Computer Program for Speciation, Batch-Reaction, One-Dimensional Transport, and Inverse Geochemical Calculations*. Denver, Colorado: U.S. Geological Survey.
- Parkhurst, D. L., & Wissmeier, L. (2015). PhreeqcRM: A reaction module for transport simulators based on the geochemical model PHREEQC. *Adv. Water Resour.* 83, 176–189. doi:[10.1016/j.advwatres.2015.06.001](https://doi.org/10.1016/j.advwatres.2015.06.001)
- Partridge, E. P., & White, A. H. (1929). The Solubility of Calcium Sulfate from 0 to 200°C. *J. Am. Chem. Soc.* 51(2), 360–370. doi:[10.1021/ja01377a003](https://doi.org/10.1021/ja01377a003)
- Paul, S., & Maji, P. (2014). City block distance for identification of co-expressed microRNAs. *Mol. BioSyst.* 10, 1509–1523. doi:[10.1007/978-3-319-03756-1\\_35](https://doi.org/10.1007/978-3-319-03756-1_35)
- Pierau, B., & Kiehl, J. R. (1996). Widerstands - und Ausweichprinzip: Vergleich zweier Entwurfsmethoden für Tunnelbauten in quellfähigem Gebirge (Resistance and yield principle : comparison of two design approaches for tunnels in swelling rock). In *Taschenb. für den tunnelbau* (pp. 226–247). Essen, Germany: Verlag Glückauf.
- Pimentel, E. [E.]. (2007). A Laboratory Testing Technique And a Model For the Swelling Behavior of Anhydritic Rock. In *11th isrm congr. 9-13 july*, Lisbon, Portugal: International Society for Rock Mechanics.
- Prommer, H., Barry, D., & Zheng, C. (2003). MODFLOW/MT3DMS-Based Reactive Multicomponent Transport Modeling. *Ground Water*, 41(2), 247–257. doi:[10.1111/j.1745-6584.2003.tb02588.x](https://doi.org/10.1111/j.1745-6584.2003.tb02588.x)

- R Core Team. (2016). *R: A Language and Environment for Statistical Computing*. R Foundation for Statistical Computing. Vienna, Austria.
- Ramon, A. (2014). *Expansion mechanisms in sulphated rocks and soils PhD Thesis* (Doctoral dissertation, Universitat Politècnica de Catalunya).
- Ramon, A., & Alonso, E. E. (2013). Heave of a railway bridge: modelling gypsum crystal growth. *Géotechnique*, 63(9), 720–732. doi:[10.1680/geot.12.P.035](https://doi.org/10.1680/geot.12.P.035)
- Ramon, A., & Alonso, E. E. (2018). Heave of a Building Induced by Swelling of an Anhydritic Triassic Claystone. *Rock Mech. Rock Eng.* 51(9), 2881–2894. doi:[10.1007/s00603-018-1503-4](https://doi.org/10.1007/s00603-018-1503-4)
- Ramon, A., Alonso, E. E., & Olivella, S. (2017). Hydro - chemo - mechanical modelling of tunnels in sulfated rocks. *Géotechnique*, 67(11), 968–982. doi:[10.1680/jgeot.SiP17.P.252](https://doi.org/10.1680/jgeot.SiP17.P.252)
- Rauh, F., & Thuro, K. (2007). Investigations on the swelling behavior of pure anhydrites. *Rock Mech. Meet. Soc. Challenges Demands*. doi:[10.1201/NOE0415444019](https://doi.org/10.1201/NOE0415444019)
- Rimstidt, J., & Barnes, H. (1980). The kinetics of silica-water reactions. *Geochim. Cosmochim. Acta*, 44(11), 1683–1699. doi:[10.1016/0016-7037\(80\)90220-3](https://doi.org/10.1016/0016-7037(80)90220-3)
- Røe, P., Georgsen, F., & Abrahamsen, P. (2014). An Uncertainty Model for Fault Shape and Location. *Math. Geosci.* 1(123), 13. doi:[10.1007/s11004-014-9536-z](https://doi.org/10.1007/s11004-014-9536-z)
- Ruch, C., & Wirsing, G. (2013). Erkundung und Sanierungsstrategien im Erdwärmesonden - Schadensfall Staufen i. Br. *Geotechnik*, 36, 147–159. doi:[10.1002/gete.201300005](https://doi.org/10.1002/gete.201300005)
- Sanner, B., Karytsas, C., Mendrinós, D., & Rybach, L. (2003). Current status of ground source heat pumps and underground thermal energy storage in Europe. *Geothermics*, 32(4), 579–588. doi:[10.1016/S0375-6505\(03\)00060-9](https://doi.org/10.1016/S0375-6505(03)00060-9). arXiv: [arXiv:1011.1669v3](https://arxiv.org/abs/1011.1669v3)
- Sass, I., & Burbaum, U. (2010). Damage to the historic town of Staufen (Germany) caused by geothermal drillings through anhydrite-bearing formations. *Acta Carsologica*, 39, 233–245.
- Sawatzki, G., & Eichhorn, F. (Eds.). (1999). *Vorl. Geol. Karte Baden - Württemberg, 1:25000, Bl. 8112 Staufen im Breisgau* (2. prelimi). Freiburg i. Br.: Landesamt für Geologie, Rohstoffe und Bergbau Baden-Württemberg (LGRB).
- Schädlich, B., Marcher, T., & Schweiger, H. F. (2013). Application of a constitutive model for swelling rock to tunnelling. *Geotech. Eng.* 44(3), 47–54.
- Schamper, C., Jørgensen, F., Auken, E., & Effersø, F. (2014). Case History Assessment of near-surface mapping capabilities by airborne transient electromagnetic data — An extensive comparison to conventional borehole data. *Geophysics*, 79(4), B187–B199. doi:[Doi10.1190/Geo2013-0256.1](https://doi.org/10.1190/Geo2013-0256.1)
- Scheidler, S., Huggenberger, P., Butscher, C., & Dresmann, H. (2017). Tools to simulate changes in hydraulic flow systems in complex

- geologic settings affected by tunnel excavation. doi:[10.1007/s10064-017-1113-5](https://doi.org/10.1007/s10064-017-1113-5)
- Scheidt, C., & Caers, J. (2009a). Representing spatial uncertainty using distances and kernels. *Math. Geosci.* 41(4), 397–419. doi:[10.1007/s11004-008-9186-0](https://doi.org/10.1007/s11004-008-9186-0)
- Scheidt, C., & Caers, J. (2009b). Uncertainty Quantification in Reservoir Performance Using Distances and Kernel Methods Application to a West Africa Deepwater Turbidite Reservoir. *SPE J.* 14(04), 680–692. doi:[10.2118/118740-PA](https://doi.org/10.2118/118740-PA)
- Schöttle, M. (Ed.). (2005). *Geotope im Regierungsbezirk Freiburg*. Karlsruhe: Landesanstalt für Umweltschutz Baden-Württemberg.
- Schreiner, A. (1991). Geologie und Landschaft. In A. Hoppe (Ed.), *Markgräflerl. - entwicklung und nutzung einer landschaft* (81, 7–24, 6 Abb.). Freiburg i. Br.: Berichte der Naturforschenden Gesellschaft.
- Schweizer, D., Blum, P., & Butscher, C. (2017). Uncertainty assessment in 3-D geological models of increasing complexity. *Solid Earth*, 8(2), 515–530. doi:[10.5194/se-8-515-2017](https://doi.org/10.5194/se-8-515-2017)
- Schweizer, D., Prommer, H., Blum, P., & Butscher, C. (2019). Analyzing the heave of an entire city: modeling of swelling processes in clay-sulfate rocks. *Eng. Geol.* (Manuscript under review).
- Schweizer, D., Prommer, H., Blum, P., Siade, A. J., & Butscher, C. (2018). Reactive Transport Modeling of Swelling Processes in Clay-sulfate Rocks. *Water Resour. Res.* 54(9), 6543–6565. doi:[10.1029/2018WR023579](https://doi.org/10.1029/2018WR023579)
- Serafeimidis, K., & Anagnostou, G. (2012a). On the kinetics of the chemical reactions underlying the swelling of anhydritic rocks. In *Rock eng. technol. sustain. undergr. constr.* (Vol. EUROCK 201), Stockholm, Sweden.
- Serafeimidis, K., & Anagnostou, G. (2012b). Simultaneous anhydrite dissolution and gypsum precipitation in a closed swelling rock system. In *46th us rock mech. / geomech. symp.* (p. 11). Chicago, IL, USA: ARMA.
- Serafeimidis, K., & Anagnostou, G. (2013). On the time-development of sulphate hydration in anhydritic swelling rocks. *Rock Mech. rock Eng.* 619–634. doi:[10.1007/s00603-013-0376-9](https://doi.org/10.1007/s00603-013-0376-9)
- Serafeimidis, K., & Anagnostou, G. (2014a). On the crystallisation pressure of gypsum. *Environ. Earth Sci.* doi:[10.1007/s12665-014-3366-7](https://doi.org/10.1007/s12665-014-3366-7)
- Serafeimidis, K., & Anagnostou, G. (2014b). The solubilities and thermodynamic equilibrium of anhydrite and gypsum. *Rock Mech. Rock Eng.* doi:[10.1007/s00603-014-0557-1](https://doi.org/10.1007/s00603-014-0557-1)
- Shannon, C. E. (1948). A mathematical theory of communication. *Bell Syst. Tech. J.* 27(July), 379–423. doi:[10.1145/584091.584093](https://doi.org/10.1145/584091.584093)
- STD. (2016). *Stratigraphic Table of Germany 2016* (ed.) (M. Menning & A. Hendrich, Eds.). Potsdam, Germany: German Research Center for Geosciences.

- Steiner, W. (1993). Swelling rock in tunnels: Rock characterization, effect of horizontal stresses and construction procedures. *Int. J. Rock Mech. Min. Sci.* 30(4), 361–380. doi:[10.1016/0148-9062\(93\)91720-4](https://doi.org/10.1016/0148-9062(93)91720-4)
- Suzuki, S., Caumon, G., & Caers, J. (2008). Dynamic data integration for structural modeling: Model screening approach using a distance-based model parameterization. *Comput. Geosci.* 12(1), 105–119. doi:[10.1007/s10596-007-9063-9](https://doi.org/10.1007/s10596-007-9063-9)
- Tacher, L., Pomian-Srzednicki, I., & Parriaux, a. (2006). Geological uncertainties associated with 3-D subsurface models. *Comput. Geosci.* 32(2), 212–221. doi:[10.1016/j.cageo.2005.06.010](https://doi.org/10.1016/j.cageo.2005.06.010)
- Tertois, A.-L., & Mallet, J.-L. (2007). Editing Faults within tetrahedral volume models in real time. In S. J. Jolley, D. Barr, J. J. Walsh, & R. J. Knipe (Eds.), *Struct. complex reserv.* (Chap. 0, Vol. 292, pp. 89–101). Geol. Society Spec. Publ. doi:[10.1144/sp292.5](https://doi.org/10.1144/sp292.5)
- Thiele, S. T., Jessell, M. W., Lindsay, M., Ogarko, V., Wellmann, J. F., & Pakyuz-Charrier, E. (2016). The topology of geology 1: Topological analysis. *J. Struct. Geol.* 91, 27–38. doi:[10.1016/j.jsg.2016.08.009](https://doi.org/10.1016/j.jsg.2016.08.009)
- Thiele, S. T., Jessell, M. W., Lindsay, M., Wellmann, J. F., & Pakyuz-Charrier, E. (2016). The topology of geology 2: Topological uncertainty. *J. Struct. Geol.* 91, 74–87. doi:[10.1016/j.jsg.2016.08.010](https://doi.org/10.1016/j.jsg.2016.08.010)
- Tikhonov, A. N., & Arsenin, V. I. A. (1977). *Solutions of ill-posed problems*. Scripta series in mathematics. Winston.
- Ufrecht, W. (2017). Zur Hydrogeologie veränderlich fester Gesteine mit Sulfatgestein, Beispiel Gipskeuper (Trias, Grabfeld-Formation). *Grundwasser*, 22(3), 197–208. doi:[10.1007/s00767-017-0362-3](https://doi.org/10.1007/s00767-017-0362-3)
- Wallis, I., Prommer, H., Post, V., Vandenbohede, A., & Simmons, C. T. (2013). Simulating MODFLOW-based reactive transport under radially symmetric flow conditions. *Ground Water*, 51(3), 398–413. doi:[10.1111/j.1745-6584.2012.00978.x](https://doi.org/10.1111/j.1745-6584.2012.00978.x)
- Webb, A. R., & Copsey, K. D. (2003). Measures of dissimilarity. In *Stat. pattern recognit.* (Second, Chap. A1, pp. 419–429). Chichester, UK: John Wiley & Sons, Ltd.
- Wellmann, J. F. (2013). Information theory for correlation analysis and estimation of uncertainty reduction in maps and models. *Entropy*, 15(4), 1464–1485. doi:[10.3390/e15041464](https://doi.org/10.3390/e15041464)
- Wellmann, J. F., Horowitz, F. G., Schill, E., & Regenauer-Lieb, K. (2010). Towards incorporating uncertainty of structural data in 3D geological inversion. *Tectonophysics*, 490(3-4), 141–151. doi:[10.1016/j.tecto.2010.04.022](https://doi.org/10.1016/j.tecto.2010.04.022)
- Wellmann, J. F., & Regenauer-Lieb, K. (2012). Uncertainties have a meaning: Information entropy as a quality measure for 3-D geological models. *Tectonophysics*, 526-529, 207–216. doi:[10.1016/j.tecto.2011.05.001](https://doi.org/10.1016/j.tecto.2011.05.001)

- Welter, D. E., White, J. T., Hunt, R. J., & Doherty, J. (2015). *Approaches in Highly Parameterized Inversion: PEST++ Version 3, A Parameter ESTimation and Uncertainty Analysis Software Suite Optimized for Large Environmental Models*. U.S. Geological Survey. doi:[10.3133/tm7C12](https://doi.org/10.3133/tm7C12)
- White, J. T., Fienen, M. N., & Doherty, J. (2016). A python framework for environmental model uncertainty analysis. *Environ. Model. Softw.* 85, 217–228. doi:[10.1016/j.envsoft.2016.08.017](https://doi.org/10.1016/j.envsoft.2016.08.017)
- Witkamp, G., Van der Eerden, J., & Van Rosmalen, G. (1990). Growth of gypsum. *J. Cryst. Growth*, 102(1-2), 281–289. doi:[10.1016/0022-0248\(90\)90912-5](https://doi.org/10.1016/0022-0248(90)90912-5)
- Wittke, W. (2014). Swelling Rock. In *Rock mech. based an anisotropic jointed rock model* (pp. 181–208). doi:[10.1002/9783433604281.ch8](https://doi.org/10.1002/9783433604281.ch8)
- Yager, R. R. (1995). Measures of entropy and fuzziness related to aggregation operators. *Inf. Sci. (Ny)*. 82(3-4), 147–166. doi:[10.1016/0020-0255\(94\)00030-F](https://doi.org/10.1016/0020-0255(94)00030-F)
- Yamamoto, J. K., Koike, K., Kikuda, A. T., Campanha, G. A. D. C., & Endlen, A. (2014). Post-processing for uncertainty reduction in computed 3D geological models. *Tectonophysics*, 633, 232–245. doi:[10.1016/j.tecto.2014.07.013](https://doi.org/10.1016/j.tecto.2014.07.013)
- Zadeh, L. (1965). Fuzzy sets. *Inf. Control*, 8(3), 338–353. doi:[10.1016/S0019-9958\(65\)90241-X](https://doi.org/10.1016/S0019-9958(65)90241-X)
- Zheng, C. (2010). *MT3DMS v5.3: Supplemental User's Guide*.
- Zorn, T., K uchler, R., Noack, K., Dittmar, T., & Worch, E. (2009). Zur Gipsaufl osung in Batch- und S ulenversuchen. *Grundwasser*, 14(4), 287–295. doi:[10.1007/s00767-009-0118-9](https://doi.org/10.1007/s00767-009-0118-9)



## OWN PUBLICATIONS

---

### PEER-REVIEWED INTERNATIONAL PUBLICATIONS

- Schweizer, D., Blum, P., & Butscher, C. (2017). Uncertainty assessment in 3-D geological models of increasing complexity. *Solid Earth*, 8(2), 515–530. doi:[10.5194/se-8-515-2017](https://doi.org/10.5194/se-8-515-2017)
- Schweizer, D., Prommer, H., Blum, P., & Butscher, C. (2019). Analyzing the heave of an entire city: modeling of swelling processes in clay-sulfate rocks. *Eng. Geol.* ((under review)).
- Schweizer, D., Prommer, H., Blum, P., Siade, A. J., & Butscher, C. (2018). Reactive Transport Modeling of Swelling Processes in Clay-sulfate Rocks. *Water Resour. Res.* 54(9), 6543–6565. doi:[10.1029/2018WR023579](https://doi.org/10.1029/2018WR023579)

### CONFERENCE CONTRIBUTIONS

- Schweizer, D., Blum, P., & Butscher, C. (2015). Integrated hydrogeological and geochemical processes in swelling of clay-sulfate rocks (poster). In *Geophys. res. abstr.* (Vol. 17, EGU 2015–1599, April 12–17). Vienna, Austria: EGU General Assembly.
- Schweizer, D., Blum, P., & Butscher, C. (2016). 3D geologische Modelle als Grundlage für Stofftransportmodellierung (oral presentation). In *25. tagung der fh-dggv "grundwasser – mensch- ökosysteme"* (Session O 15.7, Forum Junge Hydrogeologen, April 13–17). Karlsruhe, Germany.
- Schweizer, D., Prommer, H., Blum, P., & Butscher, C. (2019). Schadensfall Staufen: Simulation hydraulischer und geochemischer Prozesse (oral presentation). In *21. tagung ingenieurgeologie* (October 29 – 30). Würzburg, Germany: Deutsche Gesellschaft für Geotechnik e.V. (DGGT).
- Schweizer, D., Prommer, H., Blum, P., Siade, A. J., & Butscher, C. (2016). A preliminary reactive transport approach to quantify swelling of clay-sulfate rocks (poster). In *49th fall meet.* ((H13F–1455), December 12–16). San Francisco, California (United States): American Geophysical Union (AGU).
- Schweizer, D., Prommer, H., Blum, P., Siade, A. J., & Butscher, C. (2017a). Reactive transport modeling to quantify anhydrite dissolution and gypsum precipitation in clay-sulfate rocks (oral presentation). In *Geobremen 2017* (September 24–29). Bremen, Germany: Deutsche Mineralogische Gesellschaft (DMG) und Deutsche Geologische Gesellschaft – Geologische Vereinigung (DGGV).

- Schweizer, D., Prommer, H., Blum, P., Siade, A. J., & Butscher, C. (2017b). Reactive transport modeling to quantify swelling of clay-sulfate rocks (poster). In *Geophys. res. abstr.* (Vol. 19, EGU 2017-13438, April 23 –28). Vienna, Austria: EGU General Assembly.
- Schweizer, D., Prommer, H., Blum, P., Siade, A. J., & Butscher, C. (2017c). Reaktive Transportmodellierung zur Quantifizierung der Quellprozesse in Ton-Sulfatgesteinen (oral presentation). In *20. tagung ingenieurgeologie* (September 6 –8). Würzburg, Germany: Deutsche Gesellschaft für Geotechnik e.V. (DGGT).

## ACKNOWLEDGEMENTS

---

This thesis would not have been possible without the inspiration and support of a number of wonderful individuals — my thanks and appreciation to all of them for being part of this journey and making this thesis possible.

First and foremost I would like to express my deep gratitude to my supervisors Prof. Dr. Christoph Butscher and Prof. Dr. Philipp Blum for accepting me into their PhD program, for their guidance, continues encouragement and for always supporting me. You never lost trust in my abilities even during challenging times and encouraged me to develop my own ideas. Christoph, you were an excellent mentor, always making time for inspiring discussions, to share your expertise, and to answer my countless questions. With your calm and focused nature you have guided me through the many actual and imaginary crises and pitfalls during my PhD. But most importantly I would like to thank you for giving me, as a newcomer to engineering geology and hydrogeology, the opportunity to broaden my horizon, acquire new skills and to pursue this exciting path. Philipp, thank you for helping me focus on the “bigger picture”, for your critical perspective “from the outside”, for the brain storming and developing of ideas and concepts and for all the fruitful discussions.

Special thanks go to Dr. Henning Prommer for welcoming me to his research group at the CSIRO in Australia. His expertise in reactive transport modeling was a significant influence in shaping many of the concepts in this thesis. Thank you, for your constant help and support. I would like to thank Dr. Adam Siade for his invaluable insights into parameter estimation with PEST, his patience in answering all my questions, and for his contagious enthusiasm on the topic. I also want to thank Nat Raisbeck-Brown for welcoming me to her home and supporting me in so many ways during my time at the CSIRO and in Perth.

I would like to extend my thanks to my colleagues at the Department of Engineering Geology and Hydrogeology, especially Dr. Susanne Benz and Dr. Tobias Kling, for a great working atmosphere, solid support in many ways, and also the carefree conversations.

In addition, many other people have been involved in many different respects. This thesis would not have been possible without the help of Ralf Loritz, Lukas Luft, Alf Martin and Brian Shaw who considerably improved my thesis by their proofreading and valuable comments, Dipl.-Ing. Thomas Mutschler and his insights into rock mechanics, Dr. Horst Dresmann, Dr. Björn Zehner and Dr. Peter Achziger who supported me in the 3D geological modeling and I had

many fruitful discussion with, Prof. Dr. Guillaume Caumon, Prof. Dr. Florian Wellmann and the anonymous reviewers in the peer-review process who helped improve my manuscripts with their comments and expertise, and the Paradigm support team that tirelessly answered countless questions.

I gratefully acknowledge funding by the German Research Foundation (DFG) and from the Graduate School for Climate and Environment (GRACE). I further acknowledge the support for open access publishing by the Deutsche Forschungsgemeinschaft (DFG) and the Open Access Publishing Fund of Karlsruhe Institute of Technology (KIT). I would also like to thank the Geological Survey of Baden - Württemberg (LGRB) and the Landratsamt Breisgau - Hochschwarzwald (LKBH) for the provision of data.

Finally, my deep and sincere gratitude to my family and my partner Sonja for their continuous and unparalleled love, help and support. To my parents, thank you for always encouraging and supporting me in all my pursuits and adventures that opened my mind to the world and made me the person I am today. You are the best!!! Sonja, thank you for always being there for me and that you never lose confidence in me, even when I am in doubt myself. I am incredibly thankful and happy to have you by my side. This journey would not have been possible if not for you.

## DECLARATION

---

### AUTHORSHIP

**Chapter 2:** *Schweizer, D., Blum, P., & Butscher, C. (2017). Uncertainty assessment in 3-D geological models of increasing complexity. Solid Earth, 8(2), 515–530. doi:10.5194/se-8-515-2017*

Daniel Schweizer (DS) carried out the geological modeling using GO-CAD/SKUA in consultation with Christoph Butscher (CB) and Philipp Blum (PB). DS developed and implemented the general approach for the uncertainty assessment based on the concept of information entropy by Florian Wellmann (FW). DS analyzed the resulting data by developing R codes and evaluated the results in consultation with CB and PB. DS wrote the manuscript, whereby CB significantly improved the manuscript. The final manuscript was reviewed by all authors. DS accompanied it through the review process.

**Chapter 3:** *Schweizer, D., Prommer, H., Blum, P., Siade, A. J., & Butscher, C. (2018). Reactive Transport Modeling of Swelling Processes in Clay-sulfate Rocks. Water Resour. Res. 54(9), 6543–6565. doi:10.1029/2018WR023579*

Daniel Schweizer developed the conceptual model and methods with significant contribution by Henning Prommer (HP) and in consultation with CB, PB and Adam Siade (AS). DS implemented the numerical model and the R/Python scripts to pre- and post-process the data. DS conducted the parameter estimation, and obtained and analyzed the model results in consultation with all authors. AS significantly contributed to the parameter estimation and uncertainty analysis. DS wrote the manuscript and accompanied it through the review process, with HP and CB significantly improving the manuscript methods and results part. The final manuscript was reviewed by all authors.

**Chapter 4:** *Schweizer, D., Prommer, H., Blum, P., & Butscher, C. (2019). Analyzing the heave of an entire city: modeling of swelling processes in clay-sulfate rocks. Eng. Geol. (Manuscript under review)*

Daniel Schweizer implemented the numerical model and the Python scripts to pre- and post-process the data in consultation with CB. DS conducted the parameter estimation, and obtained and analyzed the model results in consultation with CB and PB. DS wrote the manuscript and is accompanying the review process. The final manuscript was reviewed by all authors.

Eidesstattliche Versicherung gemäß §6 Abs. 1 Ziff. 4 der Promotionsordnung des Karlsruher Instituts für Technologie für die Fakultät für Bauingenieur-, Geo- und Umweltwissenschaften:

1. Bei der eingereichten Dissertation zu dem Thema *Integrated hydrogeological and geochemical processes in swelling clay-sulfate rocks* handelt es sich um meine eigenständig erbrachte Leistung.
2. Ich habe nur die angegebenen Quellen und Hilfsmittel benutzt und mich keiner unzulässigen Hilfe Dritter bedient. Insbesondere habe ich wörtlich oder sinngemäß aus anderen Werken übernommene Inhalte als solche kenntlich gemacht.
3. Die Arbeit oder Teile davon habe ich bislang nicht an einer Hochschule des In- oder Auslands als Bestandteil einer Prüfungs- oder Qualifikationsleistung vorgelegt.
4. Die Richtigkeit der vorstehenden Erklärungen bestätige ich.
5. Die Bedeutung der eidesstattlichen Versicherung und die strafrechtlichen Folgen einer unrichtigen oder unvollständigen eidesstattlichen Versicherung sind mir bekannt.

Ich versichere an Eides statt, dass ich nach bestem Wissen die reine Wahrheit erklärt und nichts verschwiegen habe.

*Karlsruhe, Oktober 2019*

---

M.Sc. Daniel Michael  
Schweizer

#### COLOPHON

This document was typeset using the typographical look-and-feel `classicthesis` developed by André Miede. The style was inspired by Robert Bringhurst's seminal book on typography "*The Elements of Typographic Style*". `classicthesis` is available for both  $\text{\LaTeX}$  and  $\text{\LyX}$ :

<https://bitbucket.org/amiede/classicthesis/>

Happy users of `classicthesis` usually send a real postcard to the author, a collection of postcards received so far is featured here:

<http://postcards.miede.de/>

*Final Version* as of October 29, 2019 (`classicthesis` version 1.0).